# A Photoluminescence Study of a Beryllium Related Defect in Silicon

A thesis for the degree of

## DOCTOR OF PHILOSOPHY

Presented to

## DUBLIN CITY UNIVERSITY

By

## SIOBHAN ELIZABETH DALY B.Sc.

Research Supervisor

### DR. MARTIN O. HENRY

School of Physical Sciences

Dublin City University

September 1994

## Declaration

I hereby certify that this material, which I now submit for assessment on the programme of study leading to the award of Doctor of Philosophy is entirely my own work and has not been taken from the work of others save and to the extent that such work has been cited and acknowledged within the text of my work.

Signed: _Siobhán Daly_      Date: _3/10/94_

    Siobhan E. Daly.

# Table of Contents

# Abstract

Photoluminescence (PL) spectroscopy is used to investigate the optical properties of a beryllium related defect in silicon. Bound exciton recombination at the defect centre produces a distinctive PL spectrum consisting of a strong zero phonon transition at 1137 98(5) meV together with a well defined local mode structure containing a series of sharp, high energy local mode phonon replicas. The chemical nature of the defect is considered and is believed to incorporate both beryllium and oxygen, the latter of which is present in significant quantities in as grown Czochralski (CZ) silicon. An examination of the vibronic sideband of the zero phonon line supports this suggestion.

Uniaxial stress spectroscopy shows the defect to have a low symmetry configuration, found to be consistent with a rhombic I ($C_{2v}$) symmetry group. The application of a magnetic field reveals no Zeeman splitting, indicating that the bound exciton must consist of two spin 1/2 particles, this behaviour is consistent with a pseudo-donor model where the angular momentum of the bound hole is strongly quenched in the low symmetry axial field of the defect.

Conventional isotope substitution experiments with beryllium are impossible, as there is only one isotope of stable Be available. The use of radioactive isotopes is considered as a means of overcoming this problem. A feasibility study involving silicon implanted with radioactive indium is presented. This is the first occasion in which the PL spectra of defects involving radioactive isotopes have observed.

# Chapter 1
## Introduction

## 1.1 Introduction

The properties of a semiconducting material are markedly influenced by the presence of impurities and by any imperfections or disruptions to its crystalline structure The ability to incorporate selected impurities, and to eliminate or modify the effects of undesirable impurities, is central to achieving desired optical and electrical characteristics Very Large Scale Integrated (VLSI) circuits, for example, incorporate devices with sub micron dimensions It is particularly in these regimes that even very small impurity concentrations can become catastrophic to the performance of a device

Impurities give rise to defect structures within the crystal structure A defect may be described as any imperfection introduced into the crystal structure which disrupts the periodic three dimensional array of atoms within the lattice thus altering the properties of the material Defects may be extended in nature such as dislocations, stacking faults, grain boundaries and precipitates These defects have a significant effect on the macroscopic properties of the material such as tensile strength and elasticity A further classification of defects is referred to generally as point defects These can consist of single impurity atoms, which can exist in interstitial or substitutional lattice positions The host lattice element, for example silicon, can itself give rise to point defects in the form of self interstitials and vacancies Defect associates containing one or more impurities or defects in close proximity are also regarded as point defects A further classification of point defects can be made if we consider the constituents of the defect. An intrinsic defect is one arising from vacancies and self-interstitials present in the material Native impurities in the form of oxygen and carbon are present in significant quantities, these together with impurity atoms give rise to a large number of extrinsic point defects Complex point defects such as these have attracted much attention over the past three decades and is the class of defect with which this work is primarily concerned

The role a given impurity or defect can play in a semiconductor depends strongly

on the localised energy levels it introduces into the otherwise forbidden energy gap of the semiconductor The most fundamental properties of the defect can be established by uncovering the nature and positions of the energy levels introduced by the defect From this information defects can be evaluated in terms of their optical, chemical and electrical nature in order that we gain an understanding of the fundamental physical properties associated with them and thus how they may be utilised, modified or eliminated in order to enhance the properties of the material

Photoluminescence (PL) spectroscopy has proved to be a very sensitive tool for investigating both intrinsic electronic transitions and electronic transitions at impurities and defects in semiconductors Because of its sensitivity relative to other characterisation techniques, PL lends itself well to the characterisation of defects in silicon for which, silicon being an indirect gap semiconductor, the luminescence efficiency is small compared to other direct gap semiconductors Over 100 defect complexes have been identified in silicon [1] which give rise to PL spectra Due to the sensitivity of the technique and the well established spectroscopic methods, high resolution work is possible PL can be used to probe the symmetry of a defect using uniaxial stress and Zeeman spectroscopy and to identify the chemical constituents of a defect using isotope substitution A limitation associated with PL is the difficulty in obtaining absolute intensity measurements The luminescence intensity associated with a defect system will depend on the excitation density, the temperature, the sample geometry and capture cross-sections Despite this limitation, photoluminescence is one of the most revealing and versatile characterisation techniques available for the study of defects in silicon and constitutes the primary technique used in this work A review of photoluminescence and other related optical characterisation techniques is given by Perkowitz [2]

Central to this work is the characterisation of a defect structure in beryllium implanted, oxygen rich silicon In order to gain an understanding of the reaction kinetics likely to influence the formation of this defect, many factors must be taken into account In silicon the formation of defects can be attributed to a number of factors, most notably, the nature of the silicon crystal, the residual impurities in the crystal, in particular carbon and oxygen, the manner in which the impurities are incorporated and the processes to which the Si crystal is subjected The present state of knowledge in these areas will now be addressed in order to provide a basis on which to interpret the

## 1.2 Basic Properties of Silicon.

In chapter two the band structure of silicon will be considered with particular reference to the optical spectra which result from defect structures imbedded in the silicon crystal In this chapter some basic properties of the silicon crystal and its ability to incorporate impurities will be addressed Silicon is a group IV element which crystallises in the diamond structure, a schematic representation of which is contained
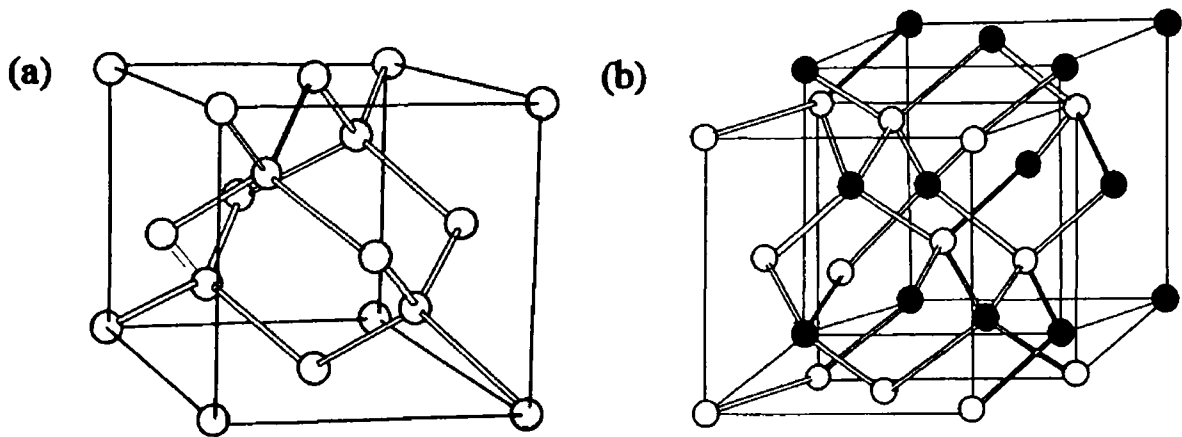


*Figure 1 1  (a) Diamond crystal structure consisting of (b) two interpenetrating face centered cubic lattices*

in figure 1 1(a), and can be considered to be composed of two interpenetrating face-centered cubic lattices as illustrated in figure 1 1(b)  Each atom is covalently bonded to four nearest neighbours arranged in the shape of a regular tetrahedron  The interatomic spacing, at room temperature, is 0 234 nm, corresponding to a lattice parameter of 0 543 nm and a density of 2330 kg/m$^3$ which is equivalent to 5 x 10$^{22}$ atoms/cm$^3$

Impurities are readily incorporated into silicon, the impurity is accommodated as either a substitutional atom, or as an interstitial atom  The two most commonly occupied interstitial sites are the tetrahedral interstitial site and the hexagonal interstitial site, as illustrated in figure 1 2 (a) and (b)  In order for defect complexes to form the
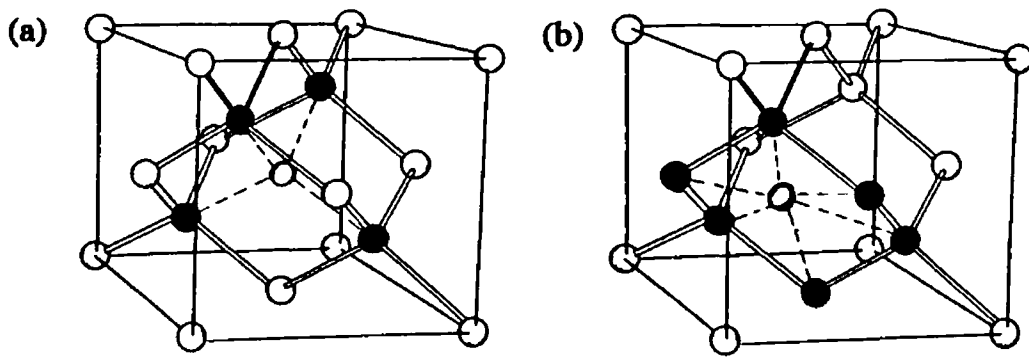
*Figure 1 2   Interstitial locations in the Si lattice   (a) Tetrahedral interstitial site and (b) hexagonal interstitial site*

various impurities must move through the crystal to complex with other impurities or with silicon interstitial atoms or with vacancies  The ability of an impurity to move is determined by its diffusion coefficient (or diffusivity) D, which may generally be expressed as a function of temperature by

$$D = D_0 \exp\left(-\frac{E_a}{kT}\right)$$  1.1

where the constant $D_0$ is related to the jump frequency and $E_a$ is the activation energy [14]   Both the prefactor $D_0$ and the exponential term are temperature dependent However, $D_0$ is usually considered to be constant within a temperature range of one hundred degrees, because the temperature dependence of D is mainly controlled by the exponential factor   The diffusivity is the rate at which a particular atom travels through the crystal and has units $cm^2s^{-1}$, atoms which diffuse interstitially have typical values of $1x10^{-4}$ - $1x10^{-9}$ $cm^2s^{-1}$ while atoms that diffuse substitutionally can have values down to $1x10^{-16}$ $cm^2s^{-1}$ [14]   In general the activation energies associated with the diffusion of interstitial atoms in silicon is of the order of 0 3 - 2 0 eV, whereas the activation energies associated with substitutional diffusion is of the order of 2 5 - 4 0 eV [14]

## 1.3 Native Impurities in Silicon - Oxygen and Carbon

Oxygen and carbon are considered to be key impurities in silicon and together constitute the highest impurity concentration found in silicon In as-grown material these impurities are incorporated mainly as interstitial oxygen ($O_i$) atoms and substitutional carbon ($C_s$) atoms, both of which are electrically neutral [3] Their main influence on the optical and electrical properties occurs as a result of the nucleation of complexes and precipitates, thus creating a wealth of defects The interaction between them in silicon crystals has been the subject of much research for its technological importance, because precipitated oxygen acts as a gettering centre [4] for metallic impurities and because carbon enhances the oxygen precipitation [5]

The presence of oxygen in silicon in concentrations orders of magnitude higher than the usual doping impurities was first established by Kaiser, Keck and Lange [6] who related the oxygen content to the intensity of an absorption band at 9 µm By observing the isotope shift of this band on substituting $O^{18}$ and $O^{16}$ the oxygen origin of the 9 µm band was confirmed [7]

The presence of oxygen in silicon can be directly attributed to the crystal growth
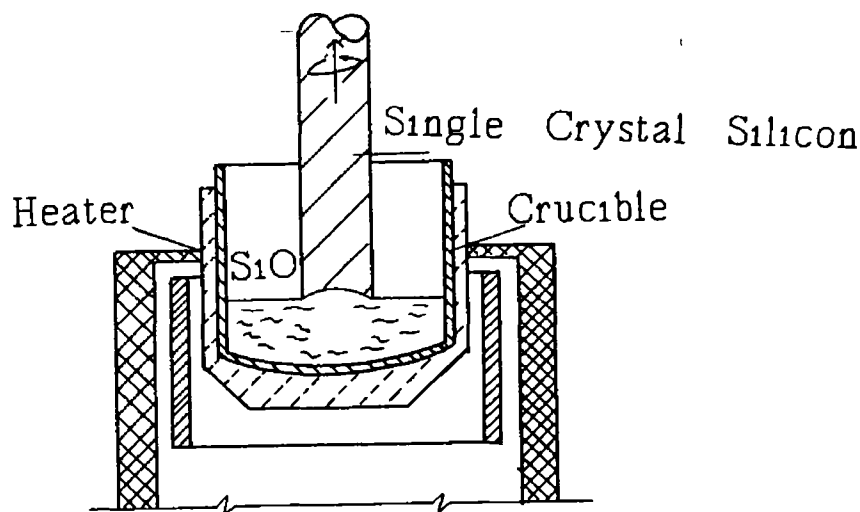
Figure 1 3  Czochralski method of silicon crystal growth.

and purification techniques  The two most common techniques employed are known as float zone (FZ) and Czochralski (CZ)  CZ silicon accounts for almost 80% of the total industrial output  The basic principle is that of pulling, against gravity, a single crystal from a silica crucible containing molten silicon, as illustrated in figure 1 3  During crystal growth the molten silicon reacts with the silica of the crucible according to

$$Si + SiO_2 \rightarrow 2(SiO) \qquad\qquad 1.2$$

Typical concentrations of oxygen in CZ silicon are $10^{18}$ cm$^3$  Normally, the majority of the oxygen is in the dissolved state, where a single oxygen atom occupies an interstitial lattice site and will preferentially bond to two nearest neighbour silicon atoms
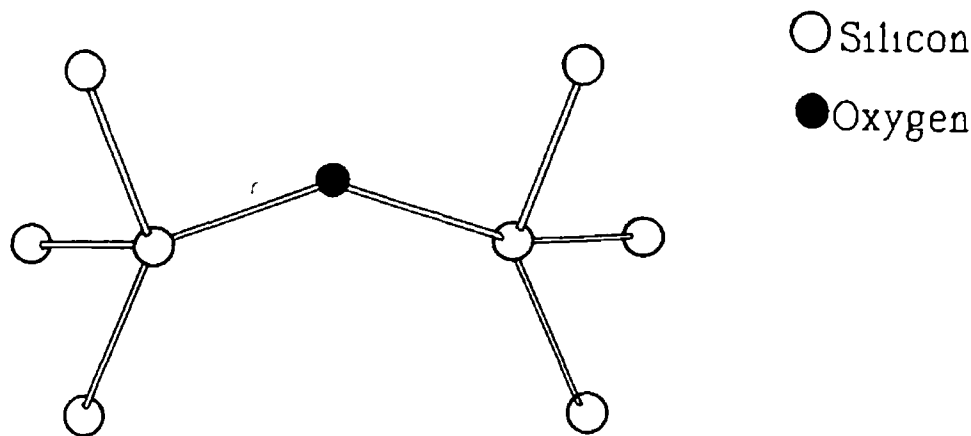


*Figure 1 4  Interstitial location of the oxygen atom in silicon*

[8], a model of this defect is shown in figure 1 4  X-ray diffraction measurements show that dissolved oxygen leads to an increase in the lattice parameter, suggesting the interstitial location [9]  The presence of interstitial oxygen in such high concentrations can induce both positive and negative effects on the optical and electrical properties of the material, we will mention briefly some of these effects

## 1.3.1 Thermal Donors

An inconvenient property of oxygen in silicon is its ability to form donors in the temperature range 300°C to 500°C and especially at 450°C  A series of shallow energy levels, known collectively as thermal donors, is observed, a typical photoluminescence

TD(TO)    96 HOURS

NP x10

B(TO)

P
B

9175  9200  9225  9250  9275  9300

FE(TO)    TA    NP

8600  8700  8800  8900  9000  9100  9200  9300  9400
WAVENUMBERS
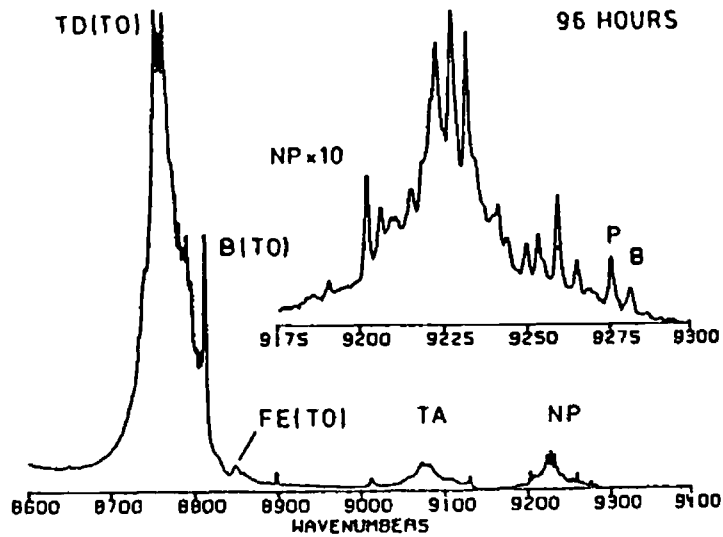
*Figure 1 5  Photoluminescence spectra of Thermal Donors formed in oxygen rich silicon annealed for 96 hours at 450°C*

spectrum is shown in figure 1 5 [10]   It is not yet clear which atomic species constitute the core of the donors, nor the diffusing species which are captured to build up a series of up to nine different levels, often labelled TD1  TD9 [11]

This effect was first reported by Fuller et al [12], who assumed that the donor consists of an $SiO_4$ complex  This assumption was made on the basis that the oxygen donor concentration was small compared to the oxygen concentration but grows rapidly with increasing oxygen content, proportional to the fourth power of the oxygen concentration  However, this conclusion was not generally accepted

A further proposal was that the donors were considered to be structured clusters of pairs of oxygen atoms, but the diffusion coefficient is too low to account for nine separate donor species containing up to 18 oxygen atoms  More recently, it has been suggested that silicon self interstitials, released as two interstitial oxygen atoms combine to form an $O_2$ dimer, may play a crucial role in thermal donor production [13]

The observation of thermal donors is usually explained in terms of a family of agglomerates incorporating a growing number of oxygen atoms [9]

## 1.3.2 Oxygen Induced Stacking Faults

If, during device production, oxygen precipitates at or near the wafer surface, stacking faults will be formed  This will affect device performance as the stacking

faults will lie within the active region of the devices which may cause device failure by leakage currents, filamentary shorts and reduced lifetimes. This may be prevented by suitable device processing whereby oxygen precipitates and stacking faults are only formed deep within the wafer, thereby leaving a sufficiently deep defect free layer in which to form the active regions of devices.

Lattice defects, such as the stacking faults described above, when formed deep within the wafer may be beneficial to device production. Firstly, they act as intrinsic gettering centres for fast diffusing impurities like Cu, Fe, Na and Ag which can all affect device performance. Secondly, they cause precipitation or particle hardening of the lattice which inhibits the extension of dislocations. particularly during high temperature processes. Intrinsic gettering is the greatest advantage of CZ grown material as without it VLSI technologies would not be possible.

## 1.4 Complexing of Oxygen with Extrinsic Impurities

We have seen how the presence of oxygen in silicon is essential for device production and how it can influence many aspects of the material from defect production to the mechanical strength of the material. Oxygen is also considered to be one of the most important defect forming elements in CZ silicon. We will now examine the behaviour of oxygen when extrinsic impurities are introduced.

As described in section 1.2, oxygen is incorporated into silicon as isolated interstitial atoms with preferential bonding to two adjacent silicon atoms. Being an interstitial atom, diffusion occurs readily and is thermally activated according to equation 1.1, where $D_0 = 0.25$ cm$^2$s$^{-1}$ and $E_a = 2.50$ eV [14]. Diffusion of the oxygen atom occurs by an elementary step in which it jumps from one <111> bond to an adjacent one. Migration of the oxygen allows complexing with other impurities, either native to the silicon or introduced via ion implantation or diffusion processes. Defects of this nature have constituted an area of continuing interest in semiconductor research. Early work revealed that lithium-oxygen complexes show donor activity [15]. A variety of carbon-oxygen complexes is produced by thermal annealing of radiation damaged silicon [1]. More recently, nitrogen-oxygen defects have been attributed to the origin of donor activity in CZ silicon [16]. Of the group III impurities, boron and

aluminium have been reported to complex with oxygen [17], [18] and [19] For boron, the existence of B-O defects has been inferred from DLTS measurements [14] and recent photoluminescence data on thermally annealed CZ silicon doped with boron have been interpreted as evidence of B-O defect formation [16]

Two families of defects with particular relevance to this work are those resulting from irradiation with light ions and defects formed when group II impurities are introduced into the material Each of these areas will be addressed in the following section

### 1.4.1 Damage Related Centres Containing Oxygen

Radiation damage induced by high energy particles is of fundamental importance to the production of a wide variety of optically and/or electrically active defect centres Radiation damage can result from many sources including electron irradiation, ion implantation and others such as neutron, gamma and x-radiation If the incoming particle possesses sufficient energy such that a host atom will be displaced from its lattice site through a sufficient distance that the bonds pulling the atom back to its lattice site are broken then damage will result In this manner an interstitial atom and a vacancy are created The penetration depth of the incoming particle depends strongly on the energy and mass of the incoming particle together with the species present in the host lattice and its associated bond structure In the case of electron, neutron, γ-ray and x-ray irradiation, damage will occur as described above However in the case of ion implantation the incoming particle will also come to rest within the host lattice thus introducing damage and an impurity into the lattice which may also complex to form a defect centre

The damage process may be viewed as occurring in two stages Firstly, enough energy must be supplied to the silicon atom of the host lattice in order that it is displaced from its lattice site Secondly, the displaced atom must not undergo correlated recombination with the vacancy Therefore, an individual damage event can result in the production of a vacancy-interstitial pair If, following the collision process that produces the vacancy and interstitial pair, the incoming particle retains a considerable fraction of its kinetic energy, it may have the ability to create a further interstitial atom and vacancy. This process will be repeated until the incoming atom losses all of its kinetic energy

When CZ silicon is irradiated with electrons or ions a number of defects are formed which can be directly attributed to the presence of oxygen in significant quantities   Most notable among these is the "C centre"   This defect forms a luminescence band with the principal zero phonon energy line at 789 4 meV [18] Isotope substitution experiments show that the centre contains at least one carbon atom and at least one oxygen atom [20] [21]   The formation process of this defect can be summarised as follows   Substitutional carbon $(C_s)$, which is mobile at room temperature, is found in as-grown CZ silicon in concentrations exceeding $10^{17}$ cm$^3$ Radiation damage creates silicon self interstitials (I) which are highly mobile at room temperature   I are captured by $C_s$ to create carbon interstitials $(C_i)$,

$$I + C_s \rightarrow C_i$$   1 3

$C_i$ are highly mobile at temperatures T > 300 K, with a diffusion rate considerably exceeding that of $C_s$ atoms   The mobile $C_i$ atoms can react readily with the $O_i$ atoms to form the C centre,

$$C_i + O_i \rightarrow C_i O_i$$   1.4
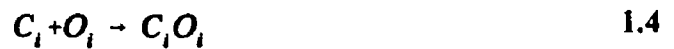
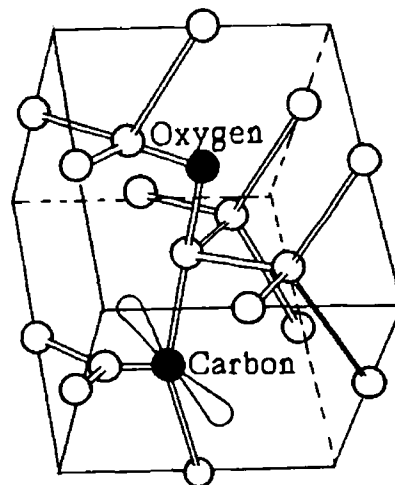Uniaxial stress perturbations show that the centre has a monoclinic I symmetry



Figure 1 6   Model of the "C Centre", containing a $C_i$ and an $O_i$ atom.

[22][23] This centre has been identified in both it's infra-red active modes and it's electronic transitions. It can also be observed in paramagnetic resonance as the "G15" transition [24]. A model for the defect has been derived and is illustrated in figure 1 6

The $C_i$ atoms have a tendency to complex with other impurities, one example of this is the "G centre", consisting of a $C_i$ atom plus a $C_s$ atom,

$$C_i + C_s \rightarrow C_i C_s \qquad\qquad 1.5$$

This centre has a luminescence band with principal zero phonon line at 969 meV [25]

The "P centre" with zero phonon line at 767 meV has also been shown to contain both carbon and oxygen [26]. A comparison of both the C and P centres show that they are identical with respect to their carbon and silicon constituents, but different with respect to oxygen. This defect is readily produced in heat treated silicon as well as in irradiated silicon [23]

## 1 4 2 Oxygen and Group II Related Defects

Oxygen has long been associated with group II elements in the formation of oxides such as zinc-oxide and beryllium-oxide. These are extremely stable compounds as the oxygen atom with an electronic configuration of $1s^2$ $2s^2$ $2p^4$, has an outer p shell and so readily reacts with group II elements, all of which contain an outer filled s shell. The bonding mechanism of these materials is largely ionic e g $Zn^{2+}$ $O^2$, with the outer shell of the group II element supplying two electrons to the oxygen atom. Defects which incorporate group II elements and oxygen in semiconductors have been identified, for example efficient red luminescence characteristic of Zn-O or Cd-O double-doped GaP originates in electronic transitions at nearest neighbour $Zn_{Ga}$-$O_P$ or $Cd_{Ga}$-$O_P$ pairs which form isoelectronic compound constituents [27]. GaP Be and Ga Mg produce characteristic spectra containing no-phonon transitions near 2 18 eV. The transitions are associated with $Be_{Ga}$-$O_P$ or $Mg_{Ga}$-$O_P$ nearest neighbour pairs [24]

In silicon the complexing of oxygen is an important topic as oxygen complexes may provide a means of controlling the oxygen in such a manner as to prevent the formation of unfavourable defects. A recent photoluminescence study of zinc diffused

material shows two separate PL spectra with zero-phonon line energies at 1129 82 and 1090 68 meV [28]  A new luminescence system has been identified in cadmium implanted silicon [29], again believed to be associated with oxygen

Beryllium was reported to complex with oxygen in silicon by Robertson [30] The removal of the 9 μm infra red absorption peak from oxygen rich silicon doped with

**Wavelength (μm)**

7    8    9    10

60

Si(0)

Si(0,Be)

% Transmission

40

20

T = 10°K
t = 24 cm

0

1600    1400    1200    1000

**Wavenumbers (/cm)**
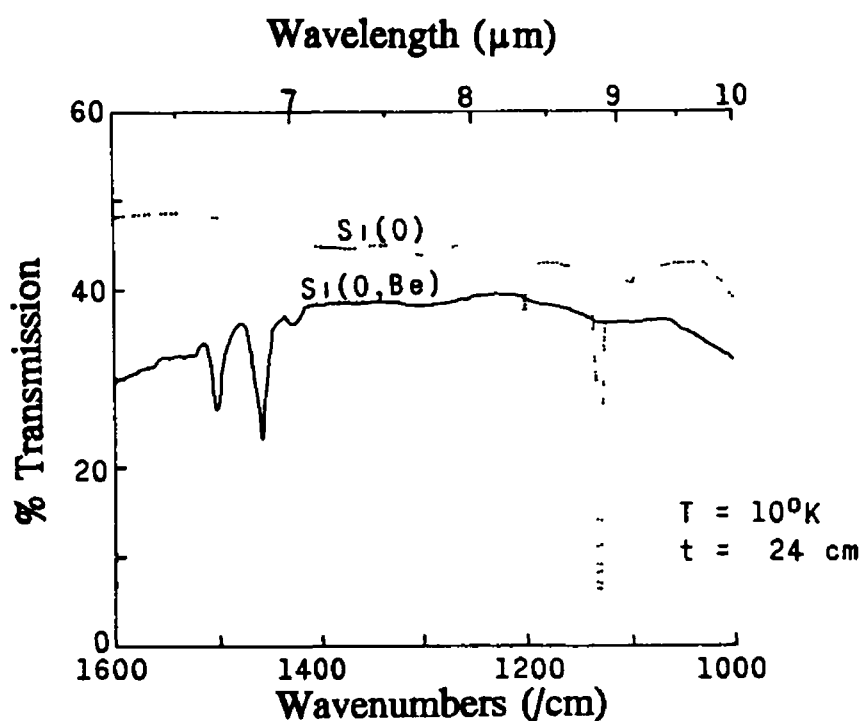
*Figure 1 7  Absorption spectra of oxygen-rich silicon before and after beryllium doping*

Be suggested the formation of Be-O complexes within the silicon lattice  The spectra shown in figure 1 7 illustrate the effect of Be doping on the infrared absorption spectrum   A more recent study by Gerasimenko et al [31] identified two luminescence lines at 1 1382 and 1 0528 eV in Be implanted Si  Since these lines were not exhibited by oxygen lean FZ material they were attributed to Be-O complexes  No further work was reported on these complexes  The complexing of the group II impurity Be forms the basis of this research and so this topic will be addressed in greater depth in section 1 5

## 1.5 Beryllium Doped Silicon

Be together with other group II impurities have been studied in germanium and have been found to behave as substitutional double acceptor impurities [32]   In silicon we would expect a similar situation, however this is not the case   For example, doping with Mg produces n-type silicon as the Mg atom occupies an interstitial lattice site [33]   Be doping, on the other hand, produces p-type silicon and the Be atom is therefore believed to occupy a substitutional site   Crouch et al [34] propose that, due to the very fast diffusion rate of Be in Si, interstitial diffusion is indicated and leads one to expect beryllium to be an interstitial impurity   However, as Be produces p-type material it appears that the mobile interstitial beryllium becomes trapped at vacancies thus producing a substitutional acceptor impurity   Since the early 1970's research into Si Be has continued in an attempt to identify Be related complexes, table 1 1 contains a summary of the main findings

It has been suggested that an acceptor level at 191 9 meV above the valence band, is due to isolated substitutional Be [34]   A recent piezospectroscopic study indicates that the center is a tetrahedral double acceptor, supporting this suggestion [35]   A second acceptor level at 145 meV above the valence band is believed to consist of two Be atoms on nearest neighbour sites [34]   The ratio of the absorption coefficients of these two acceptor levels depends strongly on cooling rate   When samples are quenched the 191 meV level is dominant, whereas upon cooling slowly the 145 meV level is favoured   During quenching it is believed that the pair formation of the 145 meV level dissociates to the single substitutional 191 meV level [34]

When lithium is diffused into Be doped silicon, it produces two acceptor levels at 106 and 81 meV above the valence band, these behave in a similar way to the Be induced acceptor levels when subjected to annealing and quenching treatments [34] They are believed to consist of a Li atom trapped close to each of the two Be defects [34]

The ability of hydrogen to passivate impurities is a topic of current research interest.   Hydrogen diffuses interstitially and would be expected to partially passivate beryllium (double acceptor) leading to single hole acceptors   Crouch et al [36] performed infra-red absorption of Si Be which was heated in a hydrogen environment revealed two acceptor levels at 91 and 73 meV above the valence band   Quenching and

annealing studies indicated that these levels are due to beryllium-hydrogen pairs, a direct analog to the Be-Li pairs [36]   Muro and Sievers [37] found a large energy shift upon upon substitution of H with D   At very low temperature they found one

| Acceptor Levels | | |
|---|---|---|
| Energy Level (meV) | Identity | Reference |
| $E_v$ + 191 9<br>$E_v$ + 145 | Be (substitutional)<br>2 Be (n n sites) | [34] |
| $E_v$ + 106<br>$E_v$ + 81 | Be (sub ) + Li<br>2 Be (n n s) + Li | [34] |
| $E_v$ + 91<br>$E_v$ + 73 | Be (sub ) + H<br>2 Be (n n s) + H | [36] |

| Photoluminescence Centres | | |
|---|---|---|
| Energy (ZPL) (meV) | Identity | Reference |
| 1076 | Be Pair - Isoelectronic | [41] |
| 1117 | Be Pair + Carbon | [45] |
| 1138 2<br>1052 8 | Be + O ?<br>Be + O ? | [31] |
| 1066 5<br>1013 4<br>917 5 | Be ?<br>Be ?<br>Be ? | [31] |

Table 1 1   Acceptor levels and luminescence defects in which Be is incorporated

hydrogenic line series and with increasing temperature a new series originating from thermally populated higher 1s states appeared   It was concluded that the Be-H complex

is dynamic with the hydrogen undergoing a tunnelling process Theoretical calculations suggest the hydrogen resides at a hexagonal interstitial site next to Be [38] The energy barrier between neighbouring sites was found to be of the order of 0 1 eV, compatible with the tunnelling model [39]

Mass spectroscopy data [34] indicate that only about 10% of the beryllium occupies electrically active sites Much work has centered on determining the nature of the remaining beryllium atoms Electrically inactive, *isoelectronic*, substitutional interstitial beryllium pairs are believed to account for most of the remaining Be atoms [40] Intense luminescence from this defect has been interpreted as arising from an exciton bound to an axial isoelectronic defect consisting of two Be atoms sharing a Si site This centre has associated with it a principal zero phonon line at 1076 meV which has been studied using infrared absorption [41] and photoluminescence [42][43] Zeeman [38] and uniaxial stress data [44] were originally interpreted as evidence for a <100> axis of symmetry, subsequently the data were found to be consistent with a <111> symmetry axis Tarnow et al [46] also determine a [111] symmetry axes from their calculations Luminescence from this defect is often accompanied by a weaker set of lines lying at higher energy A correlation between the intensity of these lines and the concentration of carbon in the sample led to the suggestion that the lines were associated with the Be pair centre perturbed by a nearest neighbour C atom [45]

Low temperature photoluminescence spectroscopy by Gerasimenko et al [31] revealed a number of radiative recombination centres which were assumed to contain beryllium atoms Figure 1 8 reproduces the annealing behaviour of the luminescence lines observed Two new luminescence lines were observed at 1 1382 and 1 0528 meV Since these lines were exhibited in oxygen rich silicon and not in oxygen lean silicon it was concluded that they were due to Be-O complexes In the present work Be implanted silicon produced a photoluminescence system with principal zero phonon line at 1137 98(5) meV together with an sideband structure containing both lattice and local modes as illustrated in figure 1 9 The zero phonon line of this centre is believed to coincide with the line labelled 1 1382 eV of Gerasimenko et al , while the line labelled 1 0528 eV is in fact a local mode of the same system Three lines produced by Gerasimenko et al as yet remain unidentified in terms of their chemical nature However, their annealing behaviour is reminescent of damage induced defects as their

eV

Be Pair + C
1 1156

L3
1 0528

700    400    600

700    400    600

Be Pair
1 0786

1 0134

700    400    600

700    400    600

1 0665

0 9175

700    400    600

700    400    600

BeA
1 1382

200    400    600
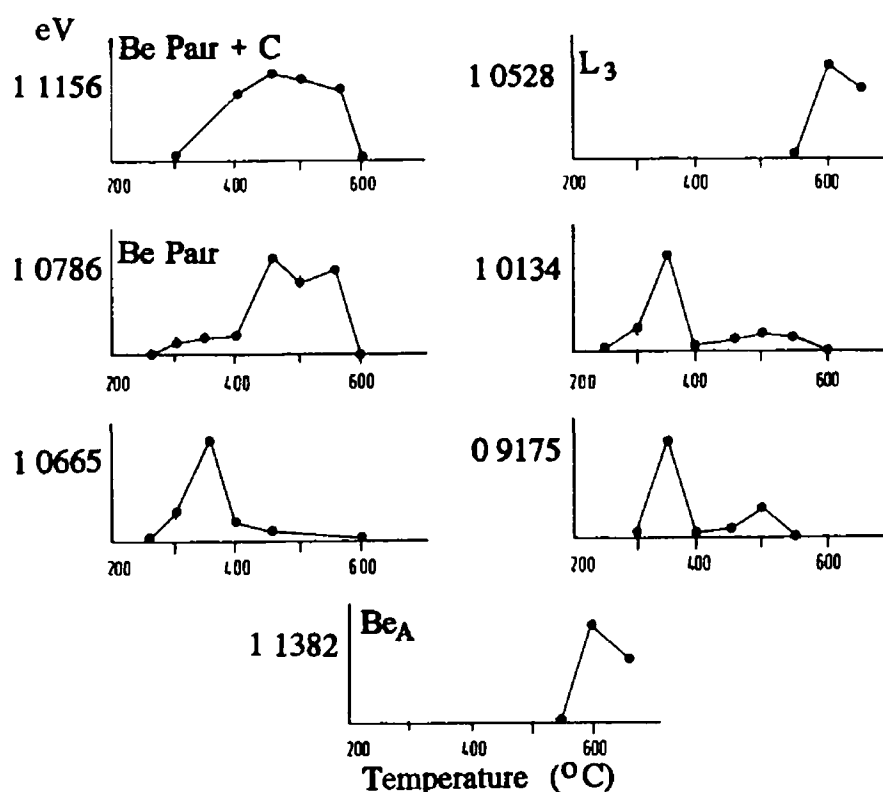
Temperature (°C)

*Figure 1 8  Normalised intensities of luminescence lines from centres believed to contain Be, from reference [30]*

intensity is substantially reduced above 400°C, the temperature at which most damage products are annealed out of the silicon lattice  No further work is reported on the nature of the Be-O related defect, the present work is mainly concerned with determining the nature of this defect

Ab initio calculations carried out by Tarnow et al [46] confirm that substitutional Be is an energetically favourable position  In that work the formation energies of a multitude of Be defect structures ranging from the simplest monatomic defects to more complex defect clusters were investigated  For single substitutional and interstitial beryllium atoms the authors concluded that the substitutional site is energetically more favourable than either of the two available interstitial sites  Table 1 2 gives the results of their calculations for single substitutional and interstitial sites  The lattice relaxations are largest for the substitutional site, the Be-Si bond length being 2 25 Å which is 4% shorter than the Si-Si bond length
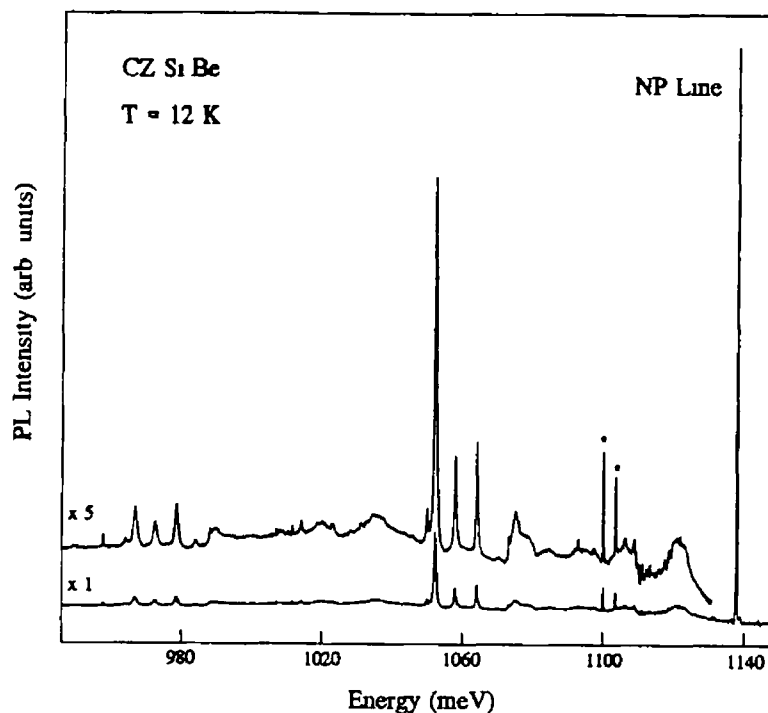
*Figure 1 9  Photoluminescence spectrum of Be implanted CZ Si annealed at 600°C  The features marked * are not part of the Be_A spectrum.*

| Defect Type | Energy |
|---|---|
| Substitutional Be | 1 1 ± 0 5 eV |
| Tetrahedral Interstitial | 1 0 ± 0 2 eV |
| Hexagonal Interstitial | 1 5 ± 0 2 eV |

*Table 1 2  Energies of the isolated substitutional and interstitial Be defects in Si   The zero of energy is chosen to be the energy of Be in its metallic form [30]*

## 1.6 Conclusions

In this chapter, the origins of defect structures in silicon were introduced, particular emphasis was placed on the formation kinetics of defects in silicon which are related to the presence of oxygen and related to damage processes  The present

knowledge of Be related defect structures already charactensed in silicon was also presented A defect structure likely to contain Be and O was tentatively identified and forms the subject of this thesis

In chapter two, the ongin of the charactensttc band structure found in silicon will be addressed with particular emphasis on the introduction of energy levels into the otherwise forbidden energy gap of the matenal by defect structures The use of photoluminescence spectroscopy to probe these energy levels will be considered as will the nature of typical defect related PL spectra In chapter three, the use of perturbation techniques in conjunction with PL spectroscopy as a means of uncovenng the axial symmetry of defects is descnbed, the necessary theory will be developed in order to analyse the data obtained in this work Chapter four contains details the expenmental techniques used throughout this work Chapters five and six contain the new data obtained dunng the course of this work together with an analysis of same In chapter seven a new technique involving the use of radioactive isotopes in photoluminescence spectroscopy is introduced with particular reference to how the technique could be applied to the further analysis of this and other defects Conclusions drawn from the data obtained together with suggestions for further work are presented in chapter 8

**References:**

[1] G Davies, Physics Reports 3 & 4 (1989) 83

[2] S Perkowitz Optical Characterisation of Semiconductors Academic Press (1993)

[3] P J Drevinsky, C E Caefer, S P Tobin, J C Mikkelsen and J R Kimerling, Mat Res Soc Symp Proc 104 (1988)

[4] T Y Tan, E E Gardner and W K Tice, Appl Phys Lett 30, 175 (1977)

[5] R A Craven, in *Semiconductor Silicon*, edited by H R Huff, R J Krieger and Y Takeishi (Electrochemical Society, Pennington, Nj, 1981), 254

[6] W Kaiser, P H Keck and Lange, Phys Rev 101 (1956) 1254

[7] H J Hrostowski and R H Kaiser, Phys Rev 107 (1957) 966

[8] R K Watts in Point Defects in Crystals (John Wiley and Sons) 180

[9] W L Bond and W Kaiser, J Phys Chem Solids 16 (1960) 44

[10] A C T Drakeford and E C Lightowlers Defects in Electronic Materials Symp, Boston, MA USA (Pittsburgh, PA, USA Mater Res Soc 1988) 209

[11] M Stavola, Mater Res Soc Proc 59 (1986) 7

[12] C S Fuller and J A Ditzenburger, J Appl Phys 27 (1956) 544

[13] R C Newman, J Phys C Solid State Phys 18 (1985) L967

[14] Landolt-Bornstein "Numerical Data and Functional Relationships in Science and Technology, Group III Crystals and Solid State Physics" Volume 17 Technology of Si, Ge and SiC Section 6 1 4 1 Editors O Madelung, M Schultz and H Weiss (Springer-Verlag Berlin 1984)

[15] E M Pell, Solid State Phys Electron Telecommun 1 (1960) 261

[16] M Suezawa, K Sumino, H Harada and T Abe, Japan J Appl Phys 25 (1986) L859

[17] P.J Drevinsky and H M De Angelis, Proc 13th Int Conf Defects in Semiconductors ed L C Kimerling and J M Parsey Jr (Warrendale, PA The Metallurgical Society of AIME) (1988) 807

[18] A La Ferla, L Torrisi, G Galvagno, E Rimini, G Ciavola, A Carnera and A Gasparotto, Appl Phys Lett 62 (1993) 393

[19] J J Van Kooten, T Gregorkiewkz, A J Blaakmeer and C A Ammerlaan, J Phys C Solid State Phys 20 (1987) 2183

[20] G Davies, E C Lightowlers, R A Woolley, R C Newman and A S Oates, J Phys C **17** (1984) L499

[21] K Thonke, G D Watkins and R Sauer, Solid State Comm **51** (1984) 127

[22] K Thonke, A Hangleiter, J Wagner and R Sauer, J Phys C **18** (1985) L795

[23] C P Foy, J Phys C **15** (1982) 2059

[24] J M Trombetta and G D Watkins, Mater Res Soc Proc **104** (1988) 93, Appl Phys Lett **51** (1987) 1103

[25] L W Song, B W Benson and G D Watkins Appl Phys Lett **51** (1987) 1155

[26] W K Kurner, R Sauer, A Dorner and K Thonke, Phys Rev B **39** (1989) 13327

[27] P J Dean and M Ilegems, Journal of Luminescence **4** (1971) 201

[28] M O Henry, J D Campion, K G Mc Guigan, E C Lightowlers, M C do Carmo and M H Nazare, Semicond Sci and Tech **9** (1994) 1375

[29] E McGlynn, Private Communication

[30] J B Robertson, American Physical Society Meeting (1968) unpublished

[31] N N Gerasimenko, B A Zaltsev, L N Safronov and L S Smirnov, Sov Phys Semicond **19** (1985) 762

[32] P Fisher and H Y Fan, Phys Rev Lett **5** (1960) 195

[33] J B Robertson and R K Franks Solid State Commun **6** (1968) 825

[34] R K Crouch and J B Robertson, Phys Rev B **5** (1972) 3111

[35] J N Heyman and E E Haller, Bull Am Phys Soc **36** (1991) 862

[36] R K Crouch, J B Robertson, H T Morgan, T E Gilmer, Jr and R K Franks J Phys Chem Solids **35** (1974) 833

[37] K Muro and A J Sievers Phys Rev Lett **57** (1986) 897

[38] P J H Denteneer, C G Van de Walle and S T Pantelides, phys Rev Lett **62** (1989) 1884

[39] E E Haller Physica B **170** (1991) 351

[40] N Killoran, D J Dunstan, M O Henry, E C Lightowlers and B C Cavenett, J Phys C **15** (1982) 6067

[41] D Labrie, T Timusk and M L Thewalt, Phys Rev Lett **52** (1984) 81

[42]    M O Henry, E C Killoran, D J Dunstan and B C Cavenett, J Phys C 14 (1981) L255

[43]    M L Thewalt, S P Watkins, U O Ziemelis, E C Lightowlers and M O Henry, Solid State Commun 44 (1982) 573

[44]    M O Henry, K A Moloney, J Treacy, F J Mulligan and E C Lightowlers, J Phys C 17 (1984) 6245

[45]    D Labrie, I J Booth, S P Watkins and M L W Thewalt, Solid State Communications 63 (1987) 115

[46]    E Tarnow, S B Zhang, K J Chang and D J Chadi, Phys Rev B 42,17 (1990) 11252

# Chapter 2
# Band Structure and Recombination Processes in Semiconductors

## 2.1 Introduction

Impurities and defect complexes can induce energy levels within the forbidden energy gap of a semiconductor Optical spectroscopy provides a means of probing transitions between these levels and with the valence and conduction band continua In this chapter the band structure of semiconductors will be considered as will the recombination processes associated with various types of defects Relevant theoretical phenomena will be developed in order to provide a basis on which to analyse the data obtained in this work

## 2.2 Band Structure of Semiconductor Materials

The concept of a solid having a series of allowed energy bands is a familiar one and stems from our understanding of a single isolated atom represented as having a
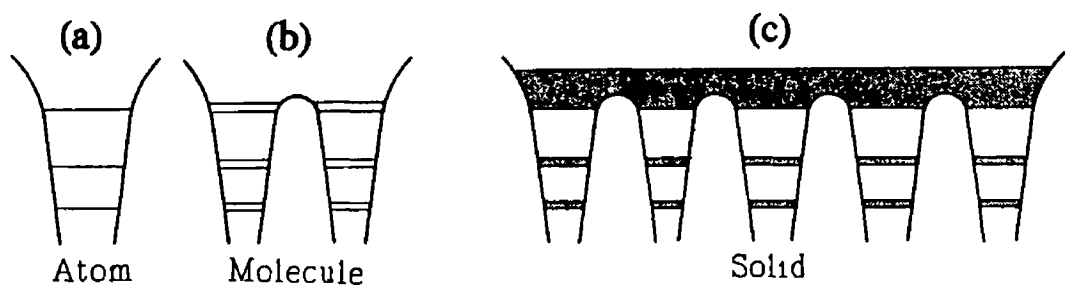


*Figure 2 1   Creation of a band structure within a semiconductor   The evolution of the energy spectrum from an atom (a), to a molecule (b), to a solid (c)*

series of discrete energy levels lying in a potential well   When a second atom is brought sufficiently close to the first so that their electronic wave functions overlap, all of the spin paired electrons acquire energies slightly different from their original isolated values   The energy spectrum of such a system will consist of a series of discrete doublets   If we now consider a solid having N similar atoms, which give rise to 2N electrons of the same orbital type occupying 2N different electron states, we find that the N sublevels being so closely spaced can be considered to form continuous energy bands, separated by regions in energy for which no electron states exist, termed energy gaps, as illustrated in figure 2 1   The relative magnitude of the energy gap will determine the conductive properties of the material and so allow us to differentiate between metals, semiconductors and insulators

The existence of such energy gaps can be derived from a quantum mechanical point of view by solving the Schrodinger equation for an electron as it moves through the crystal   The crystal will have a potential V(r) which will have the periodicity of the crystal lattice i e   the electron will experience a periodic potential as it moves through the crystal   In this model the Schrodinger equation can be written as,

$$\left[\left(\frac{\hbar^2}{2m}\right)\nabla^2 + E - V(r)\right]\Psi(r,k) = 0 \qquad \text{2.1}$$

The solutions to this equation are the so called Bloch functions

$$\Psi(r,k) = u_k(r)\exp i k.r \qquad \text{2.2}$$

where $u_k(r)$ has the periodicity of the lattice and so will have the same translational symmetry as the real lattice, and k is a vector in reciprocal space   Substituting equation 2 2 into the Schrodinger equation and rearranging we obtain an eigenvalue equation which when solved gives a series of discrete energies which vary continuously with k, as illustrated in figure 2 2   These discrete energy levels bear a one to one correspondence with the energy bands discussed at the beginning of this section

If we consider the crystal as a square well potential bounded by an infinite barrier and having a base of width L, we find that k can have values between
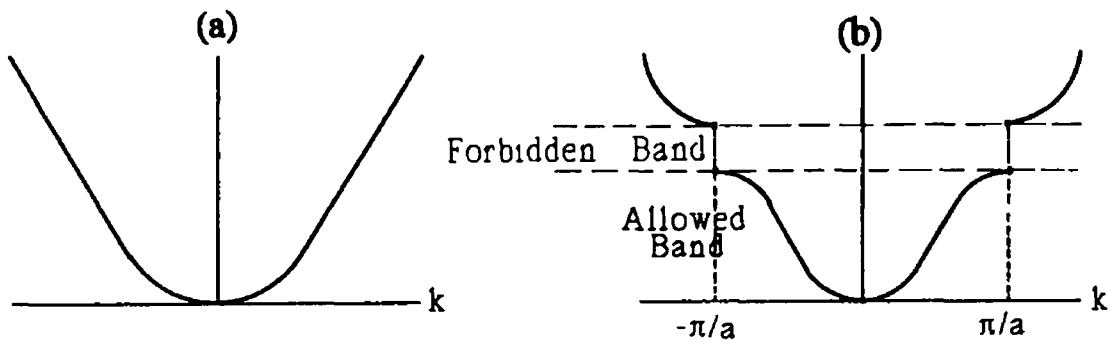
*Figure 2 2  (a) Plot of energy versus wavevector k for a free electron and (b) plot of energy versus wavevector for an electron in a monatomic lattice of lattice constant a*

$$-\frac{\pi}{L} < k < \frac{\pi}{L}$$ 2.3

Hence k = π/L is the maximum significant value of k   This maximum value occurs at



Wavevector   k
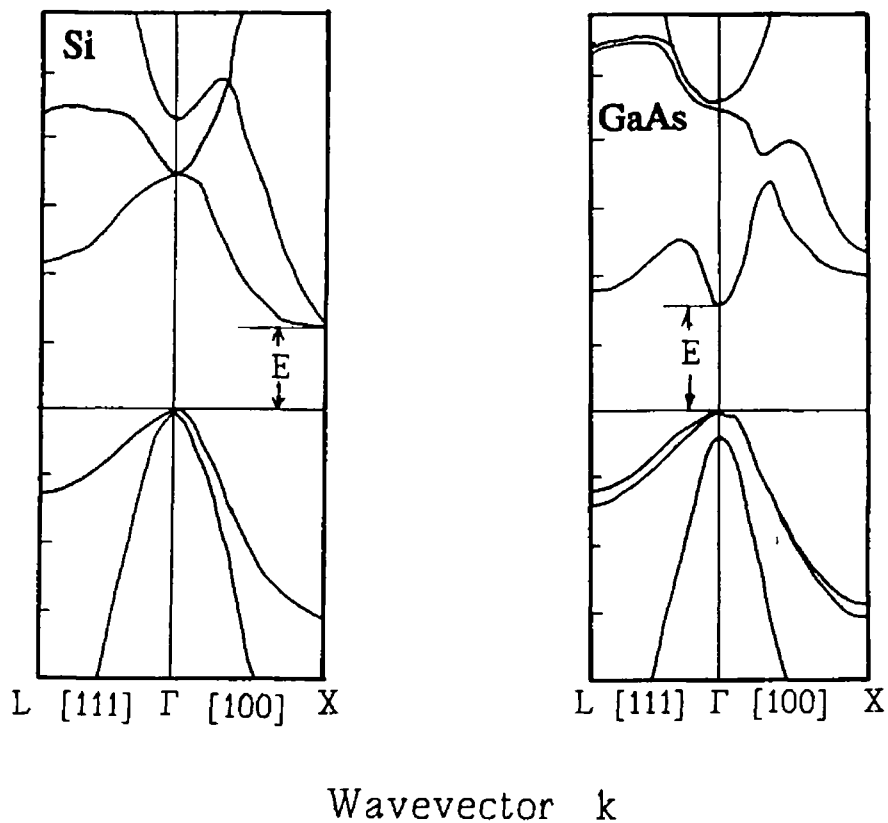
*Figure 2 3   Energy dispersion relations for two semiconductors Si and GaAs   The energy gap (E_g) is shown for the direct gap of GaAs and the indirect gap of Si*

the edge of the Brillouin zone, larger values of k simply repeat the values obtained for the first Brillouin zone, therefore the energy levels in any crystalline solid need only be defined within the limits of equation 2 3, ie within the first Brillouin zone  L in equation 2 3 is proportional to the internuclear distance of the atoms within the crystal lattice  As this distance varies with crystal direction, so also will the band structure Plotting energy values as a function of k in each of the three principal crystal directions (<001>, <110> and <111>), yields the familiar band structure of semiconductors  The band structure of two semiconductor materials is illustrated in figure 2 3

It is clear from figure 2 3 that silicon is an indirect gap material  In the case of indirect gap materials, extrema occur in the lowest lying conduction bands away from the zone centre  The result of this is the conduction band minimum and the valence band maximum occur at different points in k space  For most semiconductors the valence band structure is similar especially at k = 0, the zone centre  The energy gap is the difference between the valence band at k = 0 and the lowest point in the conduction band  When the lowest point occurs at k = 0, the semiconductor is direct gap because a transition can occur at the zone centre with both the initial and final states having the same momentum wavevector, k = 0, as illustrated in figure 2 3  A good example of a direct gap material is GaAs

The most significant result of silicon being an indirect gap semiconductor from an optical spectroscopy point of view is that radiative transitions between the valence band and conduction band cannot readily occur  In any absorption or recombination process both energy and momentum must be conserved  In this case the transition is a two step process  Momentum is conserved via a phonon interaction  A broad spectrum of phonons is available but only those with the required momentum change become involved in the process  Each phonon has a characteristic energy $E_p$  Hence, to complete a band to band transition a phonon is either emitted or absorbed  These two processes are given respectively by

$$h\nu_a = E_f - E_i + E_p \qquad\qquad 2\ 4$$

$$h\nu_a = E_f - E_i - E_p \qquad\qquad 2.5$$

where $E_i$ and $E_f$ are the are the initial and final states involved in the transition  This process is illustrated in figure 2 4
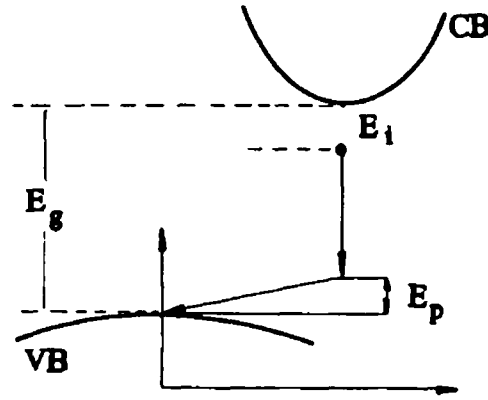
*Figure 2 4   Phonon assisted exciton recombination in an indirect gap material*

## 2.3 Impurity States

When defects are introduced into the crystal, energy levels can appear in the otherwise forbidden energy gap   The electronic states may be divided into two major categories   shallow and deep

Shallow states arise from electron or hole wavefunctions that are delocalised from the defect core and have eigenfunctions that extend beyond their neighbouring atoms   Shallow donors and acceptors, for example, behave in this manner   The electron wavefunctions associated with shallow donors are derived from the conduction band minimum, and similarly the hole wavefunctions of shallow acceptors are derived from the valence band maximum   The extra electron of the donor impurity is, by a Coulombic force, attracted to the impurity nucleus   The energy binding the electron to the nucleus i e the ionisation energy, $E_i$, can be calculated from

$$E_i = \frac{m^* q^4}{2 h^2 \varepsilon^2 n^2} = \frac{m^*}{m \varepsilon^2 n^2} 13\,6 \ eV \qquad\qquad 2\,6$$

where $m^*$ is the effective mass of the electron (which differs from the mass in vacuum by virtue of the crystal field in which it resides) and $\varepsilon$ is the dielectric constant   An approximate radius for the electron can be calculated, corresponding to the quasi-Bohr radius

$$Quasi\text{-}Bohr \ Radius = a_0 \, \varepsilon \, \frac{m}{m^*} \, n^2 = 0\,5292 \, \varepsilon \, \frac{m}{m^*} \, n^2 \quad (\text{Å}) \qquad 2.7$$

where $a_0$ is the lattice constant In the case of the donor the ionisation energy from the ground state to the conduction band is obtained by allowing $n = 1$ A similar situation holds for acceptor levels found above the valence band, in this case it is the effective mass of the hole which is used in equation 2 6

This model is often referred to as the hydrogenic model and is valid when the quasi-Bohr radius is large compared to the lattice constant. For typical semiconductors with $\varepsilon \approx 10$, a quasi Bohr radius of $\approx 50$ Å is obtained which is much larger than the lattice constant

Deep levels are usually found closer to the centre of the band gap Their core potential, which is a tight binding potential rather than a far reaching Coulombic potential, plays a dominant role and so the defects are characterised by highly localised wave functions, in this regime comparison with hydrogen-like states is no longer valid

In calculating the eigenstates associated with deep levels both the conduction band and valence band need to be considered The chemical make up of the centre as well as the lattice surrounding it, influence its energy level system

The binding energy of deep levels cannot be generalised in a simple form as was possible for shallow centres but requires a detailed quantum mechanical analysis such as the self consistent Green's function and the pseudopotential methods [1]


## 2.4 Electron-Hole Recombination Processes in Semiconductors

The electromagnetic radiation emitted due to the recombination of electron-hole pairs in semiconductors is referred to as recombination radiation This is a general term which covers both short and long wavelength radiation whereas "near-band-gap" refers, in particular, to radiation with energy close to that of the band gap Photoluminescence is the reverse process of absorption An electron excited by incident radiation, to a higher energy state de-excites to a lower energy level, usually the ground state, emitting all of the energy difference between the two If there is a multiplicity of excited states only transitions from the lowest excited state will generally be observed due to rapid thermalisation of carriers from the higher excited states The minimum detectable defect

Thermalisation by Phonon Emission
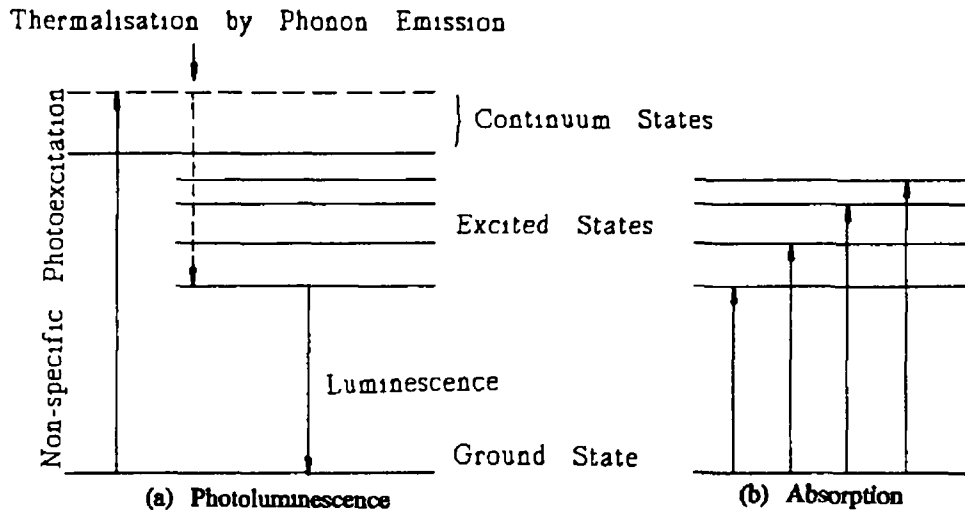


Figure 2 5 *Optical absorption (a) and emission (b) processes in semiconductors*

concentration is usually much lower in luminescence as there is no large background light level present to reduce the signal to noise level   Figure 2 5 illustrates both the absorption and emission process for an energy level system consisting of a ground state together with a series of excited states   A comprehensive review of absorption and luminescence together with other optical characterisation techniques is given by Perkowitz [1]

The main prerequisite needed to detect a transition, either in absorption or emission, is that the system not be in static equilibrium   For this to happen requires some form of excitation to be supplied   Under optical excitation with photon energies greater than the band gap energy, free electrons and holes are produced   Because of the Coulombic attraction between the electron and hole, these particles form mobile pairs known as excitons   The ionization energy of such a system is given by

$$E_x = \frac{-m_r^* q^4}{2 h^2 \varepsilon^2 n^2}$$

2.9

where n is an integer $\geq$ 1 indicating the various exciton states and $m_r^*$, the reduced mass of the exciton, is given by

$$\frac{1}{m_r^*} = \frac{1}{m_e^*} + \frac{1}{m_h^*}$$

2.10

$E_c$

$n = \infty$

$n = 2$

$n = 1$

$E$

$E_v$
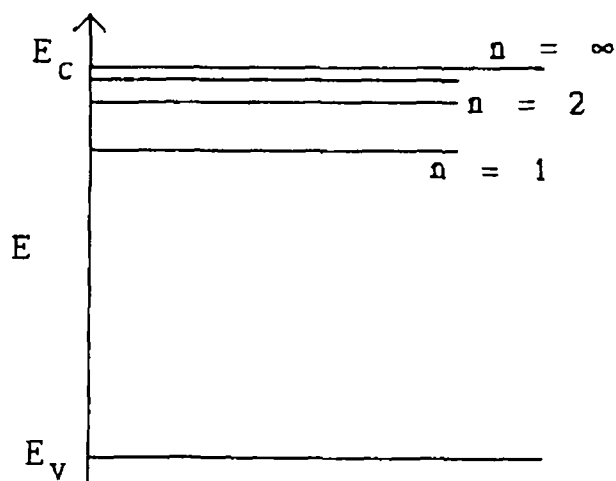
Figure 2 6   Energy level diagram for the exciton and its excited states

Laser excitation hv > $E_g$

Electron hole pairs

Free excitons (FE)

| Capture by shallow donors and acceptors Bound excitons (BE) | Bound multiexciton complexes (BMEC) | Electron hole drops (EHD) at high excitation densities | Capture by neutral defect complexes |

| Non radiative decay Auger effect | Non radiative decay Auger effect | Non radiative transitions |

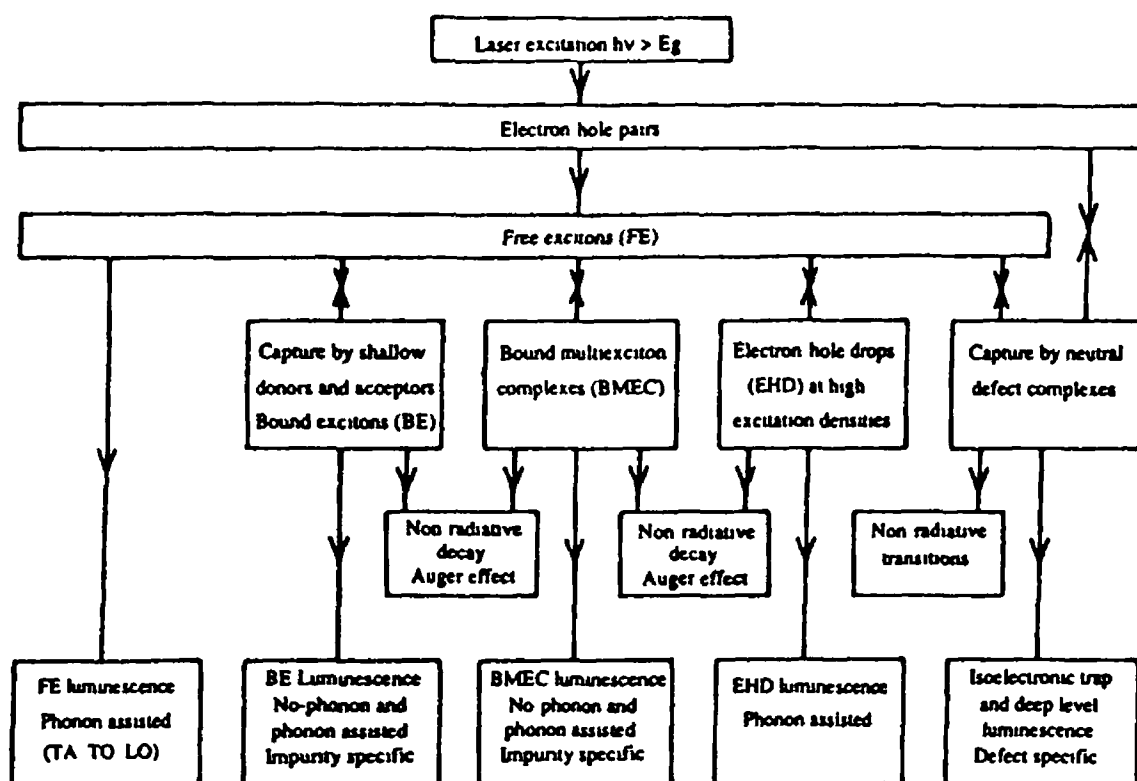| FE luminescence Phonon assisted (TA TO LO) | BE Luminescence No-phonon and phonon assisted Impurity specific | BMEC luminescence No phonon and phonon assisted Impurity specific | EHD luminescence Phonon assisted | Isoelectronic trap and deep level luminescence Defect specific |

Figure 2 7   Luminescence decay processes stimulated by above band gap photo excitation [2]

$m_e^*$ and $m_h^*$ are the electron and hole effective masses, respectively It is usual to regard the conduction band edge as coinciding with the n = infinity level of the exciton The various states of the exciton are then as represented in figure 2 6 The exciton can move

through the crystal as a mobile pair and may eventually recombine  Many recombination processes are available to the exciton, as illustrated in figure 2 7, some of which are radiative giving rise to luminescence while others are non radiative [2]

In high purity material, at low temperatures and relatively low excitation densities many excitons decay by electron - hole recombination giving rise to free exciton (FE) luminescence  If donors or acceptors are present in concentrations $> 10^{15}$ cm$^3$ then at low temperatures practically all of the free excitons may become localised at the impurity where they recombine giving rise to impurity specific bound exciton (BE) luminescence  BE and FE luminescence can occur simultaneously in the same material, in which case each can be identified by its characteristic line width and
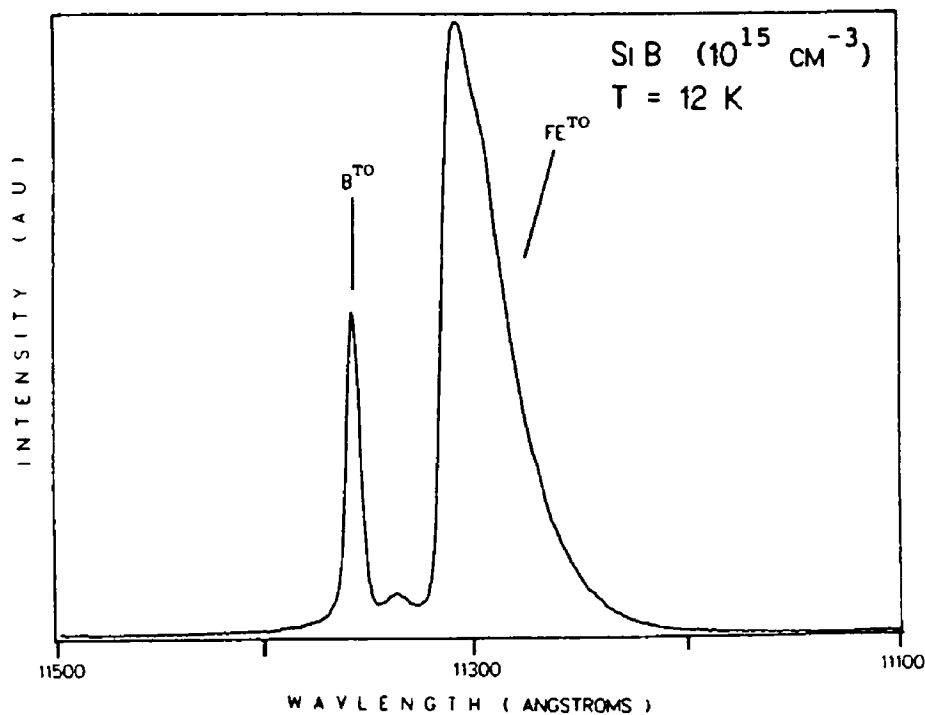


*Figure 2 8   Low temperature spectrum of boron doped silicon containing both free exciton (FE) and impurity specific bound exciton (BE) luminescence*

energies, Figure 2 8 shows a typical low temperature PL spectrum of silicon containing both FE and BE impurity specific luminescence  Bound exciton states often give rise to shallow states in the forbidden gap which means that the FE is bound to the defect with a binding energy of only a few meV  Excitons may also become bound at defect centres with highly localised states, in which case one of the particles is very strongly bound to the centre as in the case of deep electron or hole attractive defects

## 2.5 Excitons Bound to Donors and Acceptors

A simple substitutional donor may bind an exciton in the following manner Initially, an electron is bound by the electron attractive core potential of the impurity, a hole is then subsequently bound by the Coulombic attraction induced by the extra electronic charge The two electrons will have angular momentum $j_e = 1/2$ and will be paired with opposite spins into a singlet, $J = 0$ state, with negligible electron-electron interaction The hole will be loosely bound in an effective mass like manner with a $J = 3/2$ state, with a very weak electron-hole interaction Figure 2 9(a) illustrates a typical spectrum for bound exciton recombination arising from donor bound excitons in silicon

In the case of an exciton bound to an acceptor, the hole is initially bound by the hole attractive core potential and the electron is bound in the Coulombic field of the extra hole charge The two holes have angular momentum $j_h = 3/2$, and split by the hole-hole exchange interaction which results in two hole states $J = 0$ and $J = 2$ Each of these states is then coupled to the electron $(j_e = 1/2)$ resulting in three bound exciton states $J = 1/2$, $3/2$ and $5/2$ Figure 2 9(b) illustrates a spectrum for bound exciton recombination arising from acceptor bound exciton in silicon

An alternative model for bound exciton states was developed by Kirczenow [3] Based on a shell model concept, the electrons and holes in the exciton are assigned to the usual donor and acceptor levels, respectively, with electron-hole interaction neglected The theory has been developed further on the basis of recent high-resolution photoluminescence measurements to include interaction effects [4] The modelling of excitons bound to shallow donors and acceptors is now at a high level of sophistication

## 2.6 Excitons Bound to Neutral Defects

Electrically neutral defects may exist in the crystal lattice and are generally referred to as isoelectronic defects Their existence was first detected in ZnTe O by Dietz [5] and in GaP N by Dean [6] Since then many isoelectronic defects have been identified in a variety semiconductor crystals Such impurities can consist of simple substitution atoms, for example N in GaP, or can be complex in nature such as ZnO and CdO in GaP [7] The core of the defect is considered to posses a short range
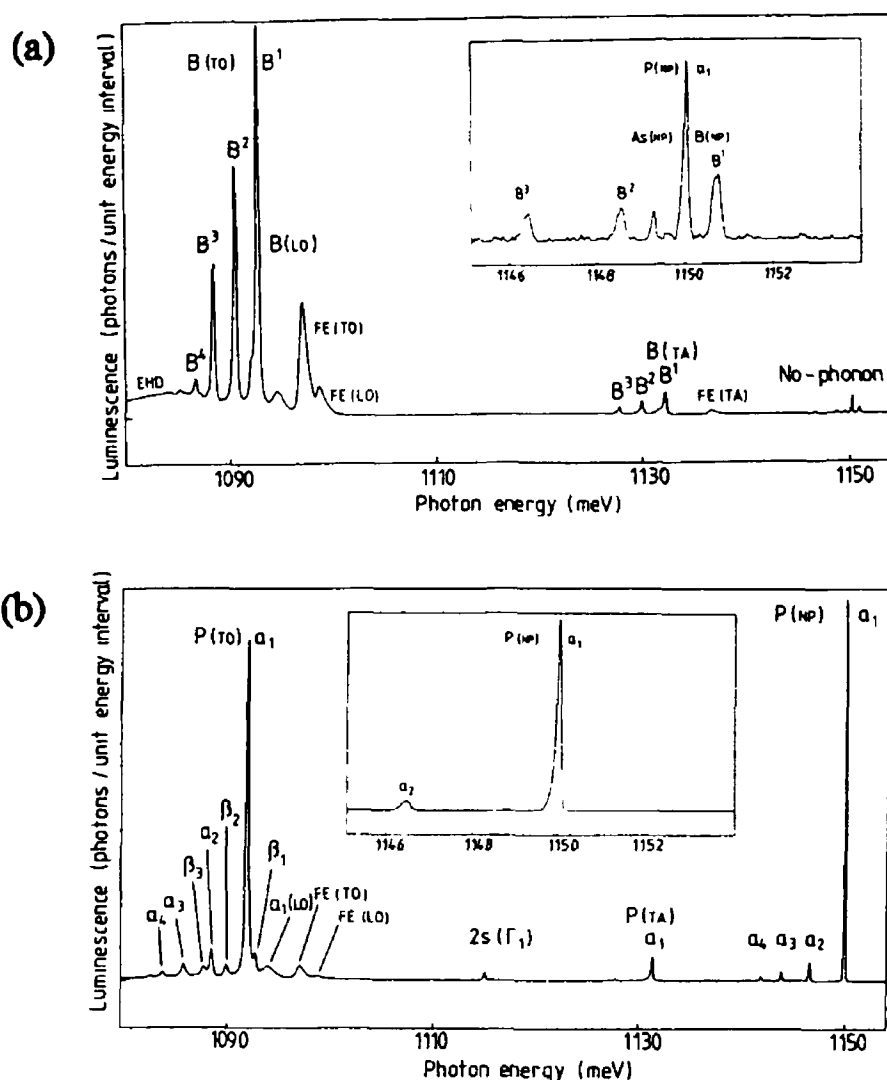
*Figure 2 9   Low temperature photoluminescence spectra of Si showing bound exciton emission due to (a) boron acceptors and (b) phosphorous donors*

interaction due to electronegativity differences or a local strain field about the defect site  This causes the defect to become either electron- or hole-attractive, this model was proposed by Hopfield et al [8]   A second carrier is consequently bound, via the Coulombic potential of the primary particle, into a hydrogen-like orbit   Cohen and Sturge [9] confirmed this model for the near - neighbour $N_p$ - $N_p$ pair in GaP using photoluminescence excitation to scan the absorption spectrum of acceptor-like excited states of the hole which was shown to be bound via a Coulombic potential of a highly localised electron   While the binding of the primary particle is due to the very localised nature of the potential, the delocalised particle is described well in terms of effective

mass theory   Isoelectronic defects can be classed as either "electron-attractive" or "hole-attractive" on the basis of which particle, electron or hole, is primarily bound to the defect.

A schematic representation of an electron attractive defect is illustrated in figure 2 10(a)   The localised electron creates a distributed Coulomb potential, which is partially screened by the core potential of opposite sign   This leads to the capture of the hole   The angular momentum of the electron and hole are $j_e = 1/2$ and $j_h = 3/2$ respectively   Electron-hole exchange interaction will split the bound exciton state into

**(a) Electron Attractive Core**
**"Pseudo-acceptor"**

Electron Energy

Primary Particle

Secondary Particle

Bound Exciton Energy

$j_h = 3/2$
$j_e = 1/2$

$J = 1$

$J = 2$
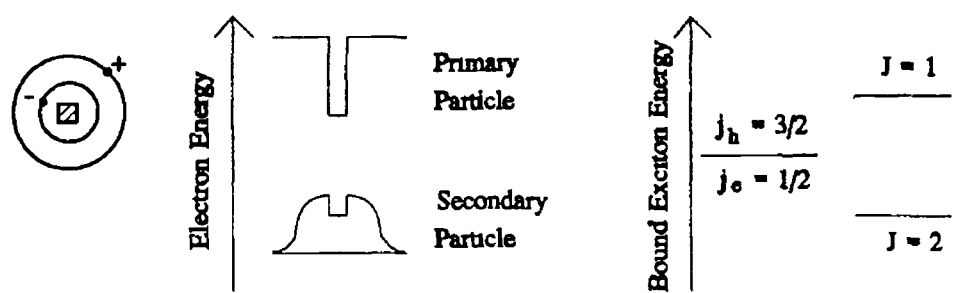
**(b) Hole Attractive Core**
**"Pseudo-donor"**

Electron Energy

Primary Particle

Secondary Particle

Bound Exciton Energy

$s_h = 1/2$
$s_e = 1/2$

$S = 0$

$S = 1$

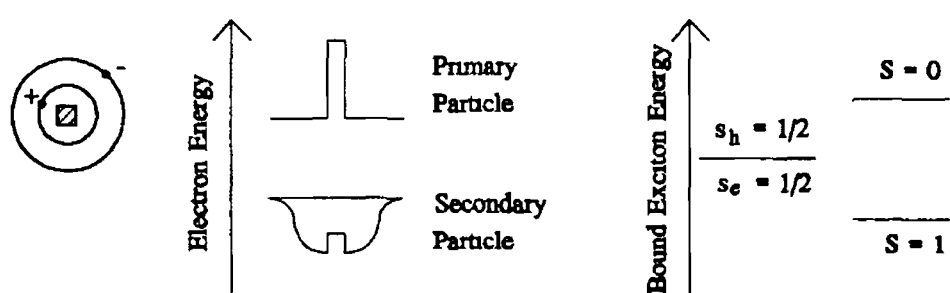*Figure 2 10   Schematic representation of the binding of excitons to (a) electron attractive and (b) hole-attractive defects*

a $J = 1$ and a $J = 2$ state, as illustrated in figure 2 10(a)   These states will be further split by the local defect field, the effect of an axial trigonal field is illustrated   Electrically neutral defects characterised by electron attractive cores are referred to as

pseudoacceptors The luminescence associated with exciton recombination at the Be-related (Be-pair) centre in silicon is pseudoacceptor in nature [10,11] as is the "ABC" centre also observed in silicon [12]

Hole-attractive neutral defects may bind a hole as the primary particle in a very localised potential, and an electron may be subsequently bound in the Coulombic potential of the hole thus completing the bound exciton excitation A schematic representation of such a bound exciton is illustrated in figure 2 10(b) The delocalised electron will have an s-like wavefunction However, the hole may also have an s-like wavefunction, in which case the angular momentum of the hole is said to be quenched In order for the angular momentum to be quenched a very localised wavefunction must exist with an orbitally non-degenerate hole state at lowest energy, such a state may be created by a defect having a low symmetry local strain field The electron, bound in an effective mass-like state, is influenced by the screened electron-repulsive core potential The electron-hole exchange interaction leads to a singlet-triplet bound exciton state as illustrated in figure 2 10(b) Hole-attractive defects such as is described here are referred to as "pseudodonors" Both the C-line [13] and the P-line [14] defects produced in radiation damaged CZ silicon are consistent with the pseudodonor model

Electron-hole recombination at isoelectronic defects leads to very efficient luminescence Since there are no unpaired electronic particles remaining at the isoelectronic centre after recombination, non-radiative Auger processes cannot occur, unlike the situation for excitons bound to donors or acceptors where non radiative recombination processes can dominate

## 2.7 Optical Transitions at Point Defects

In the previous section we have established that, where defects, whatever their nature, induce energy levels within the band gap, one of the most direct methods of probing the energy level system is by the detection of optical transitions between the levels and/or the bands The resulting spectra provide a wealth of information on the defect Recombination at point defects in silicon often gives rise to sharp intense zero phonon lines together with a multiphonon sideband structure The extent to which the electronic transitions of the defect couple to the vibrational modes of the lattice can be

established and in some cases coupling to the localised vibrational (or phonon) modes of the defect itself. The relative intensities of the zero phonon line and the side band structure is determined by the strength of the electron-lattice coupling. Spectra such as these are common in silicon. The origin of the observed transitions from an electronic and vibrational point of view will be addressed in the next section.

## 2.8 Electronic and Vibrational Elements of Emission Spectra

The elements of photoluminescence spectra resulting from electron-hole recombination in silicon may consist of three elements; (i) zero phonon transitions, (ii) vibrational modes of the crystal and (iii) impurity specific local modes. Each of these will be addressed in turn.

### 2.8.1 Zero Phonon Lines

When an optical transition occurs, there is a 'displacement recoil' associated with the electronic transition as the ions neighbouring the defect center relax to their equilibrium positions. This is expected to involve the excitation of several vibrational modes of the crystal resulting in a shift and broadening of the luminescence peak. However, since the states of excitation are quantised there is a finite probability that no mode of the crystal will be excited, thus, giving rise to a single 'zero phonon line' (ZPL) that is neither displaced nor broadened by energy transfer to the vibrational modes. Because of the narrow line shape associated with ZPL's small shifts and splittings of the line are easily detectable; this makes them particularly suitable for the application of perturbation techniques such as uniaxial stress or high magnetic fields which provides us with a means of deducing information on the defect and its associated crystal environment.

### 2.8.2 Vibrational Modes of the Crystal

A crystal can be described as a three dimensional array of coupled atoms. If we model the crystal as a series of atoms joined by springs, then all atoms are coupled to each other. The motion of each individual atom is a complicated one, with components in all directions. It can be decomposed into a sum of many harmonic parts of a large
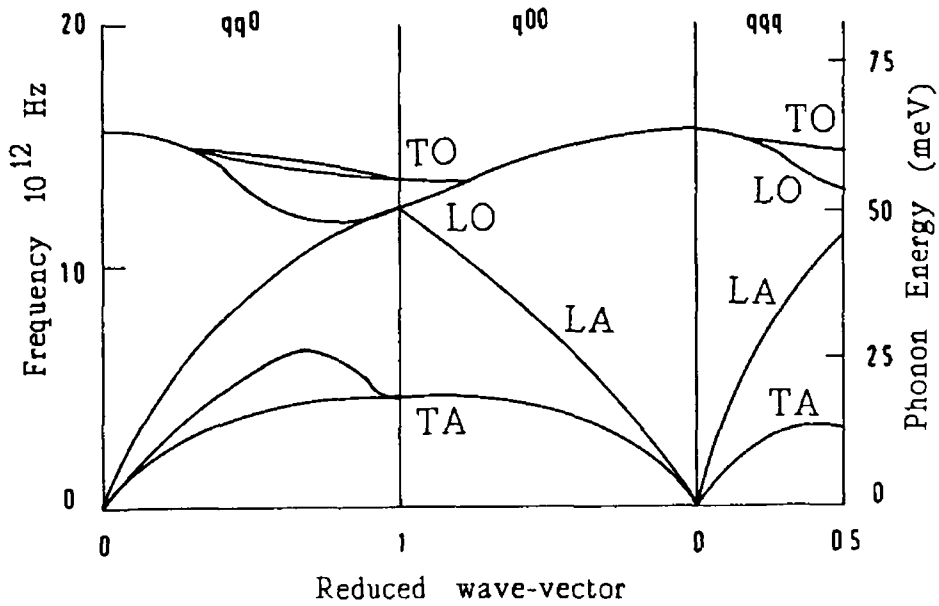
*Figure 2 11  Phonon dispersion curves for Si with q given in terms of 2π/a where a is the lattice constant for Si*

number of frequencies   Spring-like interatomic forces allow macroscopic elastic deformations of the semiconductor and coupled microscopic oscillations of each atom In a simple harmonic approximation, each mode of oscillation is equivalent to a harmonic oscillator which can be quantised as a phonon  By analogy with the photon, the phonon has energy E given by,

$$E = \hbar\omega$$
<div align="right">2 11</div>

and by the De Broglie's hypothesis can be considered to have particle like properties, with momentum given by,

$$p = \hbar k$$
<div align="right">2 12</div>

Therefore the lattice vibration can be thought of as a stream of phonons carrying the energy and momentum of the wave

The motion of each individual atom can be determined by its own vibrational frequency and the sum of the many components associated with the surrounding atoms or ions  When an optical transition occurs several vibrational modes of the crystal may be excited  If we consider the phonon dispersion curves illustrated in figure 2 11

[15] for the major symmetry directions in the silicon lattice we note that the density of phonon states is highest at ~18 meV, at ~56 meV and at ~58 meV for the transverse acoustic (TA), longitudinal optic (LO) and transverse optic (TO), modes respectively

### 2.8.3 Impurity Specific Local Modes

In silicon many defects are formed by the presence of one or more impurity atoms within the crystal structure  These defect complexes may have associated with them one or more modes of vibration, or degrees of freedom, within the solid, which may give rise to spectral features in the sideband structure of the defect  The majority of local modes found in silicon are produced by the vibrating atom being an impurity atom of low mass e g  C and O, local modes of impurities such as these are characterised by phonon quanta greater than 65 meV, the lattice cutoff  The vibrations associated with heavier impurity atoms will have phonon quanta which lie in the continuum of the host lattice

Because local modes are sharp, a photoluminescence spectrum appears to contain sidebands of the ZPL with a similar set of sidebands repeated from the local mode line containing the optic and acoustic lattice modes  Local modes which appear in the one phonon sideband may also be replicated in the multiphonon sideband  Local modes are spatially localised on the optical centre and so are sensitive to the electronic orbitals occupied by the centre

Local modes predominantly arise from the vibrations of one of the constituent atoms of the defect, hence they are particularly susceptible to isotope substitution  In fact the chemical constituents of many defects are determined by monitoring the response of the local modes to isotope effects

## 2.9 Electron-lattice Coupling

Consider an isolated atom with a series of excited states, if an electron is excited from a lower to a higher state it will eventually undergo a transition to its original lower energy state, with the quantum of electro-magnetic radiation emitted corresponding exactly to the energy difference of the levels involved, spectroscopically, a sharp line results  Now, introducing the atom into a crystal lattice as a defect center, the energy

of the system not only depends on the electronic state of the centre but also on the crystal environment. Firstly, the neighbouring atoms in the crystal produce an electrostatic potential (called the crystal field) which usually changes the allowed energy levels. Secondly, the fact that the atoms in the solid vibrate about their equilibrium positions results in the impurity atom becoming a participant in the vibrational motion of the crystal. Hence, when an electronic transition occurs vibrational modes of the crystal may also be excited. The extent to which electronic transitions couple to the vibrational modes of the crystal yields much information on the defect and it's environment.

When a defect centre undergoes excitation different electronic states of the defect can be occupied. This process changes the molecular configuration or the chemical bonds at the centre. The equilibrium positions of the atoms comprising the defect are likely to be different in the two electronic states, and the vibrational frequencies may also differ.

In general electronic transitions contribute both a broad multiphonon component and a narrow ZPL to the optical spectrum, with the relative intensities determined by the strength of the electron-lattice coupling. In the case of strongly coupled defects, virtually all of the intensity is in the broad multiphonon band whereas transitions for which the coupling is weak are characterised by having practically all of the intensity in the ZPL. Figure 2 12 illustrates four optical spectra showing the effect of increasing electron-lattice coupling [16]

Coupling can be viewed in two equivalent ways (i) the change in electronic energy as a function of lattice distortion or (ii) the electrons (holes) can be seen as exerting forces capable of distorting the lattice. Both views are equivalent. In both instances, upon excitation, it can be seen that the lattice has been affected by the presence of the electron (hole), a transition will occur thus "relaxing" the lattice to its original, pre excitation, state.

By analysing the changes in potential that the defect undergoes as a function of excitation and subsequent de-excitation, the degree of electron-lattice coupling which occurs can be estimated. In the following, the case of an optical centre with just one vibrational co-ordinate and with non-degenerate electronic states which are well separated in energy from all other electronic states will be considered, in the limit of linear coupling. In the ground state, prior to excitation, the vibrational potential energy
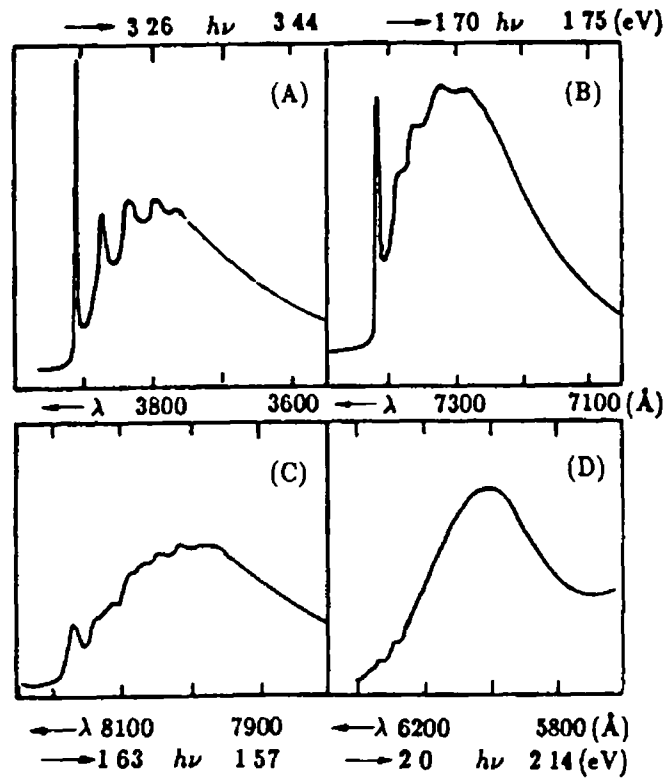
Figure 2 12  Optical absorption at 4 K of LiF, KCl, KBr and NaCl respectively showing
decreasing structure with increasing electron lattice coupling [9]

can be written as

$$V_g = \frac{1}{2}m\omega^2(Q-Q_g)^2$$

2.13

where m is the effective mass of the vibration with angular frequency $\omega$ and $Q_g$ is the
mean position of the vibrational displacement Q  Upon excitation, the centre has a
larger electronic energy E, and will have a new mean position at $Q_e$  The potential
energy of this new excited state is

$$V_e = E + \frac{1}{2}m\omega^2(Q-Q_g)^2 - E_r$$

2 14

where $E_r$ is energy through which the defect relaxes by virtue of its new equilibrium
position  We define a as the "linear electron-phonon coupling term" which can be
written in terms of the excited state equilibrium position as

$$a = -m\omega^2(Q_e - Q_g) \qquad\qquad 3.15$$

a changes the electronic energy of the system by an amount proportional to the deformation $(Q_e-Q_g)$  The relaxation energy $E_r$ and the change in the equilibrium position in terms of a are

$$E_r = \frac{a^2}{2m\omega^2} \qquad , \qquad |Q_e - Q_g| = \frac{a}{m\omega^2} \qquad\qquad 3.16$$

Equation 3 14 can therefore be rewritten as

$$V_e = E + \frac{1}{2}m\omega^2(Q - Q_e)^2 + a(Q - Q_g) \qquad\qquad 2.17$$

The ground and excited states of a system such as is described here can be schematically represented as in figure 2 13  $E_r$ can also be written in terms of the phonon quantum $\hbar\omega$ and the "Huang-Rhys factor" S,

$$S = \frac{E_r}{\hbar\omega} = \frac{a^2}{2m\hbar\omega^3} \qquad\qquad 2\ 18$$

S is a measure of the strength of the electron lattice coupling  Experimentally S can be found from the fraction of the transition probability which lies in the zero phonon line

$$S = \ln(I_n) - \ln(I_0) \qquad\qquad 2.19$$

where $I_n$ and $I_0$ are the luminescence intensities associated with the sideband and the ZPL respectively  In the analysis above we have only considered a state with single vibrational co-ordinate (Q) and with well separated electronic states  Usually an optical centre has a very large number of vibrational modes  To take account of this equations 2 13 and 2 17 can be generalised by

$$V_g = \frac{1}{2}\sum_i m_i\omega_i^2(Q - (Q_e - Q_g))_i^2 \qquad\qquad 2\ 20$$

$$V_e = E + \frac{1}{2}\sum_i m_i\omega_i^2(Q - Q_g)_i^2 + \sum_i a_i(Q - Q_g)_i \qquad\qquad 2.21$$
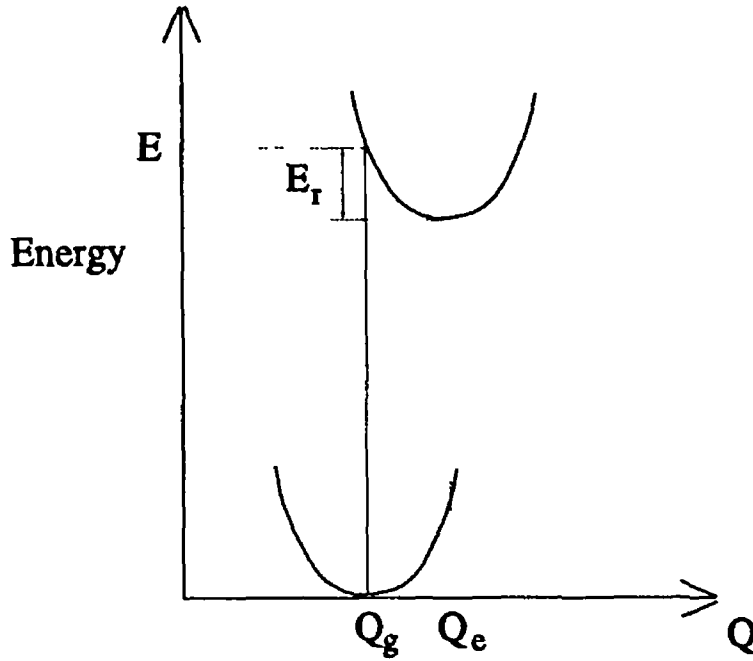
*Figure 2 13   Configuration coordinate diagram showing ground and excited states of a defect and typical excitation and recombination conditions*

$$= E + \frac{1}{2}\sum m_i \omega_i^2 ((Q_e)_i - (Q_g)_i)^2 - \sum S_i \hbar \omega_i \qquad 2\ 22$$

where $(Q_e)_i$ is the change in equilibrium position of the $i^{th}$ vibrational mode and $S_i$ is the Huang - Rhys factor for that mode

$$S_i = \frac{a_i^2}{m_i \hbar \omega_i^3} \qquad 2.23$$

As the vibrational modes are not mixed by the linear electron -phonon terms $a_i Q_i$, they are all independent of each other and the band shape has properties similar to those of the single mode case   At low temperatures, $(kT \ll \hbar\omega$, where $\omega$ is the frequency of the phonons which dominate the luminescence band), the side band involving n phonons of any frequency has a relative intensity [17]

$$I = \frac{S^n \exp(-S)}{n!} \quad , \quad S = \sum S_i \qquad 2.24$$

Because the phonons are independent of each other the probability of choosing n phonons is completely statistical   The $n^{th}$ phonon sideband $P_n$ can be constructed from

the (n - 1)$^{th}$ sideband $P_{n-1}$ and the one phonon sideband $P_1$ by taking all combinations of the two sidebands,

$$P_n(\omega) \sim \int P_{n-1}(\omega - x) P_1(x) dx \qquad\qquad 2\,25$$

where $\omega$ is the maximum frequency in the one-phonon side band

From the above analysis it is clear that the multiphonon sideband associated with any particular transition may be reconstructed, provided an accurate one-phonon sideband is determined

## 2.10 Conclusions

In this chapter we have examined the optical and electronic nature of semiconductor materials and established the existence of a forbidden energy gap into which energy levels may be induced due to the existence of defects in the crystal structure The introduction of such defects allows the optical and electronic properties of materials to be tailored to a specific application The evaluation of the properties of such defects is therefore of interest The use of optical techniques was established as a suitable means of probing such defects and the expected transitions were detailed In the final section the origins of the expected bandshape of the optical spectra were considered

In the next chapter we shall see that by monitoring the observed bandshape arising from a defect level and by changing the environment in which the crystal resides further information on the nature of the defect can be obtained

**References·**

[1]     S Perkowitz    Optical Characterisation of Semiconductors Academic Press (1993)

[2]     E C Lightowlers Growth and Characterisation of Semiconductors, edited by R A Stradling and P C Kilpstein, Adam Hilgar (1990)

[3]     G Kirczenow, Can J Phys **55** (1977) 1787

[4]     V A Karasyuk, D M Brake and M L W Thewalt, Phys Rev B 47 (1993) 9354

[5]     R E Dietz,D G Thomas, J.J Hopfield, Phys Rev Lett **8** (1962) 319

[6]     P.J Dean and D C Herbert, Bound Excitons in Semiconductors, Topics in Current Physics (Springer-Verlag 1979) 55

[7]     C H Henry, P.J Dean and J D Cuthbert, Phys Rev B, **166** (1967) 754

[8]     J J Hopfield, D G Thomas and R T Lynch, Phys Rev B 15 (1966) 312

[9]     E Cohen and M D Sturge, Phys Rev B, **15** (1977) 1039

[10]    M W L Thewalt, S P Watkins, U O Ziemelis, E C Lightowlers and M O Henry Solid State Commun **44** (1982) 573

[11]    D Labrie, T Timusk and M L W Thewalt, Phys Rev Lett **52** (1984) 81

[12]    J Weber, W Schmid, and R Sauer, Phys Rev B **21** (1980) 2401

[13]    K Thonke, A Hangleiter, J Wagner and R Sauer, J Phys C **18** (1985) L795

[14]    J Wagner, A Dornen and R Sauer, Phys Rev B **31** (1985) 5561

[15]    A D Zaetsis, Chem Phys **40** (1979) 345

[16]    D B Fitchen, R H Silsbee, T A Fulton and E L Wolfe, Phys Rev B 11 (1963) 275

[17]    G Davies, Phys Reports **176** (1989) 83

# Chapter 3

## Perturbation Techniques - Temperature, Uniaxial Stress and Zeeman Spectroscopy

## 3.1 Introduction

In chapter two the presence of defects in the crystal were seen to give rise to states within the forbidden energy gap, the most fundamental properties of such defects that can be determined are the positions of the energy levels and the wavefunctions of the states introduced by that defect   The most convenient method of monitoring transitions among levels is to record the bandshape of the spectrum in either absorption or emission, we saw in Chapter 2 how the analysis of such spectra can yield much information on the nature of the defect

If the defect levels and/or the band continua readily respond to externally applied perturbations a wealth of information about the defect and the crystal environment in which it resides may be obtained   Some of the external parameters that can be readily controlled are temperature, pressure and electrical and magnetic fields

In the following sections the response of the bandshape to temperature, uniaxial stress and magnetic fields as measured using photoluminescence spectroscopy will be considered with a view to analysing the data obtained in this work

## 3.2 Temperature Effects

Consider a silicon crystal in the limit of low temperature, i e at 0 K, the thermal energy, kT, of the system is zero and so transitions cannot occur among energy levels and all defect induced energy level structures are in the ground state   At a finite temperature and under illumination, however, the localised levels may become populated, the relative populations generally obeying Boltzman statistics   Defect induced excited states may be populated either by exciton capture or by internal transitions from the ground state to the excited states   Transitions may occur between

these levels or between localised levels and the band edges  The population of the levels will be determined by the temperature of the crystal and so transitions which occur and are detected as luminescence signals are temperature dependent  Changes in sample temperature will therefore affect the luminescence intensity of a PL system, the manner in which these changes occur yields detailed information on the binding mechanisms of the defect and its associated energy level system

The number of emitting levels will ultimately depend on the number of excitons available for capture by that defect and on the capture cross section of the defect for excitons (no distinction is made here between exciton capture and free carrier capture which may also lead to the production of an excited state of a defect)  A large number of competitive capture paths exist for the excitons  As the temperature increases excitons bound to shallow defects will become thermally dissociated and are available for capture by deeper defects  It is clear then that the position of the energy level with respect to the band edges and to other defect levels will affect the population of the level of interest

Data for a wide range of defects in silicon [1] show that luminescence output from many optical centres has two temperature regimes, at lower temperatures the luminescence intensity increases, while at higher temperatures a decrease in luminescence intensity is frequently seen
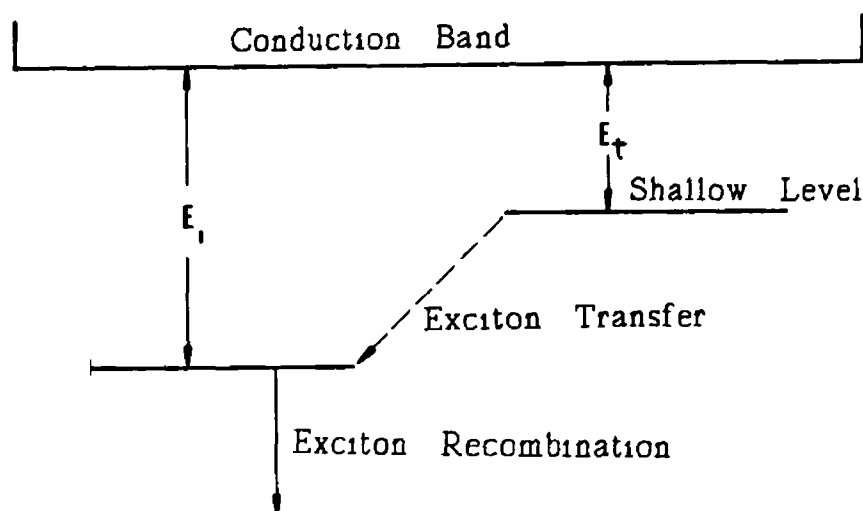


Figure 3 1  Schematic representation of the effect of shallow traps transferring energy into a deeper luminescence level

Consider first the low temperature behaviour of the luminescence intensity associated with a particular defect. The growth in intensity at low temperatures is sample dependent due to other traps competing for the excitons. As the temperature increases the fraction of shallow traps competing for the excitons decreases. The net result of this process is for the intensity of the luminescence associated with the defect to increase as temperature increases. Consider the situation in figure 3 1, all levels shallower than the one of interest are represented by a single level. With increasing temperature the shallow levels can no longer capture excitons due to rapid thermal ionisation. The fraction competing is simply that fraction left in the shallow level which Davies [1] describes by the equation

$$ f = \frac{1}{\left(1 + GT^{\frac{3}{2}}\exp\left(-\frac{\Delta E_t}{kT}\right)\right)} \qquad\qquad 3\ 1 $$

where G is the density of conduction band states relative to the trap states. Thus, at T = 0 K, f = 1, i e all traps are competing for exciton capture. As the temperature is increased a maximum intensity will be reached when the temperature is sufficiently high to prohibit exciton capture at the shallower level.

As the temperature is raised further, a drop in intensity is seen which can be attributed to the quenching of the luminescence as the excitons bound to the defect of interest begin themselves to thermally dissociate before electron hole recombination can take place. If the number of luminescence centres with excitons bound to them is defined by $N^x_i$, the number of centres with the exciton thermally ionised as $N^0_i$ and the total number of luminescence centres by $N_i$ then the luminescence intensity I as a function of temperature is defined by,

$$ I(T) = N^x_i(T)f^x \qquad\qquad 3.2 $$

where $f^x$ is the probability of radiative recombination. From equation 3 1

$$ I(T) = \frac{N_i f^x}{\left(1 + GT^{\frac{3}{2}}\exp\left(-\frac{E_t}{kT}\right)\right)} \qquad\qquad 3.3 $$

$I_i(0)$ is the luminescence intensity at T = 0, therefore the decay of the luminescence

$$I(T) = \frac{I_i(0)}{\left(1 + GT^{\frac{3}{2}}\exp\left(-\frac{E_i}{kT}\right)\right)}$$

3.4

system as a function of temperature may be modelled using the expression,

$$\frac{I(T)}{I_i(0)} = \frac{1}{\left(1 + GT^{\frac{3}{2}}\exp\left(-\frac{E_i}{kT}\right)\right)}$$

3.5

By constructing an Arrhenious plot of the decay in luminescence intensity, the ionisation energy of the excition from the defect can be calculated

Therefore by analysing the luminescence intensity as a function of temperature information on the binding of charge carriers to the defect can be obtained

## 3.3 Uniaxial Stress

The narrow no-phonon luminescence line associated with the recombination of excitons at an optical centre make it possible to measure directly small shifts and splitting of the no-phonon line The application of a force along known crystal directions has the effect of splitting no-phonon lines in a characteristic manner determined by the symmetry of the associated defect Uniaxial stress spectroscopy is a well established and powerful technique used extensively to determine the symmetry of defects and of their electronic states The technique involves the application of an axial perturbation such as compression, along a known crystal direction The effect of a uniaxial stress on the electronic states of a crystal is to remove fully or partially the degeneracy of the energy levels The measurement gives the response of electronic states to movements of the atoms near the optical centre Hence, the associated energy levels are shifted and/or split into a number of components The measurable parameters are the number of stress split components together with the intensity, polarisation and energy shift of each component which yields the symmetry of the electronic states of the defect [2]

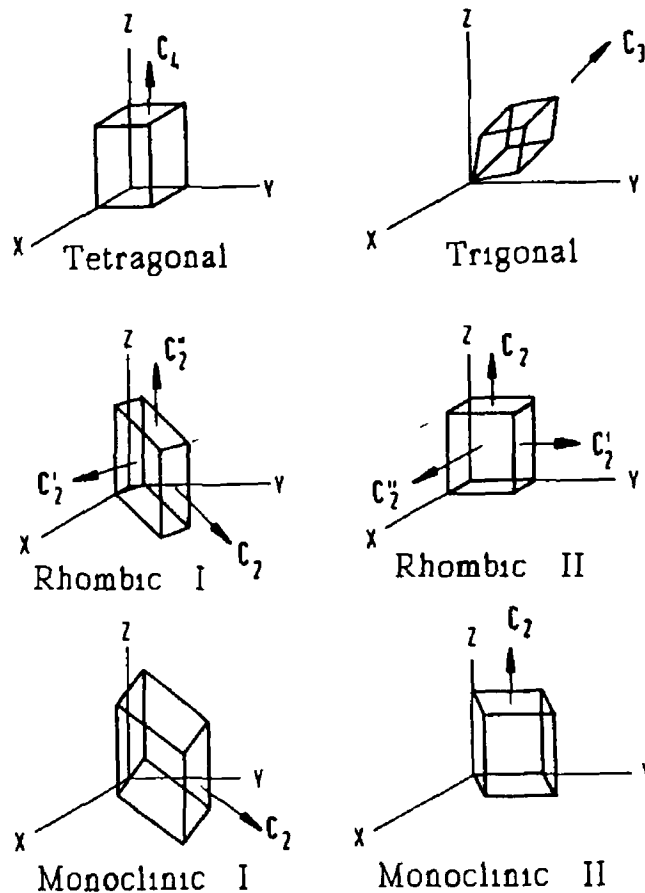A fundamental characteristic of any axial defect is that it possesses a certain

*Figure 3 2 Schematic representation of six of the eight possible symmetry systems for defects in cubic crystals*

preferred direction or axis of symmetry within the host lattice  This axis cannot have random directions but is oriented along a symmetry axis of equal or lower order to the symmetry of the crystal  The silicon crystal has cubic symmetry  All defects in silicon will thus adopt a cubic symmetry or exhibit other symmetry systems which are a sub group of this  The possible sub groups of the cubic group can be classified into eight symmetry systems  Figure 3 2 illustrates six of the eight possible symmetry systems for defects in cubic crystals, the other two are cubic, whose symmetry axes must coincide with the lattice axes, and triclinic, for which there are no restrictions on defect orientation  In the case of the silicon lattice, three equivalent four fold axes are available along the <100> directions - defects which adopt this orientation are tetragonal, monoclinic II and rhombic II, four equivalent three fold axes along the <111> directions are available which gives rise to trigonal defects, and six equivalent two fold axes along

the <110> directions are available - both monoclinic I and rhombic I oriented defects fall into this category

Orientational degeneracy and/or electronic degeneracy may be lifted with the application of uniaxial stress, the differences between the two are easily understood
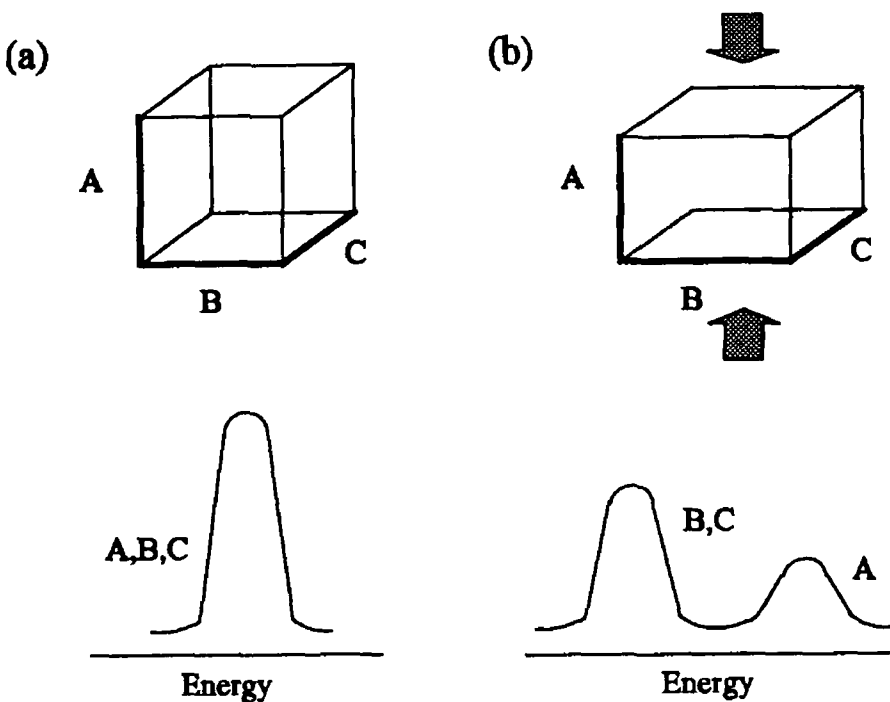


Figure 3 3  Schematic representation of (a) energetically equivalent defects A, B and C, which become orientationally nondegenerate under uniaxial stress (b)

Consider the situation in figure 3 3, a defect present in a simple cubic crystal structure may have a number of orientations which in an unstrained crystal are energetically equivalent, three such defects are represented in figure 3 3(a), labelled A, B and C  The electronic potential of each centre is equivalent and gives rise to a single transition in emission or absorption  When a uniaxial stress is applied all three defects will be affected  In figure 3 3(b) the effect of a stress applied parallel to the <100> axis is illustrated, the defects labelled B and C are affected equally by the applied stress and their potentials coincide  However, in the case of defect A the stress experienced will

differ and so the potential associated with defect A will be different from that of B and C, thus leading to two stress split components

For the case of electronic degeneracy, consider a single defect with electrons in different degenerate orbitals $p_x$, $p_y$ and $p_z$  In the absence of stress all such defects are equivalent  If the crystal is stressed in a direction parallel to $p_z$ the potential may be different in that orbital to those in the $p_x$ and $p_y$ orbitals leading to a splitting of spectral lines involving these p states  The distinction between electronic and orientational degeneracy is very clear and is important for an accurate analysis of uniaxial stress data

In order to determine the hidden anisotropy of a defect centre, it is necessary to perturb the cubic crystal in such a manner as to remove the degeneracy associated with the axial nature of the defect  This is achieved by the application of a force to samples oriented in each of the three major crystallographic directions

It is clear that for each symmetry type, a fixed number of stress split components can be expected when the crystal is stressed along each one of its principal axes  From an analysis of the stress split pattern a defect may be assigned to one of the possible symmetry systems  Table 3 1 lists all of the transitions possible for defects in silicon, together with the number of stress split components expected for uniaxial stress along the three major crystallographic axis  They have been grouped together according to the degeneracy that can be lifted, the first group are all singlet to singlet transitions where only orientational degeneracy is removed, in the third group only electronic degeneracy is lifted and in the second group both electronic and orientational degeneracy are lifted  A schematic representation of the stress split component intensities is given in figure 3 4  In this figure, the vertical lines above the horizontal lines represent polarised spectral lines parallel to the stress direction, and those below perpendicular to it  For [110] stress, there are two inequivalent perpendicular polarisations, denoted by solid and dashed lines, the asterisk indicates that the intensity ratio is not unique

The derivation of the number of stress split components, the intensity and polarisation, and the shift rate parameters for each component involves the application of group theory and first-order perturbation theory  Detailed treatments of the derivations have been given by Kaplyanskii [3,4], Hughes and Runciman [5] and Mohammed et al [6]  In the present work the rhombic I symmetry system is of particular relevance and so the results for this system will be derived from first principals

| Centre and Allowed Transitions | Expected Number of Stress Split Components | | | Associated Degeneracies |
| --- | --- | --- | --- | --- |
| | <100> | <111> | <110> | |
| 1 Tetragonal (A→A) | 2 | 1 | 2* | |
| 2 Trigonal (A→A) | 1 | 2 | 2 | |
| 3 Rhombic I (A→A) | 2 | 2 | 3 | |
| 4 Rhombic II (A→A) | 3 | 1 | 3 | Orientational |
| 5 Monoclinic I (A→A) | 2 | 3 | 4 | |
| 6 Monoclinic II (A→A) | 3 | 2 | 4 | |
| 7 Triclinic (A→A) | 3 | 4 | 6 | |
| 8 Tetragonal (A→E) | 3 | 2 | 4* | |
| 9 Tetragonal (E→E) | 3 | 2 | 4* | Orientational |
| 10 Trigonal (A→E) | 2 | 3 | 4* | and |
| 11 Trigonal (E→E) | 4 | 5 | 8 | Electronic |
| 12 Tetrahedral ($T_1 \rightarrow T_2$) | 3 | 4 | 6 | |
| 13 Tetrahedral ($A \rightarrow T_{1,2}$) | 2 | 2 | 3 | |
| 14 Tetrahedral ($E \rightarrow T_{1,2}$) | 3 | 2 | 5 | Electronic |
| 15 Tetrahedral ($T_1 \rightarrow T_1$) ($T_2 \rightarrow T_2$) | 3 | 3 | 6 | |
| 16 Tetrahedral ($\Gamma_8 \rightarrow \Gamma_8$) | 4 | 4 | 4 | |
| 17 Tetrahedral ($\Gamma_{67} \rightarrow \Gamma_8$) | 2 | 2 | 2 | |

*Table 3 1 Maximum number of components in the splitting patterns of all transitions possible at centres within the Si lattice * denotes that the number of components observable for <110> stress is dependent on viewing direction*

[100]  [111]  [110]

| Triclinic | A → A | (3) | (4) | (6) |

| Monoclinic I | A ↔ A, B ↔ B |
| | A ↔ B |

| Monoclinic II | A ↔ A, B ↔ B |
| | A ↔ B |

| Rhombic I | A₁ ↔ B₁ |
| | A₁ ↔ B₂,₃ |

| Rhombic II | A₁ ↔ B₁ |

| Trigonal | A ↔ A |
| | A ↔ E |
| | E ↔ E | (4) | (5) | (8) |

| Tetragonal | A ↔ A, B ↔ B |
| | A ↔ E |
| | E ↔ E |

| Cubic | A₁ ↔ T₁ |
| | E ↔ T₁,₂ |
| | T₁ ↔ T₂ |
| | T₁ ↔ T₁, T₂ ↔ T₂ |
| | Γ₆ ↔ Γ₈ |
| | Γ₆ ↔ Γ₆ |

*Figure 3 4  Schematic splittings of n-phonon lines under uniaxial stress for transitions at centres belonging to the eight possible symmetry systems for cubic crystals*

### 3.3.1 A note on Group Theory.

Each of the symmetry classes referred to above have associated with them a series of point groups each of which can be identified by a unique character table A character table describes, in a concise manner, the symmetry operations under which a particular point group remains invariant The character table for a $C_{2v}$ point group is shown in table 3 2 The symmetry operation associated with each class is at the top of each column preceded by the number of elements in that class Each row, or irreducible representation, is labelled according to the Muliken notation scheme Thus A or B

| $C_{2v}$ | E | $C_2$ | $\sigma_v$ | $\sigma'_v$ | Basis Functions |
|---|---|---|---|---|---|
| $A_1$ | 1 | 1 | 1 | 1 | $x^2, y^2, z^2$ |
| $A_2$ | 1 | 1 | -1 | -1 | xy |
| $B_1$ | 1 | -1 | 1 | -1 | xz |
| $B_2$ | 1 | -1 | -1 | 1 | yz |

*Table 3 2   Character table associated with the point group $C_{2v}$*

indicates a state with a degeneracy of one, i e only possesses orientational degeneracy (while E and T denaote states with deeneracy of 2 and 3 respectively) The final column on the right hand side of the character table lists some representative basis functions of the irreducible representation, the value of these basis function will become apparent as we consider the potential associated with the stress The list of the 32 crystallographic point groups which are subgroups of the cubic system are available in reference [7]

Let us assume we have an axial defect which gives rise to a single transition between two energy levels $E_a$ and $E_b$ in an unstressed crystal The application of a uniaxial stress may cause the energy levels to adopt new values as shown in figure 3 5

Mathematically, this may be represented by the introduction of a perturbation operator $\hat{V}$ into the Hamiltonian of the crystal,

$$H = H_0 + \hat{V} \qquad\qquad 3.6$$
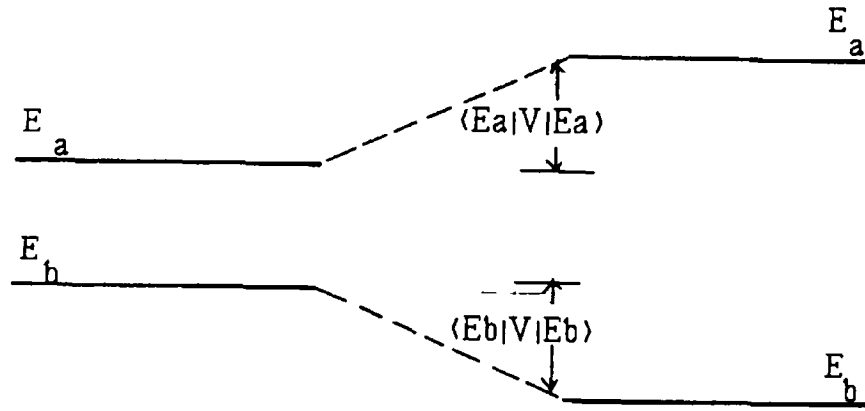
where

*Figure 3 5* *Schematic representation of the effect of uniaxial stress on transitions between electronic states*

$$\hat{V} = \Sigma_{yk}\ a_k s_{ij}$$ 

3.7

where $s_{ij}$ corresponds to a force applied to the $i^{th}$ face in the $j^{th}$ direction and $a_k$ are electronic operators of the stress operator $\hat{V}$, which transform as $<E|a_k|E>$ in the state $|E>$ as illustrated in figure 3 5   Any stress s, can be uniquely identified in the cubic crystal by six "stress tensor" components $s_{XX}$, $s_{YY}$, $s_{ZZ}$, $s_{XY}$, $s_{YZ}$ and $s_{ZX}$, all of which are symmetric ($s_{ij} = s_{ji}$), where x=[100], y=[010] and z=[001] are the cubic axes of the crystal   The tensor components can therefore be calculated from,

$$s_{ij} = |\vec{P}|\cos(i,\vec{P})\cos(j,\vec{P})$$ 

3.8

where (i,P) is the angle between the stress direction P and the $i^{th}$ axis and $|P|$ is the magnitude of the applied stress   Thus equation 3 7 becomes,

$$\hat{V} = \hat{a}_1 s_{XX} + \hat{a}_2 s_{YY} + \hat{a}_3 s_{ZZ} + \hat{a}_4 s_{XY} + \hat{a}_5 s_{YZ} + \hat{a}_6 s_{ZX}$$ 

3 9

This is the general form of the stress potential   Referring again to figure 3 6, in the unstressed situation the transition energy $E_T$ is

$$E_T = E_a - E_b$$ 

3.10

With the application of stress the energy levels may change giving a new transition energy $E'_T$,

$$E_T' = E_a - E_b + <\psi_a|\hat{V}|\psi_a> + <\psi_b|\hat{V}|\psi_b>$$ 
<div align="right">3.11</div>

$$E_T' = E_a - E_b + \delta$$ 
<div align="right">3.12</div>

where $\delta$ is termed the shift rate of the transition Referring to table 3 2 we see, from the basis function, that only $x^2$, $y^2$ and $z^2$ transform as the $A_1$ representation of $C_{2v}$, since xy, yz and zx do not transform as the $A_1$ representation of $C_{2v}$ the variables $\hat{a}_4$, $\hat{a}_5$ and $\hat{V}_6$ are zero in $<\psi_a|\hat{V}|\psi_a>$ and $<\psi_b|\hat{a}|\psi_b>$ Therefore equation 3 9 becomes,

$$\hat{V} = \hat{a}_1 s_{XX} + \hat{a}_2 s_{YY} + \hat{a}_3 s_{ZZ}$$ 
<div align="right">3 13</div>

The shift rate delta then becomes,

$$\delta = s_{XX}[<\psi_a|\hat{a}_1|\psi_a> + <\psi_b|\hat{a}_1|\psi_b>]$$
$$+ s_{YY}[<\psi_a|\hat{a}_2|\psi_a> + <\psi_b|\hat{a}_2|\psi_b>]$$
$$+ s_{ZZ}[<\psi_a|\hat{a}_3|\psi_a> + <\psi_b|\hat{a}_3|\psi_b>]$$ 
<div align="right">3.14</div>

Each $<\psi|\hat{a}|\psi>$ term is the solution of a definite integral which is a real number, therefore each $[<\psi|\hat{a}|\psi> + <\psi|\hat{a}|\psi>]$ term can be substituted by a corresponding real constant $a_x$, known as the stress parameter,

$$\delta = a_1 s_{XX} + a_2 s_{YY} + a_3 s_{ZZ}$$ 
<div align="right">3.15</div>

For a rhombic I defect in a cubic crystal, there are six distinguishable orientations available for which the defect coordinates are listed in table 3 3 (Stresses which differ only by inversion can be treated as one) Equation 3 15 is the general form of the stress potential for a $C_{2v}$ centre, where X,Y and Z are the local axes of the defect for any chosen orientation of the optical centre It is necessary to express this equation in terms of the stress tensor components determined by the experimental arrangement, i e to transform from defect co-ordinates (X,Y and Z) to crystal co-ordinates (x, y and z) Consider defect number 1 of table 3 3,

$$X = 110 \qquad Y = \bar{1}10 \qquad Z = 001$$ 
<div align="right">3.16</div>

the crystal co-ordinates are

| Defect | X | Y | Z |
|---|---|---|---|
| 1 | 110 | $\bar{1}10$ | 001 |
| 2 | $\bar{1}10$ | 110 | $00\bar{1}$ |
| 3 | 011 | $0\bar{1}1$ | 100 |
| 4 | $01\bar{1}$ | $0\bar{1}\bar{1}$ | $\bar{1}00$ |
| 5 | 101 | $10\bar{1}$ | 010 |
| 6 | $\bar{1}01$ | $\bar{1}0\bar{1}$ | $0\bar{1}0$ |

*Table 3 3* *Defect co-ordinates for the six distinguishable defect axes at a rhombic I centre*

$$x = 100 \qquad y = 010 \qquad z = 001 \qquad\qquad 3.17$$

The defect co-ordinates in terms of crystal co-ordinates are

$$X = \frac{(x+y)}{\sqrt{2}} \qquad Y = \frac{(-x+y)}{\sqrt{2}} \qquad Z = z \qquad 3.18$$

The products used in the stress tensors are

$$XX = \frac{(xx+2xy+yy)}{2} \qquad YY = \frac{(xx-2xy+yy)}{2} \qquad ZZ = zz \qquad 3.19$$

Equation 3 13 can now be rewritten as

$$\hat{V} = a_1 \frac{(s_{xx}+2s_{xy}+s_{yy})}{2} + a_2 \frac{(s_{xx}-2s_{xy}+s_{yy})}{2} + a_3 s_{zz} \qquad 3.20$$

Simplifying this we get

$$\hat{V} = \frac{(a_1+a_2)(s_{xx}+s_{yy})}{2} + (a_1-a_2)s_{xy} + a_3 s_{zz} \qquad 3.21$$

Defining new variables by the equations

$$A_1 = a_3 \qquad A_2 = \frac{(a_1+a_2)}{2} \qquad A_3 = \frac{(a_1-a_2)}{2} \qquad 3.22$$

equation 3 20 becomes

$$V = A_1 s_{zz} + A_2 (s_{xx} + s_{yy}) + 2A_3 s_{xy}$$

This procedure can be repeated for each of the other five centres listed in table 3 3, the same potential will be derived for each

In order to determine the stress parameters it is necessary to consider the numbers of stress split components arising from the application of a stress along each of the three principal directions A rhombic I defect has a principal axis of order 2 along a <100> type axis, which, by convention is usually deemed to be the Z axis of the
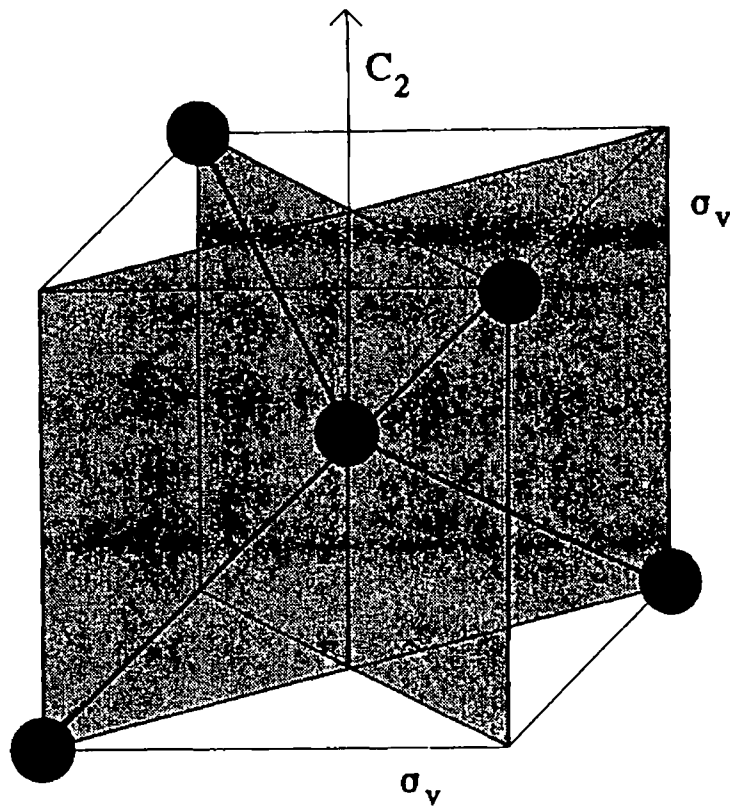


Figure 3 6 Schematic representation of symmetry elements of a rhombic I defect, consisting of a principal axis of order 2 along a <100> type axis and two reflection planes in <110> type planes

defect, and two reflection planes in <110> type planes as illustrated in figure 3 6 The expected number of stress split components can be found by calculating the values of $s_{ij}$, using equation 3 8, for each of the six rhombic I defects under a uniaxial stress along each of the three principal axis directions Table 3 4 lists all of the $s_{ij}$ values for

rhombic I symmetry, in terms of the local defect co-ordinates Equation 3 13 contains only the symmetric stress tensors $s_{XX}$, $s_{YY}$ and $s_{ZZ}$, the other tensor components of table 3 4 can therefore be ignored Consulting the relevent columns of table 3 4 we find that under <001> stress the six defects fall into two distinct families, those aligned parallel to the stress (defects 1 and 2) and those aligned perpendicular to the stress (defects 3,4,5and 6) Two stress split components are therefore expected when a stress is applied along the <001> axis of the crystal The shift rate equations can be obtained

| Centre | $s_{XX}$ | $s_{YY}$ | $s_{ZZ}$ | $s_{XY}$ | $s_{XZ}$ | $s_{YZ}$ |
|---|---|---|---|---|---|---|
| **Stress I <001>** | | | | | | |
| 1 | 0 | 0 | 1 | 0 | 0 | 0 |
| 2 | 0 | 0 | 1 | 0 | 0 | 0 |
| 3 | 1/2 | 1/2 | 0 | 1/2 | 0 | 0 |
| 4 | 1/2 | 1/2 | 0 | 1/2 | 0 | 0 |
| 5 | 1/2 | 1/2 | 0 | -1/2 | 0 | 0 |
| 6 | 1/2 | 1/2 | 0 | -1/2 | 0 | 0 |
| **Stress I <111>** | | | | | | |
| 1 | 2/3 | 0 | 1/3 | 0 | $(\sqrt{2})/3$ | 0 |
| 2 | 0 | 2/3 | 1/3 | 0 | 0 | $-(\sqrt{2})/3$ |
| 3 | 2/3 | 0 | 1/3 | 0 | $(\sqrt{2})/3$ | 0 |
| 4 | 0 | 2/3 | 1/3 | 0 | 0 | $(\sqrt{2})/3$ |
| 5 | 2/3 | 0 | 1/3 | 0 | $(\sqrt{2})/3$ | 0 |
| 6 | 0 | 2/3 | 1/3 | 0 | 0 | $(\sqrt{2})/3$ |
| **Stress I <110>** | | | | | | |
| 1 | 1 | 0 | 0 | 0 | 0 | 0 |
| 2 | 0 | 1 | 0 | 0 | 0 | 0 |
| 3 | 1/4 | 1/4 | 1/2 | -1/4 | $1/2\sqrt{2}$ | $-1/2\sqrt{2}$ |
| 4 | 1/4 | 1/4 | 1/2 | -1/4 | $-1/2\sqrt{2}$ | $1/2\sqrt{2}$ |
| 5 | 1/4 | 1/4 | 1/2 | 1/4 | $1/2\sqrt{2}$ | $1/2\sqrt{2}$ |
| 6 | 1/4 | 1/4 | 1/2 | 1/4 | $1/2\sqrt{2}$ | $1/2\sqrt{2}$ |

*Table 3 4   Calculated $s_{ij}$ values for the six rhombic I defects, in terms of the local crystal coordinates   The defect labels 1-6 are consistent with table 3 3.*

by considering a representative defect from each family, in this case defect 1, (parallel to stress) and defect 3 (perpendicular to stress) are suitable The expected shift rates are

$$\delta_1 = A_1 \qquad\qquad 3.24$$

$$\delta_2 = A_2 \qquad\qquad 3.25$$

When stress is applied along a <111> type axis we again get two families of defects, defects 1,3 and 5 forming one family and defects 2,4 and 6 forming the second The shift rate equations are

$$\delta_3 = \frac{1}{3}(A_1 + 2A_2 + 2A_3) \qquad\qquad 3.26$$

$$\delta_4 = \frac{1}{3}(A_1 + 2A_2 - 2A_3) \qquad\qquad 3.27$$

Under <110> type stress three families of defect are apparent, defect 1 , defect 2 and defects 3,4,5 and 6, giving three equations

$$\delta_5 = A_2 + A_3 \qquad\qquad 3\ 28$$

$$\delta_6 = \frac{1}{2}(A_1 + A_2) \qquad\qquad 3.29$$

$$\delta_7 = A_2 - A_3 \qquad\qquad 3\ 30$$

Each of these equations represents the shift rates of the various stress split components of a zero-phonon line associated with the defect By constructing a stress vs energy shift graph the shift rates can easily be determined It is trivial then to calculate the stress parameters $A_1$, $A_2$ and $A_3$ from the calculated slopes and equations 3 24 - 3 30

It is possible to predict the relative polarised intensities of each stress split component of the zero-phonon line It is first necessary to guess along which axis the electric dipole vector of the optical transition lies, however in most cases it tends to lie along the defect axis of highest symmetry, i e along the defect Z-axis Taking the square of the projection of the unitary vector lying along the direction of the electric dipole onto the unitary vector lying in the direction parallel to the stress will yield the
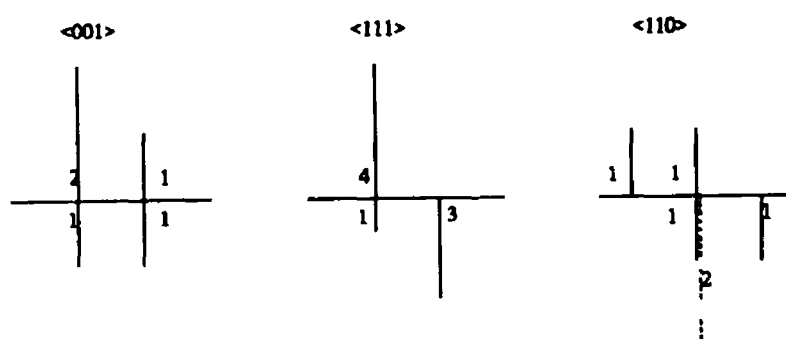
<001>     <111>     <110>

2 1

1 1

4

1 3

1 1

1

1 2

2

*Figure 3 7    Schematic representation of the polarised intensities of the stress split components for rhombic I defects*

expected intensity for π polarised luminescence    (π polarised luminescence is luminescence emitted with electric vector parallel to the stress direction, wheras σ polarised luminesence has electric vector perpendicular to the stress direction)    A projection lying in the direction perpendicular to the stress will yield the σ polarised intensity    This information is often graphically represented as in figure 3 7, where the relative polarised intensities are illustrated for rhombic I defects for stress applied in each of the three principal directions    If the predicted intensities do not match with the experimental results then the choice of electric dipole vector is incorrect, for example the electric dipole could be aligned perpendicular to the Z-axis of the defect    This situation may be analysed in a similar fashion

The analysis presented above has determined specific numbers of stress split components, the shift rates, the stress parameters and the expected intensities for a rhombic I defect    The symmetry of a particular defect whose stress split pattern is consistent with the above analysis can be assigned to the rhombic I symmetry group

## 3 3.2 Mixing of States

In the above analysis the effect of uniaxial stress on a single transition from an excited state to a ground state has been addressed    In reality this is a restricted view as many defects give rise to a series of excited states, often very closely spaced    These states can interact with each other under uniaxial stress, a phenomenon usually referred to as mixing of states

Mixing of states occurs between excited states of nearly equal energy and is essentially an interaction between the levels resulting in a non-linear shift rate    This
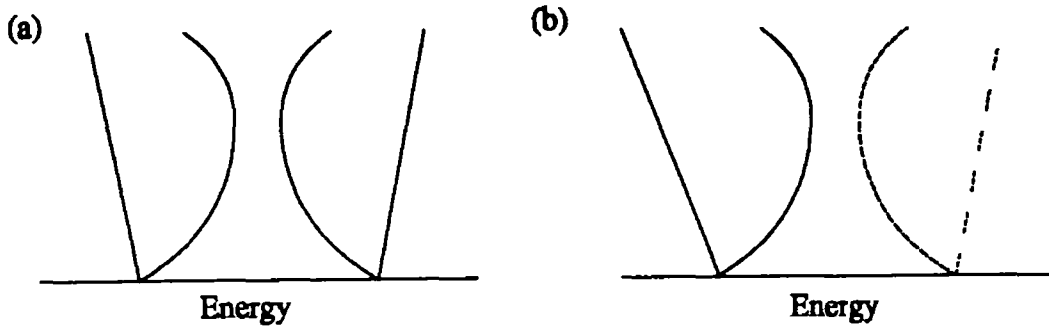
*Figure 3 8   Schematic representation of stress split components (a) two interacting states, and (b) two states interacting, one of which is not observed.*

effect manifests itself in the stress vs energy graphs as non-linear, curved shift rates instead of the expected linear relationship, as illustrated in figure 3 8(a)   Due to selection rules, the excited state structure of a defect may include levels from which transitions are forbidden   Consider an excited state structure containing excited states $E_a$, from which transitions to the ground state are allowed, and $E_b$, from which transitions to the ground state are forbidden   In the unstressed situation there is no interaction between the two levels and $<\Psi_a|\hat{V}|\Psi_b> = 0$   If, under the action of a uniaxial stress the levels interact, we find that $<\Psi_a|\hat{V}|\Psi_b> \neq 0$   Consequently the stress provides a means for a transition from the $E_b$ state to the ground state to occur via mixing with the $E_a$ state   Closely interacting states may cause a non linear shift rate as illustrated in figure 3 8(b)   As the stress is increased, the stress split components approach each other and, and as the states begin to interact, a fraction of the intensity is transferred from the allowed to the forbidden transition via the interaction, thereby producing spectral features associated with the previously forbidden transition

Consider a situation with two closely spaced excited states with wavefunctions $\Psi_a$ and $\Psi_b$   The interaction matrix will take the form,

$$\begin{bmatrix} <\Psi_a|\hat{V}|\Psi_a> & <\Psi_a|\hat{V}|\Psi_b> \\ <\Psi_b|\hat{V}|\Psi_a> & <\Psi_b|\hat{V}|\Psi_b> \end{bmatrix}$$

3.31

The off diagonal elements represent the strength of the interaction, the form of these elements is usually similar to that of the interacting states   The matrix elements therefore become,

$$Element[1\ 1] \qquad A_1 s_{zz} + A_2(s_{xx} + s_{yy}) + 2A_3 s_{xy} \qquad\qquad 3.32$$

$$Element[2\ 2] \qquad A_1' s_{zz} + A_2'(s_{xx} + s_{yy}) + 2A_3' s_{xy} + E \qquad\qquad 3\ 33$$

$$Elements[1\ 2],[2\ 1] \qquad A_1'' s_{zz} + A_2''(s_{xx} + s_{yy}) + 2A_3'' s_{xy} \qquad\qquad 3.34$$

where E is the separation of the energy levels at zero stress By diagonalising this matrix in the usual manner a series of eigenvalues is found as a function of stress It is clear that the number of variables has increased three fold due to the presence of two interacting levels, thus creating a non trivial problem in obtaining a unique set of solutions to fit any particular data set In this case it is necessary to simultaneously optimise all of the parameters to obtain a solution set with minimum deviation from the actual data

Conventional approaches to this problem rely upon the manipulation of the secular matrix for one individual direction until a reasonable fit is found Having established a best fit in one direction these parameters are then used in the secular matrix for a second direction and the parameter estimates further manipulated, this iterative process is continued until a reasonable overall fit is obtained It is clear that this method is inefficient, it's main drawback being the focusing on one direction at any one time A more systematic approach is to obtain simultaneously parameter estimates for all parameters in all stress directions A P C based optimisation tool designed specifically to identify transitions and assign them to a particular symmetry class was used The system obtains estimates for all of the parameters of the secular matrix simultaneously by applying a non linear least squares fit between the experimental data and the eigenvalues of the matrix [8]

## 3.4 Zeeman Analysis

The splitting of lines of the spectrum of atoms in a longitudinal or transverse magnetic field was first observed by Zeeman (1897) and is termed the Zeeman effect The Zeeman effect is traditionally related to single atoms but is also observed for defects in solids In a semiconductor the influence of the surrounding lattice must be

taken into consideration

We have established in the previous section that uniaxial stress measurements give the response of electronic states to movements of the atoms near an optical centre, which is useful for probing related properties such as vibronic coupling However, because stress perturbations derive from translations of atoms they produce no resolvable effects on the spin states of electrons or holes bound to the defect In contrast, however, a magnetic field will interact with an orbiting charged particle (electron or hole) and perturb the energy level formerly occupied by the particle The result of this is to induce a splitting related to the removal of the spin degeneracy of the levels involved in the transition

Since the discovery of isoelectronic defects, much work has centered on attempting to determine the process by which the excitons bind to them Zeeman spectroscopy has proved to be particularly helpful in determining the energy level structure of excitons bound at isoelectronic defects To understand its' significance we must first examine the effects of internal strain and $j$-$j$ coupling on the energy level structure of these defects

Consider an electron from the bottom of the conduction band, with $j = 1/2$, and a hole from the top of the valence band, with $j = 3/2$, which can couple to form excitonic states of total angular momentum $J = 1$ or $J = 2$, with the $J = 2$ level lying lower in energy If a tensile axial strain is present about the defect the $J$ values no longer remain good quantum numbers The $J = 2$ level splits into $m_J = \pm 2$, $\pm 1$ and $0$ sublevels, in order of increasing energy, while the $J = 1$ level splits into $m_J = \pm 1$ and $0$ The two-fold degeneracy of these $m_J$ levels is referred to as Kramers degeneracy and will be lifted in the presence of a magnetic field as depicted in figure 3 9 Transitions from these levels to the ground state will be governed by the selection rules associated with optical spectra Thus transitions from the $m_J = \pm 2$, and $0$ sublevels to the $m_J = 0$ crystal ground state are forbidden, while the $m_J = \pm 1$ sublevels are allowed All of the reported electron attractive isoelectronic defects in semiconductors have been found to exhibit either the pure quintet-triplet ($J = 2,1$) or a set of $|J,m_J\rangle$ levels as described here Examples include GaP N [9], Si Be [10], Si Tl [11] and several others in the review by Davies [1]

If the axial field is compressive then the lowest energy hole state $j = 3/2$ becomes $m_J = 1/2$ If the hole is the tightly bound particle it is much more sensitive to
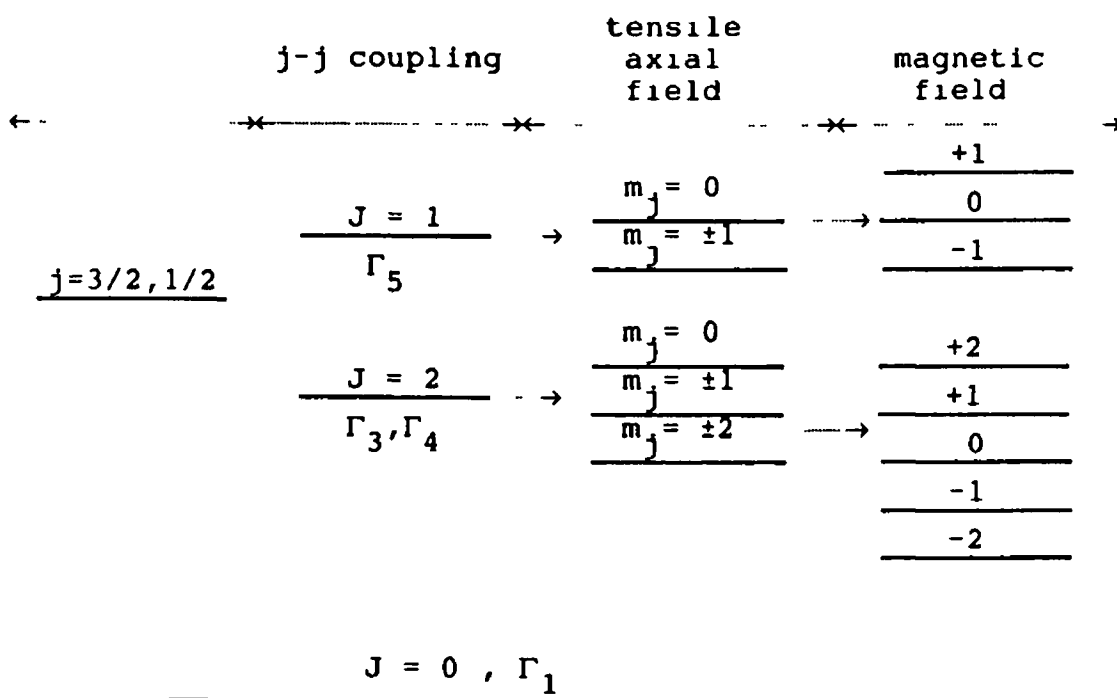
tensile
j-j coupling    axial         magnetic
field        field

j=3/2,1/2

$J = 1$

$\Gamma_5$

$m_j = 0$

$m_j = \pm 1$

+1

0

-1

$J = 2$

$\Gamma_3, \Gamma_4$

$m_j = 0$

$m_j = \pm 1$

$m_j = \pm 2$

+2

+1

0

-1

-2

$J = 0 \ , \ \Gamma_1$

*Figure 3 9  The zero phonon level structure of a quintuplet - triplet BE system.*

the local symmetry field of the defect  This is particularly evident for defects which display a symmetry of low order for example $C_{2v}$  The result of this is to restrict the degeneracy of the allowed states so that the hole angular momentum becomes quenched  The hole therefore behaves as a simple isotropic j = 1/2 particle

j-j coupling of a j = 1/2 electron and hole results in a J = 1 triplet and a J = 0 singlet state  However, since the orbital angular momentum L is quenched in this case, the observed splitting involves only pure spin states, we therefore only use the quantum number S  Orbital angular momentum quenching is characteristic of many isoelectronic hole attractive defects in silicon, for example $Zn_A$ defect observed in CZ Si Zn [12] and an In related defect [13]  Figure 3 10 illustrates the effect of j-j coupling on hole attractive isoelectronic defects

For both cases described above, any degeneracy resulting from the local strain field or the j-j coupling can be removed by applying a magnetic field which results in a splitting of the states by an amount determined by

$$\Delta E = \pm \mu_B g_m B \qquad\qquad 3.35$$

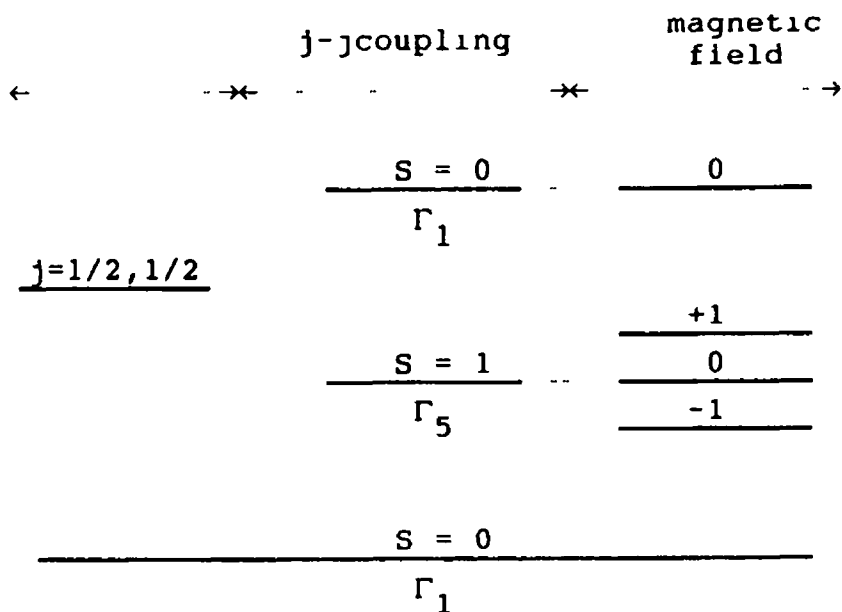where $\mu_B$ is the Bohr mabneton, $g_m$ is the g-factor and B is the magnetic field strength

```
                    j-jcoupling              magnetic
                                               field

    ←        - ⇥- -        -      -⇥-              - →

                          S = 0                   0
                        _____        _____
                            Γ₁
 j=1/2,1/2
 _____

                                                 +1
                                          _____
                          S = 1                   0
                        _____  -- _____
                            Γ₅                   -1
                                          _____


                          S = 0
_____
                            Γ₁
```

*Figure 3 10   The zero phonon level structure of a triplet - singlet bound exciton system.*

In figures 3 10 and 3 11 the expected splitting in a magnetic field is illustrated  The clear differences between the behaviour of electron attractive and hole attractive isoelectronic defects in a magnetic field provide a means of differentiating between these two types of defects

## 3.5 Conclusions

In this chapter consideration has been given to the theoretical aspects of applying perturbations to silicon crystals particularly with a view to uncovering the nature of defects imbedded in the cubic crystal structure   The techniques considered were temperature effects, uniaxial stress and Zeeman effects

In the next chapter the experimental arrangements necessary to carry out experiments that involve perturbations such as these will be considered

**References.**

[1]      G Davies, Physics Reports **176** (1989) 83

[2]      D B Fitchen Physics of Color Centres Edited by W B Fowler Academic Press (1968) 293

[3]      A A Kaplyanskii, opt Spectrosc **16** (1964) 329

[4]      A A Kaplyanskii, Opt Spectrosc **16** (1964) 557

[5]      A E Hughes and W A Runciman, Proc Phys Soc **90** (1967) 827

[6]      K Mohammed, G Davies and A T Collins, J Phys C **15** (1982) 2779

[7]      M Tinkham, Group Theory and Quantum Mechanics New York, McGraw-Hill (1964)

[8]      A L McCarren, H.J Ruskin, K G McGuigan and M O Henry IEE Proc Sci Meas Technol **141** (1994) 185

[9]      P.J Dean, R A Faulkner, J L Merz Solid State Commun **8** (1970) 2079

[10]    M O Henry, E C Lightowlers, N Killoran, D.J Dunstan, B C Cavenett J Phys C **14** (1981) L255

[11]    S P Watkins et al, Phys Rev B **29** (1984) 5727

[12]    Private communication J Campion

[13]    S P Watkins and M L W Thewalt, Phys Rev B **34** (1986) 2598

# Chapter 4
## Experimental Procedures

## 4.1 Introduction

To determine the fundamental properties of a defect it is necessary to measure the positions of the energy levels and the wavefunctions of the states introduced by that defect. Many parameters govern the ease, or otherwise, with which these properties may be determined, in this chapter the necessary experimental arrangements and sample preparation procedures appropriate to the techniques used are discussed

The various spectra addressed in this work arise from impurity levels lying within the energy gap of the silicon crystal The energy gap (Eg) of silicon is ≈ 1 1 eV, therefore spectral features due to optical excitation lie in the near infra-red region of the electro-magnetic spectrum, typically 0 5 - 1 1 eV The majority of defect levels in silicon have binding energies of less than 50 meV, consequently lattice vibrations will be strong enough to cause defects to thermally dissociate at high temperatures At higher temperatures an effective limit is set on the resolution of closely spaced spectral features due to the increased motion of the atoms about their equilibrium positions, thermal broadening of the defect levels occurs and consequently of the spectral features For these reasons it is necessary to perform most photoluminescence experiments at low temperatures

The constraints imposed by temperature as indicated above govern the experimental apparatus and procedures used throughout this work In this chapter the details of equipment and techniques used are described

## 4.2 Low Temperature Apparatus and Temperature Control

The cryostat used to achieve the necessary experimental temperatures was an Oxford Instruments continuous flow cryostat CF 1204 It operated on the principle of a continuous and controlled flow of coolant, in this case liquid helium, from a separate

storage vessel The coolant flowed through the heat exchanger of the cryostat where the temperature was measured and a resistive heater was powered using a temperature controller to maintain the desired temperature The heat exchanger and thus the sample space could be maintained at any temperature above the boiling point of the coolant and within the range of the control thermometer

To maintain the desired temperature and to insure adequate thermal insulation from the ambient laboratory atmosphere, the cryostat utilised an insulating vacuum space evacuated to better than $10^{-5}$ Torr This vacuum was achieved using a rotary backed diffusion pump The efficiency of the thermal insulating properties of the cryostat was increased by the use of low thermal conductivity combined with high mechanical strength materials, a radiation shield, at approximately 70 K, reduced the radiative heat
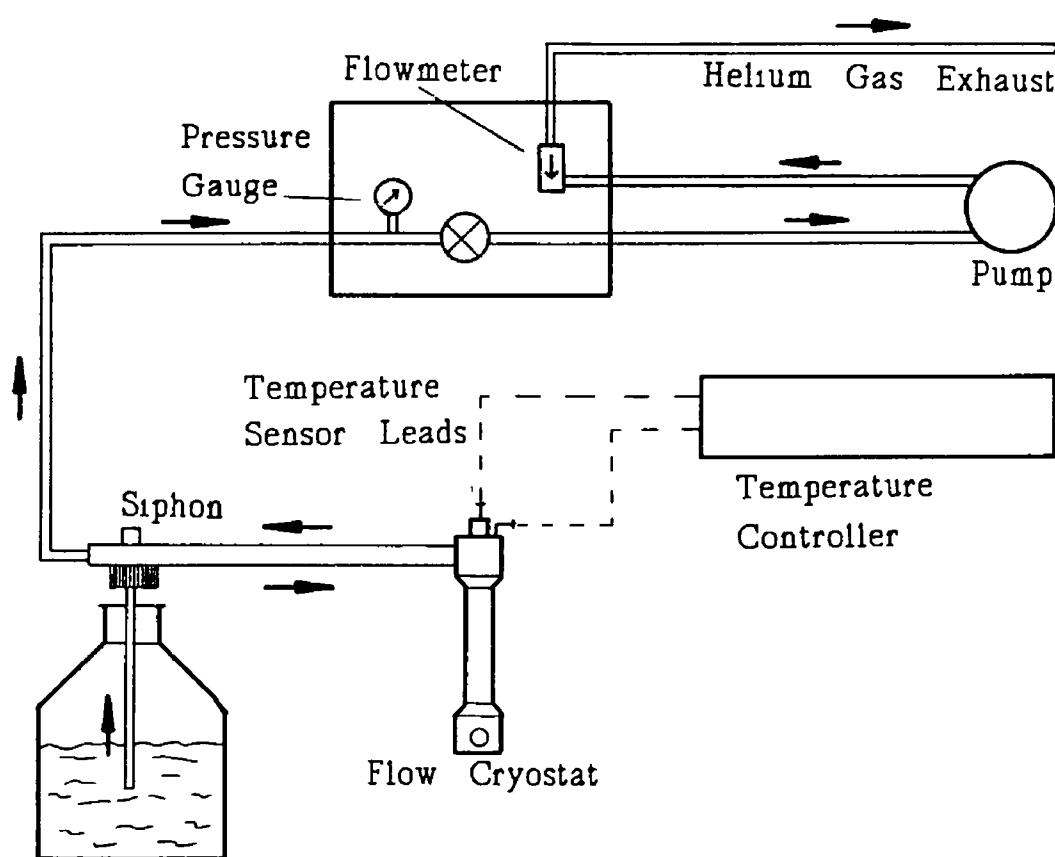


Figure 4 1 Schematic diagram of apparatus used to achieve temperatures in the range 4 2 - 300 K

load. A continuous transfer of liquid helium was achieved using the Oxford Instruments GFS300 gas cooled transfer tube. The flexible section of the transfer tube included a delivery tube which was radiation shielded by the concentric return flow of exhaust gas from the cryostat. This in turn was surrounded by an evacuated tube. This was a highly efficient system in which good use was made of the enthalpy of the exhausting gas to minimise incoming conducted heat. Figure 4.1 illustrates the cryogenic arrangement used for variable, low temperature experiments.

Control of the sample temperature was achieved by reducing the helium flow via a needle valve on the transfer tube until a temperature just below the working temperature was reached. An Oxford Instruments ITC4 temperature controller specifically intended for use in cryogenic applications was then employed in order to control the heater output so as to maintain the desired experimental temperature. The ITC4 allowed the proportional, integral and differential control terms to be adjusted to maintain temperature stability to within 0.1 K. During the course of this work a RhFe metal resistance sensor with a range of 3.8 - 300 K was used together with a 34 $\Omega$ resistive heater.

## 4.3 Optical Arrangement

The CF 1204 cryostat was equipped with three optical ports arranged at 90° intervals about the sample position. This allowed for excitation and collection of luminescence. For optimum light collection the arrangement made use of the large angles though which the luminescence was refracted as a result of the high refractive index of the material (n = 3.5 for Si), thus enabling collection of the luminescence with greater efficiency off the edges of the sample.

The arrangement of the optical components used to focus the excitation and to collect the emitted luminescence varied according to the source and spectrometer being used.

Two sources were employed, the first was an air cooled argon ion laser, operating on all lines, which required no focusing as the beam diameter was of the order of 7 mm$^2$ which was suitable for our sample size. In most cases the luminescence originated from within the bulk of the sample i.e. it was not confined to surface layers

as is the case for some damage related centres and so by using a source of longer wavelength, for which the penetration depth into the crystal was greater, a better signal to noise ratio was achieved In the latter case, the volume of material being excited was greater, leading to a larger number of luminescence centres contributing to the signal The source used in this case was a GaAs laser diode with peak emission wavelength at 810 nm A collimating lens assembly mounted directly in front of the laser diode gave a slightly diverging beam which was subsequently focused onto the sample with a final spot size of approximately 7 mm$^2$

Two spectrometers were used in this work, the first was a dispersive type instrument and the second a Fourier transform system

The experimental arrangement for the dispersive instrument is illustrated in figure 4 3, it consists of a Spex Industries 1704 1 m focal length Czerny-Turner spectrometer fitted with a grating ruled at 600 lines/mm with a blaze angle for 1 2 μm (optimised for the infra-red) A typical slit width of 200 μm gave a resolution of approximately 0 4 meV The grating was controlled by a P C via a Spex Mini-Step-Driver unit The
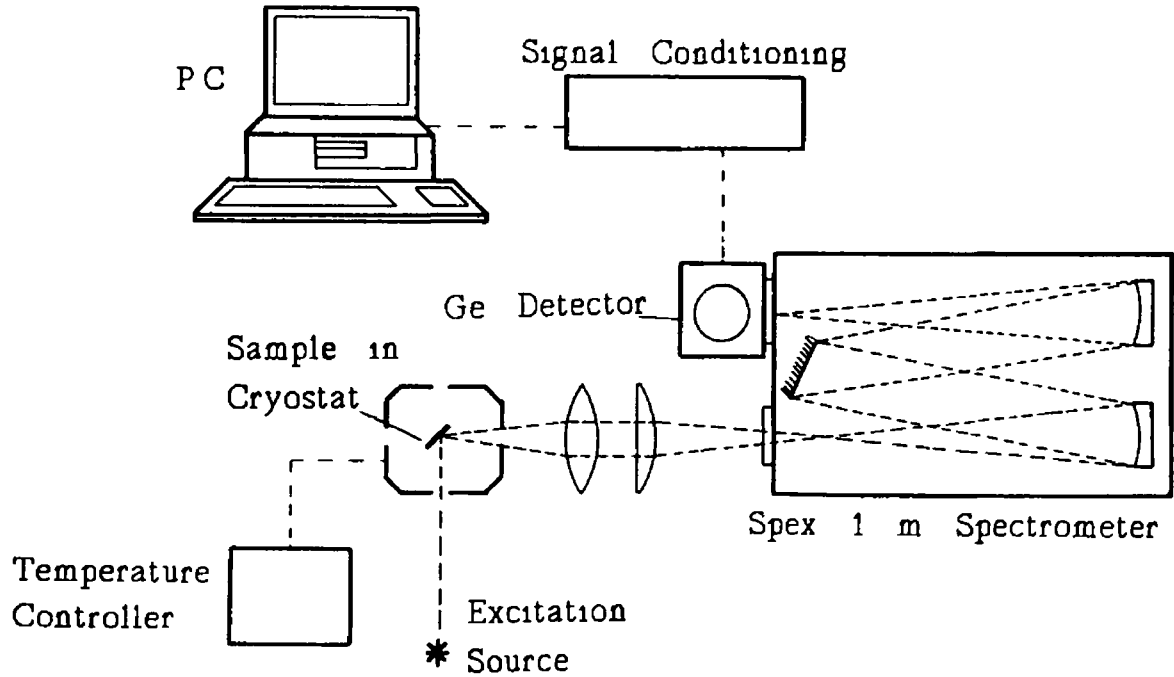


*Figure 4 2 Experimental arrangement for photoluminescence experiments using the dispersive system*

luminescence was focused onto the entrance slit of the monochromator by means of a collecting lens with f-number equal to that of the monochromator, this ensured maximum collection efficiency and minimum scatter A silicon filter at the entrance slit ensured that plasma line emission from the excitation source in the spectral region of interest did not reach the grating

The application of Fourier transform instruments to near infra-red spectroscopy and specifically to photoluminescence has occurred only within the past decade [1,2,3] Much higher sensitivity and data acquisition rates can be achieved by this method In most cases the major component of a system such as this is a Michelson
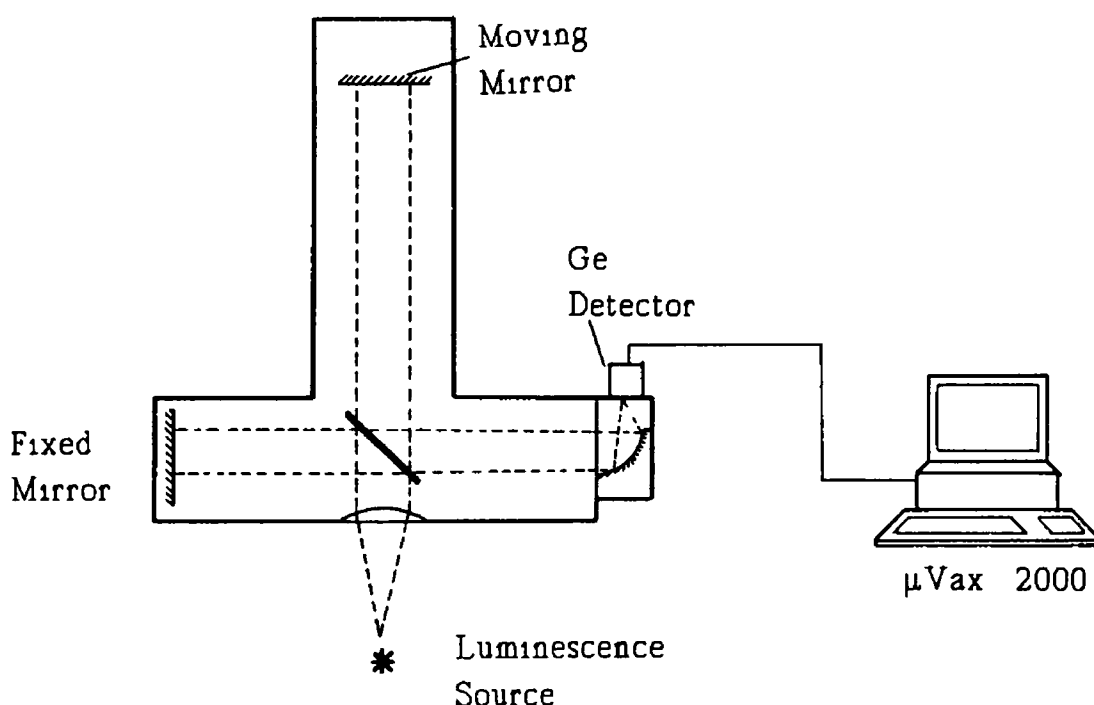


Figure 4 3 Fourier transform spectrometer, based on a Michelson interferometer

interferometer which produces an interferogram associated with all of the wavelength components in the incident light This represents the major gain in sensitivity as every component of the spectrum is being detected all of the time, rather than the small part which is incident on the exit slit of the monochromator at any one time when using a dispersive instrument The interferogram is then mathematically processed, by performing a Fourier transform in order to yield a spectrum
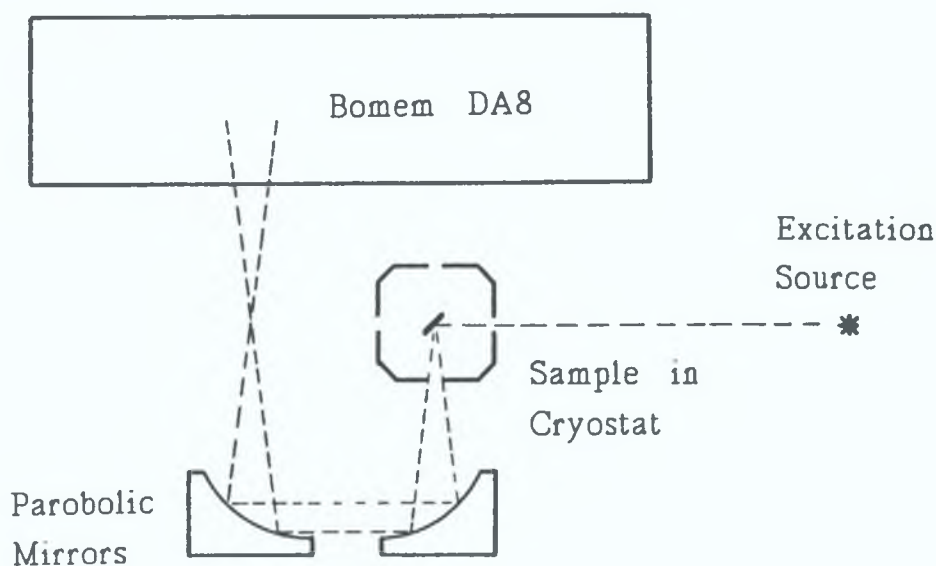
*Figure 4.4 Luminescence collection system for the FT spectrometer.*

The instrument used in this case was a BOMEM DA8 Fourier transform spectrometer, a schematic representation of which is illustrated in figure 4.3. The ultimate achievable resolution was of the order of .01 cm$^{-1}$, but for this work a typical resolution of 1 cm$^{-1}$ was used as this proved adequate for the spectra involved. The range of the instrument was determined by the range of both the detector and the beamsplitter. The beamsplitter material was BK5 glass which had a transmission curve from 3500 - 30000 cm$^{-1}$; the detector used was a germanium detector and set the ultimate detection limits to 6000 - 10000 cm$^{-1}$. Considerable computing power was required in order to control the system, monitor the stability of the instrument (in particular the position of the scanning mirror), acquire the raw data and compute the Fourier transform in order to yield a spectrum. A DEC micro VAX 2000 was used for this purpose. The luminescence collection arrangement for this system is illustrated in figure 4.4. Parabolic mirrors were used to overcome the problem of chromatic abberation and to maximise the collection efficiency.

For both the dispersive and the Fourier transform systems North Coast cooled germanium detectors were used. Two separate detectors were used with their response times optimised for the spectrometer with which they were operating. The detectors consisted of a reverse biased p-i-n diodes with low noise pre-amplifier. The diode, the feedback resistor and the FET of the preamplifier were cooled, using liquid nitrogen

stored in a dewar in the casing These combined to give a highly sensitive, low noise performance in the spectral range of interest

## 4.4 Uniaxial Stress Apparatus

Uniaxial stress measurements were used to determine the response of electronic states to the movement of atoms near an optical centre The technique involved the measurement of shift rates and/or splittings of spectral lines as a result of the application of uniaxial stress

The samples were cut to a cuboid (12x4x2 mm) with the longest axes parallel to one of the three major crystallographic axes namely <100>, <110> and <111> To ensure maximum stress homogeneity required samples to have a large ratio of length to width and thickness

To minimise thermal broadening of the spectral features it was necessary for the experiments to be carried out at liquid helium temperatures, the stress assembly was therefore constructed to fit inside the Oxford Instruments CF 1204 flow cryostat, a schematic representation of which is illustrated in figure 4 5 The stress rig was constructed using stainless steel and consisted of an outer hollow cylinder with the samples mounted exactly perpendicularly between two hardened steel pistons which served to compress the sample when an external force was applied via a push rod The samples were mounted such that their long axis was exactly parallel to the vertical axis of the stress cell Apertures in the body of the stress assembly about the sample position and coinciding with the optical ports of the cryostat allowed optical access to both excite and collect the luminescence In order to minimise heat loss the push rod was hollow The external force was applied to the push rod by the compression of a steel spring The force produced by the spring was measured with a Bofors KRA-1 piezoelectric load cell mounted between the compressed spring and the push rod which gave a voltage output as a function of the applied force (0 3 mV per 1 kg load) [2] An empirical conversion equation for the stress cell output voltage to applied force is given in equation 4 1

$$Stress(MPa) = \frac{9\,8(V - V_0)}{A(0\,286)} \qquad\qquad 4\,1$$

TB  Threaded bar
S   Spring
LC  Load cell

SC  Stress cell

CR  Cryostat
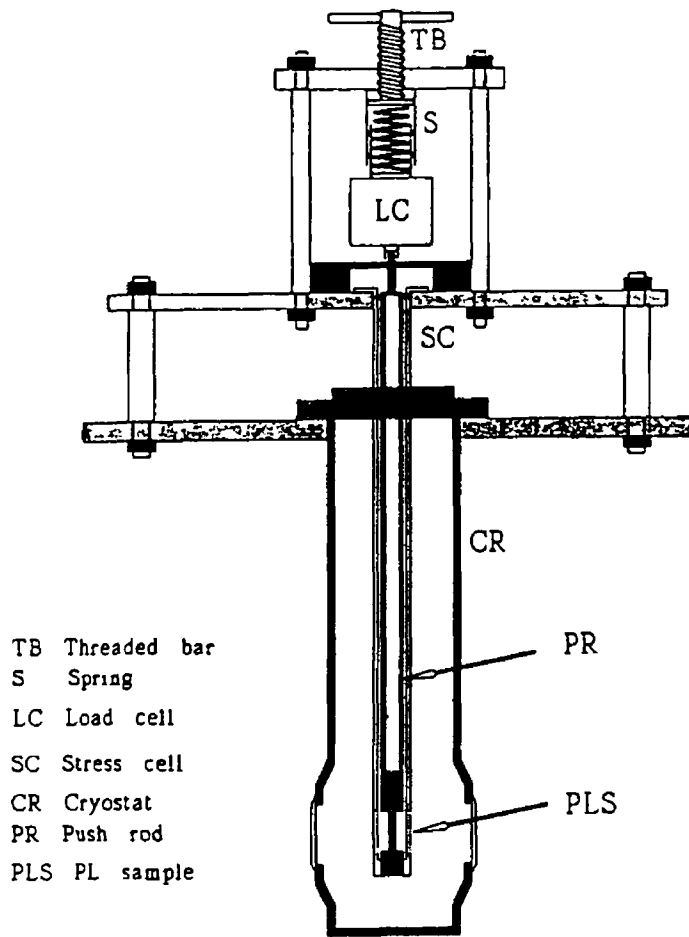PR  Push rod

PLS PL sample

*Figure 4 5   Uniaxial stress apparatus*

where $V_0$ is the load cell voltage at zero stress, V is the load cell voltage at a finite stress and A is the sample cross sectional area in $mm^2$  Stresses of the order of 100 MPa produced perturbations of a few meV, which gave appreciable effects since they were found to be large compared with the spectral line widths (approximately 0 1 meV) of the zero phonon lines

## 4.5 Zeeman Measurements

Zeeman studies were conducted at the University of Aveiro, Portugal using an Oxford Instruments Spectro Mag 4 liquid helium bath cryostat that employed a superconducting split pair magnet mounted horizontally in the tail attachment. Fields of up to 5 Tesla were available. Windows fitted to the tail assembly allowed optical access to the sample housed in the centre field region, through the horizontal magnet bore

Two options were available for mounting the samples within the magnetic field, namely the Faraday configuration and the Voigt configuration, both of which are
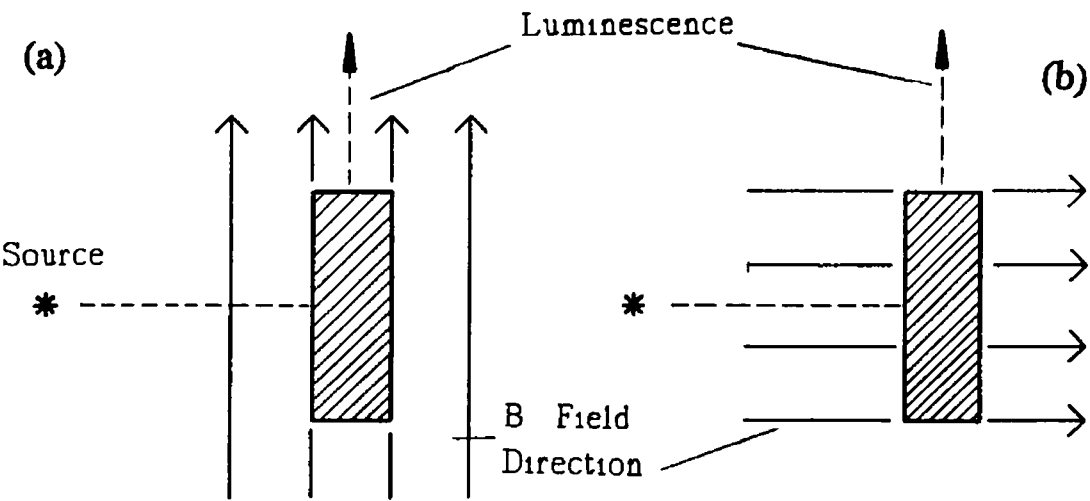


*Figure 4 6    (a) Faraday and (b) Voigt configuration for Zeeman studies in luminescence    The horizontal plane through the mounted sample is shown*

illustrated in figure 4 6    For these experiments the Faraday configuration was used, in which the direction of the magnetic field was parallel to the spectrometer axis and the excitation was perpendicular to the field

## 4.6 Sample Preparation

The standard samples used in this study consisted of CZ (high oxygen), high resistivity silicon wafers    The wafers were ion implanted with $^9$Be in the range $10^{13}$ -

$10^{17}$ atoms/cm$^2$ with ion energies in the range 50 - 200 keV  After implantation or irradiation samples were prepared by first cleaving the wafers to produce samples with dimensions of approximately 5 x 4 mm  Most wafers used were oriented in the <100> direction and so cleaved readily by applying pressure via a diamond tipped scribe at the edge of the wafer

Samples were subsequently cleaned using the RCA cleaning procedure (appendix A) which removed all organic and metallic contamination from the surfaces  Samples were placed in a cleaned 10 mm diameter quartz tube, open at both ends, one end of which was attached to a helium gas supply which provided a slight over pressure in the tube, thus ensuring that any out diffused elements from the quartz tube or the furnace were carried away from the sample  The quartz tube was placed in a Carbolite CFM 1200 tube furnace, which provided temperatures in the range from room temperature to 1200°C  The annealing apparatus is illustrated in figure 4 8  Typical anneal times for
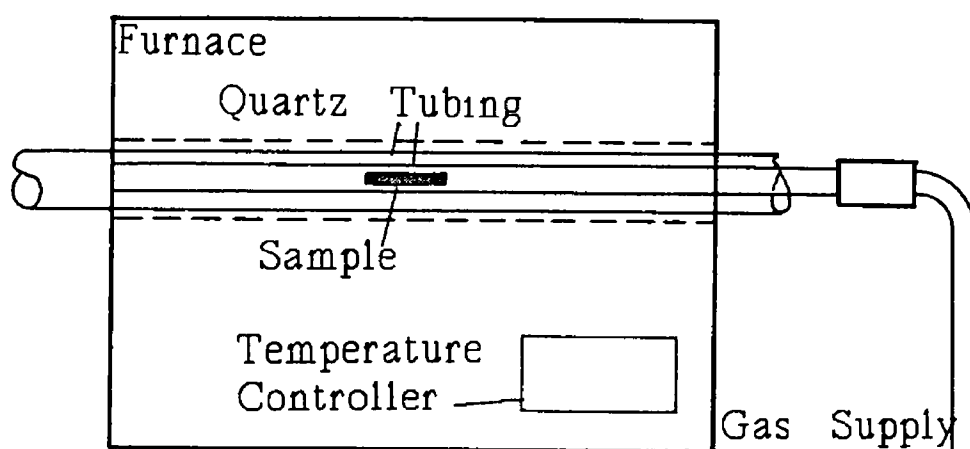


*Figure 4 7  Annealing apparatus*

the various samples was 30 minutes

It was found that the rate at which samples were cooled after annealing had a significant effect on the defects formed  It was therefore concluded that the formation kinetics of some of the defects and in particular the Be related defects was strongly dependent on the cooling rate  Typical cooling rates to optimise this defect was of the order of 100°/min  To achieve this the quartz tube was withdrawn 2 cm every 30

seconds from the furnace

Subsequent to the annealing stage, etching of some of the samples was required, in general this was done to remove the damaged region from the surface layer of the sample which arose as a result of implantation  In order that the etch would be consistently reproducible and uniform over the entire sample, it was necessary to clean the samples (using the RCA technique) immediately prior to etching  The etchant used was a 10 1 mixture of $HNO_3$ and HF acid at approximately room temperature  This removed typically 2 μm in 30 s from the <100> surface of the silicon, provided the etching solution was constantly agitated while the samples were immersed in it  This was most effectively accomplished with the use of a PTFE coated magnetic stirrer  Samples were rinsed thougherly with de-ionised water after the etching procedure

The only exception to the above procedures was encountered in the preparation of oriented samples for uniaxial stress and Zeeman measurements  In this case pre-cut samples from oriented silicon ingots were used  In their as received state these samples had typical dimensions of 12 x 4 x 2 mm and possessed a poor 'roughened' surface quality  It was therefore necessary to etch these samples prior to implantation  The etching solution as outlined above was used, which required an etching time of the order of 7 - 8 minutes  It was found that by increasing the strength of the etching solution by increasing the proportion of HF acid the process was, as expected, speeded up  However the resulting surface finish was not uniform and often pitted in appearance and the edges of the sample were considerably 'rounded'  All other procedures were as outlined above

Samples were mounted on the sample holder of the cryostat, as indicated in figure 4 9(a), using PTFE tape to secure them in place  In the case of the uniaxial stress samples great care was necessary in insuring the principal axis of the sample was exactly parallel to the axis of the stress rig  Insufficient care in this respect caused spurious stress split components to be detected due to inhomogeneous stresses being experienced by the misaligned sample  Double sided sticky tape was used to hold the sample in position while the rig was being assembled  Figure 4 9(b) illustrates the samples mounted for photoluminescence and for uniaxial stress measurements
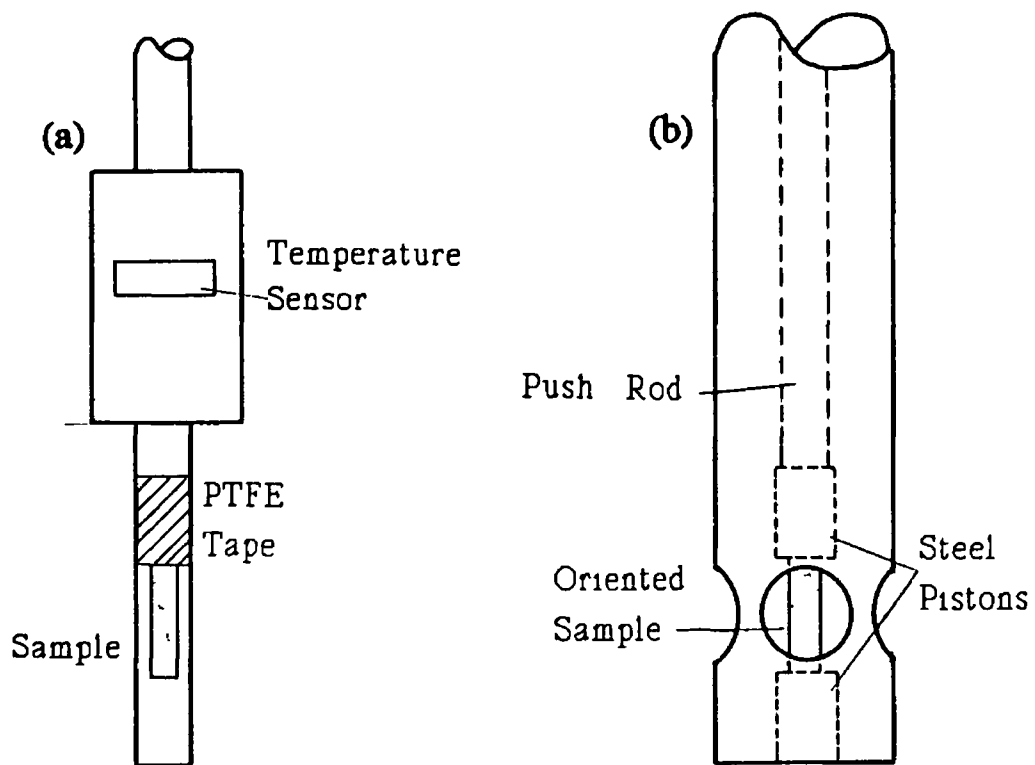
*Figure 4 8  Sample mounting arrangement (a) for PL measurements and (b) for uniaxial stress experiments*

**References:**

[1]    P McL Colley and E C Lightowlers, Semicond Sci Technol **2** (1987) 157

[2]    M L W Thewalt, M K Nissen, D J S Beckett and K R Lundgren Impurities, Defects and Diffusion in Semiconductors Bulk and Layered Structures, Mat Res Soc Symp Proc **163** (1990) 221

[3]    E C Lightowlers Growth and Characterisation of Semiconductors Edited by R A Stradling and P C Klipstein Bristol Adam Hilgar (1990) 135

# Chapter 5

## Be Related Photoluminescence System

## 5.1 Introduction

In chapter 1, Be related defects in silicon were reviewed. The work of Gerasimenko et al [1] revealed a number of radiative recombination centres which were assumed to contain beryllium atoms. Figure 1.8 reproduced the annealing behaviour of the luminescence lines observed. Gerasimenko et al attributed two of the lines (with ZPL's at 1.1382 eV and 1.0528 eV) to the complexing of oxygen with beryllium. In this work CZ silicon was implanted with $^9$Be and upon heat treatment produced a PL spectrum with zero phonon line at 1137.98(5) meV together with a characteristic sideband structure. The ZPL is believed to be consistent with the 1.1382 eV line of Gerasimenko et al, while a local mode in the sideband structure is consistent with the 1.0528 eV line. In this chapter a survey of the photoluminescence spectra obtained from Be implanted silicon will be presented, with particular reference to the chemical constituents of the defect. The PL spectrum of the defect displayed a characteristic sideband structure consistent with electron-lattice coupling. The relaxation associated with the luminescence process which produces this sideband will also be considered.

## 5.2 The 1137.98 Be related PL System (Be$_A$)

Figure 5.1 contains a typical photoluminescence spectrum, obtained at 12 K, of CZ silicon implanted with $^9$Be and subjected to an annealing temperature of 600°C as outlined in section 4.6. The PL spectrum consists of a strong no phonon transition at 1137.98(5) meV accompanied by an amply structured vibronic sideband. The phonon assisted transitions (TA and TO) are located at 1121.26 and 1083.64 meV respectively; their positions correlate directly with the peaks in the phonon density of states for silicon. Dominant in the sideband structure are the $L_1$, $L_2$ and $L_3$ lines which are attributed to localised vibrational modes of the defect; they are replicated in the
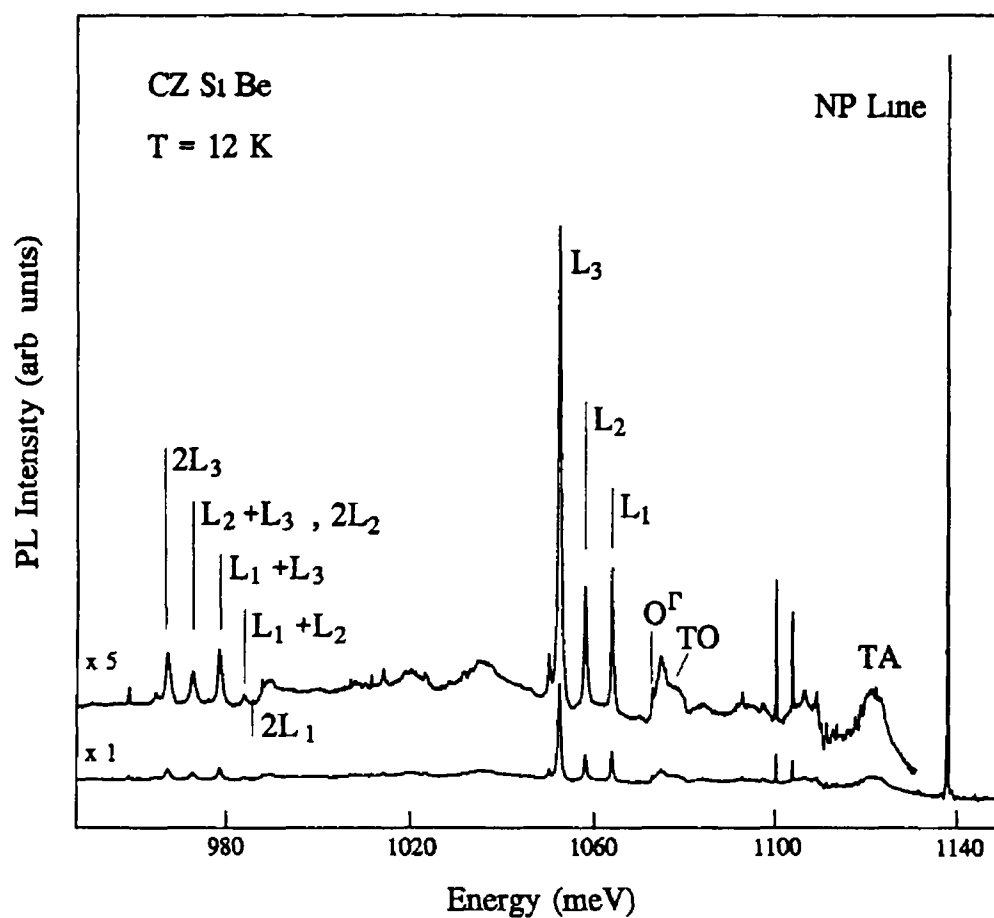
*Figure 5 1   Photoluminescence spectrum of CZ Si implanted with Be*

spectrum as two phonon satellites labelled $2L_1$, $L_1+L_2$, $L_1+L_3$, $2L_2$, $L_2+L_3$ and $2L_3$ Details of the sideband structure will be analysed in greater detail below   The energies, labelling and shift from zero phonon line (ZPL) of the main features in the spectrum are listed in table 5 1, this defect is assigned the label $Be_A$

| Spectral Feature | Energy (meV) ±.05 | Shift From ZPL (meV) | Phonon Identification Label  Energy(meV)* |
|---|---|---|---|
| ZPL | 1137 98 | 0 | |
| | 1121 26 | 16 73 | TA        18 6 |
| | 1083 64 | 54 35 | TO        57 5 |
| | 1073 87 | 64 11 | $O^{\Gamma}$ cutoff  64 2 |
| $L_1$ | 1063 99 | 73 78 | |
| $L_2$ | 1058 10 | 79 77 | |
| $L_3$ | 1052 37 | 85 52 | |
| $2L_1$ | 986 16 | 151 74 | |
| $L_1+L_2$ | 984 18 | 153 72 | |
| $L_1+L_3$, $2L_2$ | 978 71 | 159 27 | |
| $L_2+L_3$ | 972 72 | 165 26 | |
| $2L_3$ | 967 11 | 170 88 | |

*Table 5 1     Vibronic sideband features for Be related defect*
*\* Values taken form reference [2]*

## 5.3 Heat Treatment

During implantation the implanted species has a low probability of coming to rest within one of its stable configurations and so subsequent annealing is needed before the implanted ions become involved in defects characteristic of the chemical identity of the implanted ion  In order for defect complexes to form, following ion implantation, some form of heat treatment is usually required to give the various impurities sufficient energy to move and complex  Interstitial atoms require less energy to become mobile than substitutional atoms, due to their relatively small activation energies (in the range 0 5 - 1 6 eV)  Substitutional impurities, on the other hand, require sufficient energy to jump from one substitutional site to an adjacent one atoms - activation energies in the range 3 - 4 eV are typical

Be implanted CZ Si samples were subjected to annealing temperatures in the range 200 - 1000°C  Figure 5 2 contains typical low temperature photoluminescence spectra obtained for the annealed samples  Following implantation and annealing at T
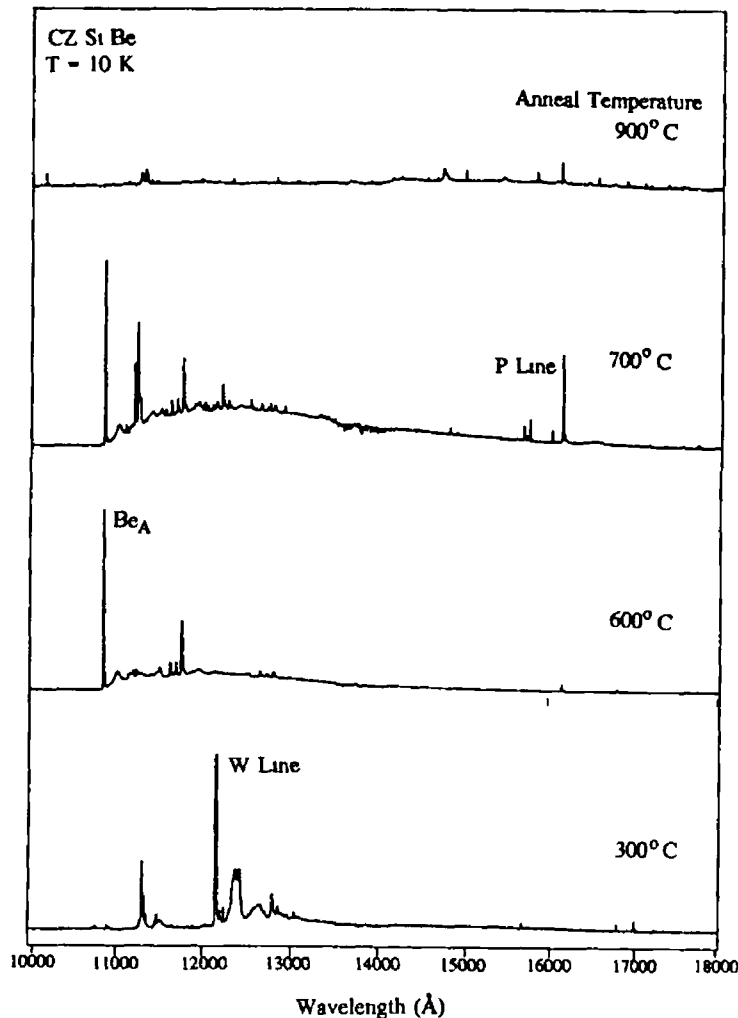
*Figure 5 2   PL spectra of CZ Si Be annealed in the range 200 - 1000°C*

≤ 300°C, the low temperature PL spectra were dominated, as expected, by damage related features, most notably the W line consisting of a strong ZPL at 1018 9 meV At this point no additional PL features were identified as relating to the presence of Be in the implanted layer   Samples annealed in the range 550 - 800°C produced PL spectra which were dominated by the PL system characteristic of the $Be_A$ defect   Samples annealed above 850°C produced no additional PL features

The normalised PL intensity, for the $Be_A$ defect, as a function of anneal temperature is illustrated in figure 5 3   The optimum defect production temperature is 600°C   Comparing figure 5 3 with the PL intensity as a function of anneal temperature for the principal lines observed by Gerasimenko et al [1] (reproduced in figure 1 8) reveals similar behaviour

Isothermal annealing was carried out at 600°C   In figure 5 4 $\ln(I/I_{t=0})$ is plotted as a function of annealing time   Within experimental accuracy (approximately 10%),
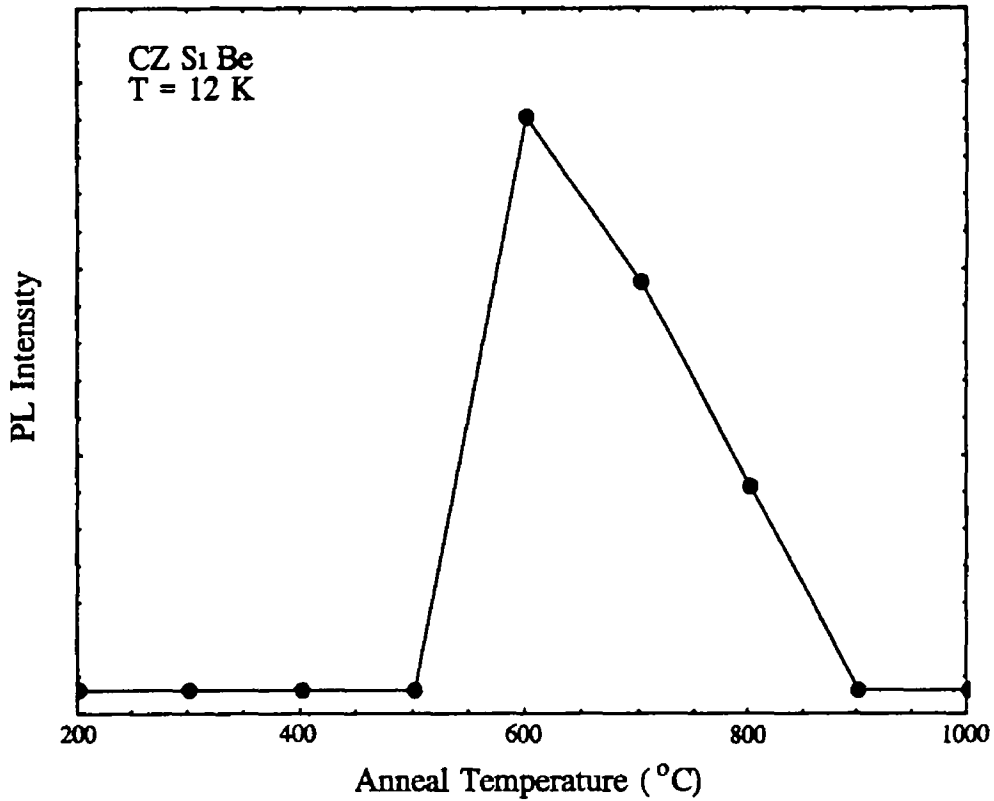
*Figure 5 3   Normalised PL intensity of $Be_A$ annealed in the range 200 - 1000°C*

the values follow a straight line for anneal times up to approximately 20 mins, thereafter the defect concentration begins to saturate   The growth in intensity up to t = 20 mins can be described by an exponential function

$$[I(Be_A)] = [I(Be_A)_{t=\infty}]\exp(-ct)$$   5.1

where c is the rate constant obtained from the slope of the least squares fit to the linear region of the data, it is found to be 2 3(3) x10$^3$ s$^1$   An estimate of the activation energy, $E_a$, for the formation of the $Be_A$ defect can be extracted from the following equation

$$c = c_0 \exp\left(-\frac{E_a}{kT}\right)$$   5 2

where $c_0$ can be estimated, to a first approximation, from the relation

$$c_0 = \frac{kT}{h}$$   5.3

where T is the absolute temperature [3]   $c_0$ is estimated to be 1 81 x 10$^{13}$ s$^1$   The
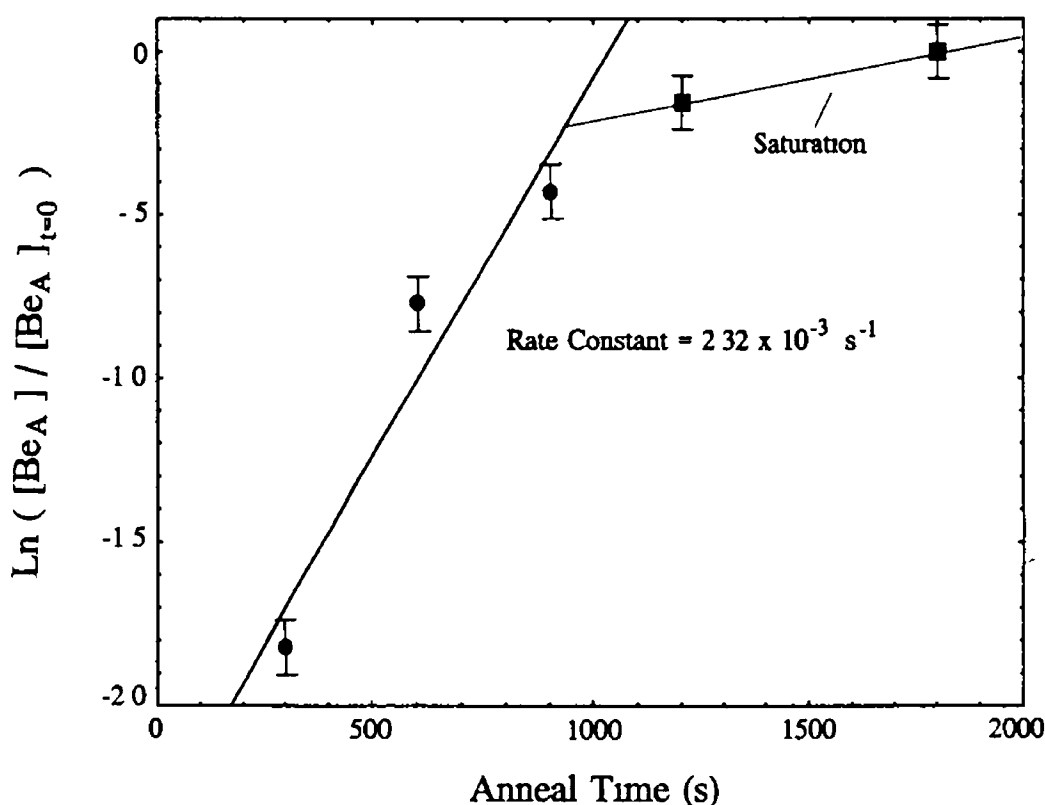
*Figure 5 4  Ln (Normalised Intensity) as a function of anneal time, anneal temperature was 600°C*

activation energy of formation of the defect is found to be approximately 2 7(3) eV  If we compare this value to typical activation energies for impurity atoms in silicon, we find that it is in the mid range between typical interstitial diffusion mechanisms and substitutional diffusion

Following the annealing experiments, optimum conditions for the production of the defect were sought  Samples annealed at 600°C for thirty minutes were subjected to a quenching treatment by cooling in air  Subsequent PL spectra failed to reveal the presence of this defect but instead produced a spectrum characteristic of the luminescence produced by the isoelectronic $Be_I$-$Be_S$ pair defect  It was discovered that by withdrawing the quartz tube containing the sample slowly from the furnace and then allowing the sample to reach room temperature without being aided by a quenching treatment optimum signal to noise conditions for the defect were reached

## 5.4 Chemical Constituents of the Defect

The identification of the chemical constituents of defects found in silicon is difficult and in the absence of isotope substitution experiments one has to rely on circumstantial evidence to obtain this information. Defects which are formed after heat treatments such as is described above can comprise any of a large range of impurities, some of which may be present in the starting material while others may be introduced during the implantation process. A further consideration is the residual impurities present even in relatively intrinsic silicon, most notably boron and phosphorous. As the Be was introduced into the silicon by ion implantation, isotopes of other impurities which have an equal mass to that of the implanted ion which may be present in the target material of the ion implantation system may also need to be considered. Listed in table 5 2 is a range of possible defect constituents and where available the activation energies associated with them.

| Impurity | Activation Energy |
|---|---|
| Silicon (interstitial) | Mobile T < R T |
| Silicon (substitutional) | 4 8 eV |
| Oxygen (interstitial) | 0 23 eV |
| Implanted Species - Beryllium | No data available, assumed mobile at R T |

*Table 5 2   Possible defect constituents of the Be$_A$ defect   Column 2 lists typical activation energies for each species, where available*

In attempting to identify the actual chemical constituents of the defect it is important to consider all of the above impurities as possible defect constituents. A comprehensive range of experiments was performed in order to confirm or eliminate possible constituents, a summary of which will now be presented.

Table 5 3 lists the samples investigated and the treatments to which they were subjected. The standard sample preparation technique used was consistent with that described for sample 1 of this table.

| No. | Starting Material | Implantation Dose  Energy | Clean | Anneal 600°C | Post Anneal Etch | Anneal 450°C |
|---|---|---|---|---|---|---|
| 1 | p CZ Si Be | 1e15  200 keV | RCA | 30 mins | no | no |
| 2 | n CZ Si Be | 1e15  200 keV | RCA | 30 mins | no | no |
| 3 | p CZ Si Be | 1e15  200 keV | RCA | 2 mins | no | no |
| 4 | p CZ Si Be | 1e15  200 keV | RCA | 5 mins | no | no |
| 5 | p Cz Si Be | 1e15  200 keV | RCA | 10 mins | no | no |
| 6 | p CZ Si Be | 1e15  200 keV | RCA | 15 mins | no | no |
| 7 | p CZ Si Be | 1e15  200 keV | RCA | 20 mins | no | no |
| 8 | p CZ Si Be | 1e15  200 keV | RCA | 30 mins | no | no |
| 9 | p FZ Si Be | 1e15  200 keV | RCA | 30 mins | no | no |
| 10 | p FZ Si Be (O Diff) | 1e15  200 keV | RCA | 30 mins | no | no |
| 11 | p CZ Si Be | 1e15  200 keV | RCA | 30 mins | 2 μm | 24 Hrs |
| 12 | p CZ Si Be | 1e15  200 keV | RCA | no | 2 μm | 24 Hrs |
| 13 | p CZ Si Be | 1e15  200 keV | RCA | 30 mins | 2 μm | 48 Hrs |
| 14 | p CZ Si Be | 1e15  200 keV | RCA | no | 2 μm | 48 Hrs |
| 15 | p CZ Si Be | 1e15  200 keV | RCA | 30 mins | 2 μm | 72 Hrs |
| 16 | p CZ Si Be | 1e15  200 keV | RCA | no | 2 μm | 72 Hrs |
| 17 | p CZ Si Be | 1e15  200 keV | RCA | 30 mins | 2 μm | 96 Hrs |
| 18 | p CZ Si Be | 1e15  200 keV | RCA | no | 2 μm | 96 Hrs |
| 19 | p CZ Si Be | 1e15   50 keV | RCA | 30 mins | no | no |
| 20 | p CZ Si Be | 1e15  100 keV | RCA | 30 mins | no | no |
| 21 | p CZ Si Be | 1e15  200 keV | RCA | 30 mins | no | no |
| 22 | p CZ Si Be | 1e15  200 keV | RCA | 30 mins | no | no |
| 23 | p CZ Si Be | 1e15  200 keV | RCA | 30 mins | 2 μm | no |
| 24 | p CZ Si Be | 1e15  200 keV | RCA | 30 mins | 4 μm | no |

## 5.5 Influence of Oxygen

In section 1 3 it was seen that oxygen is incorporated as an interstitial atom into silicon and is present in high concentrations particularly in Czochralski grown silicon Interstitial oxygen is electrically neutral, but it is found to complex with other impurities to form defect centres which, in certain circumstances, become electrically and/or optically active In order to assess the influence of oxygen on the $Be_A$ defect, samples were produced by implantation of $^9Be$ into both CZ and FZ material Spectra obtained
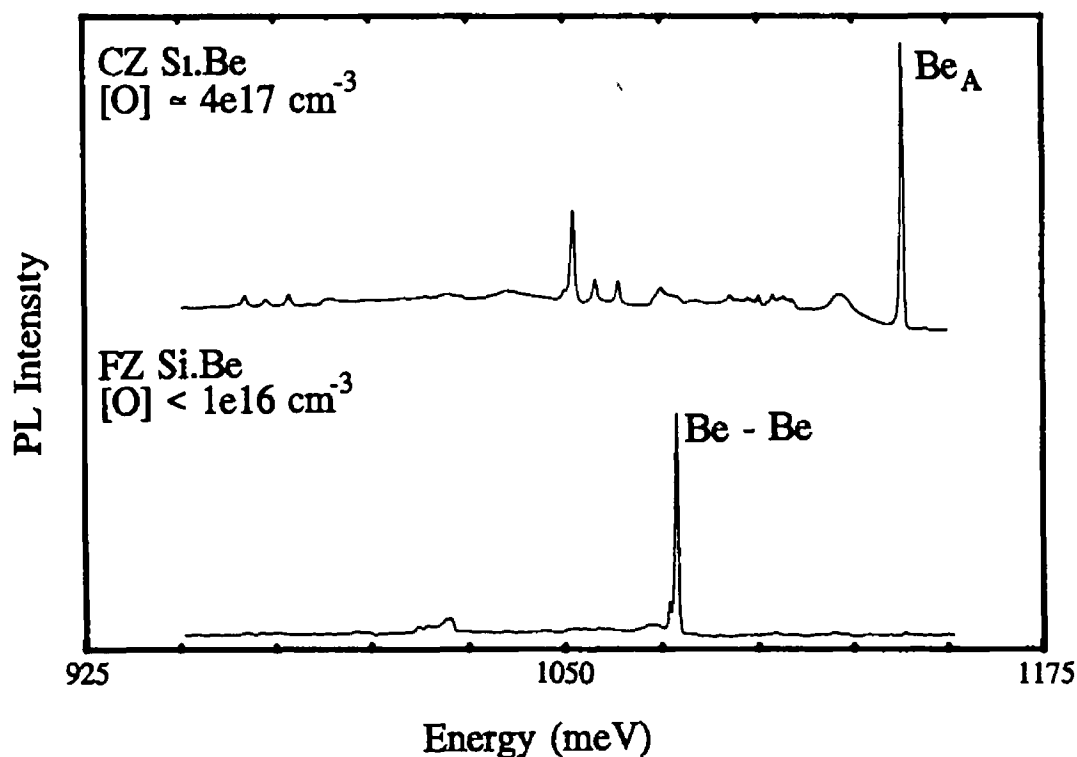


Figure 5 5   Comparison of CZ and FZ material, both implanted with an equivalent dose and energy of Be ions and similarly treated

from both samples are illustrated in figure 5 5   The CZ spectrum is dominated by the 1138 meV zero phonon line and it's characteristic sideband structure whereas the FZ material is dominated by luminescence characteristic of the Be pair   A further sample was prepared from a piece of FZ material onto which an oxide layer 1700 Å thick was grown, this sample was placed in a furnace at 1200°C for 8 hours in an oxygen rich atmosphere in order to diffuse oxygen into the bulk of the material   From the diffusion coefficient of interstitial oxygen in silicon the oxygen diffused depth was calculated to

be ≈ 35 μm after the diffusion process  This sample, together with an undiffused FZ sample from the same wafer were subsequently implanted to the same dose and energy with Be ions as the standard samples  The spectra obtained from both samples, following an anneal at 600°C, were dominated by Be-pair luminescence  The luminescence associated with the 1138 meV Be defect was present in both samples, but with a signal to noise ratio, for the ZPL, of ~ 1 5 and ~ 1 3 for the diffused and undiffused samples respectively

An estimate of the oxygen content of the CZ and FZ samples was obtained from the intensity of the 9 μm oxygen related infra red absorption peak  Samples of known oxygen content were used to calibrate the system  The oxygen content of the CZ material was approximately $5 \times 10^{17}$ atoms/cm$^3$, while the oxygen content of the FZ material was $< 1 \times 10^{16}$ atoms/cm$^3$  Infrared absorption spectra of CZ and FZ samples
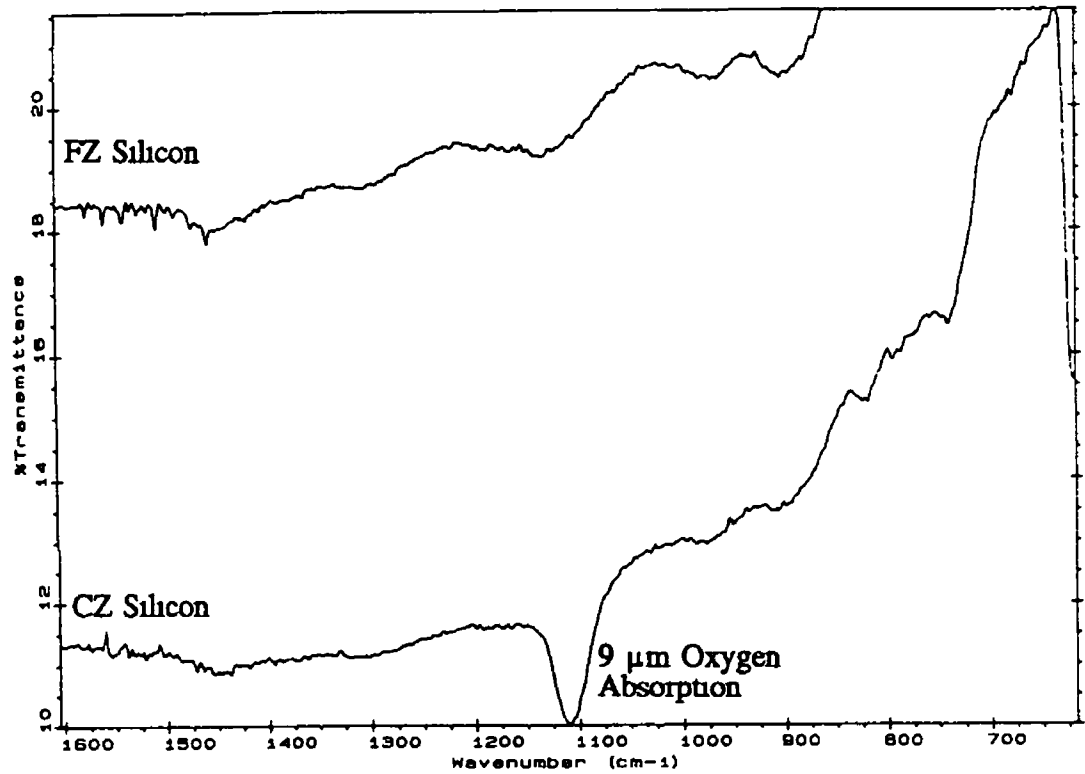


Figure 5 6   Infra-red absorption spectra of CZ (oxygen rich) and FZ (oxygen lean) silicon

in the range of interest are shown in figure 5 6  These measurements were carried out on a Nicolet IR FTIR spectrometer at room temperature  Similar measurements were carried out on CZ samples in their as-implanted state and on samples which had been

annealed in order to optimise for $Be_A$ defect, no change in the intensity of the 9 μm peak was recorded   It was concluded on the basis of the circumstantial evidence presented above that oxygen was a likely constituent of the defect

Much research on oxygen in silicon has centered on the production of thermal donors during prolonged heat treatments in CZ silicon   The ability of thermal donors to form in material in which $Be_A$ was formed was investigated   Pairs of samples were produced, labelled 11 - 18 in table 5 3, one of which was treated to produce the Be related defect the second of which was not   Pairs of samples were subjected to prolonged heat treatments of 24, 48, 72 and 96 hours at 450°C, the temperature at which thermal donor production is most vigorous   The resulting PL spectra for 72 and 96 hour
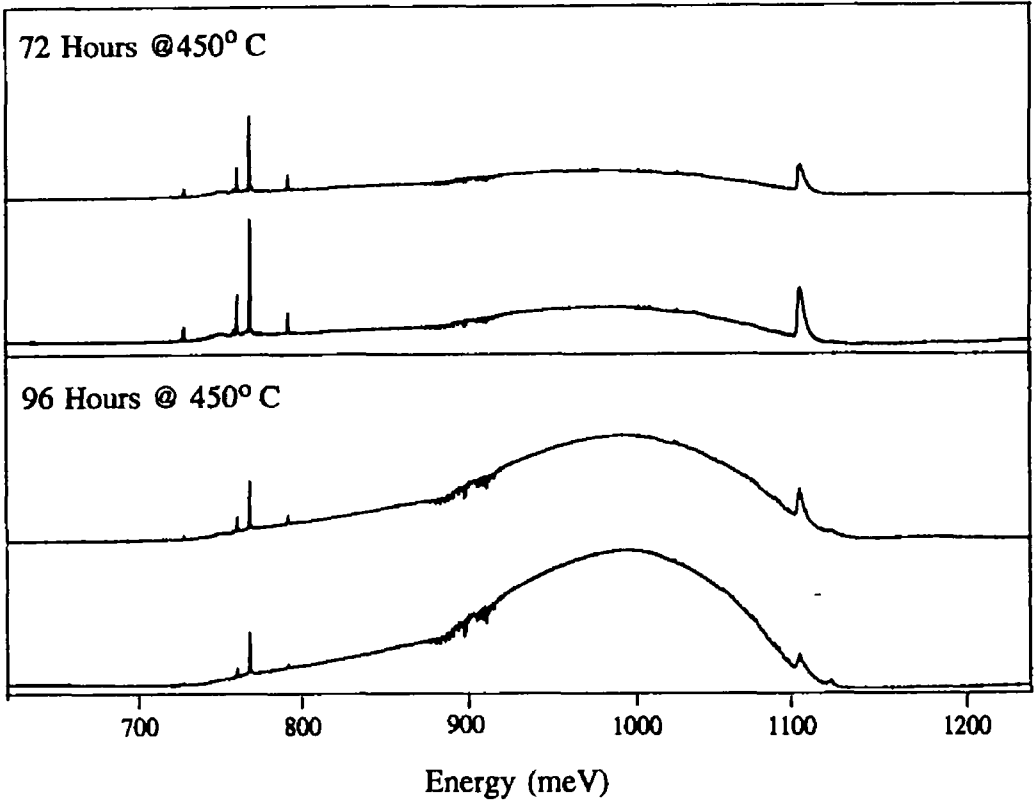


Figure 5 7   PL spectra of samples annealed to produce thermal donors, the upper spectrum in each case was treated to maximise the concentration of the $Be_A$ defect

anneals are shown in figure 5 7   The total luminescence intensity calculated for the pairs of samples is shown in figure 5 8   In each case the total PL intensity was less in the samples with the $Be_A$ present when compared to the sample with no Be defect present   It appears that the presence of the $Be_A$ defect inhibits the production of thermal donors
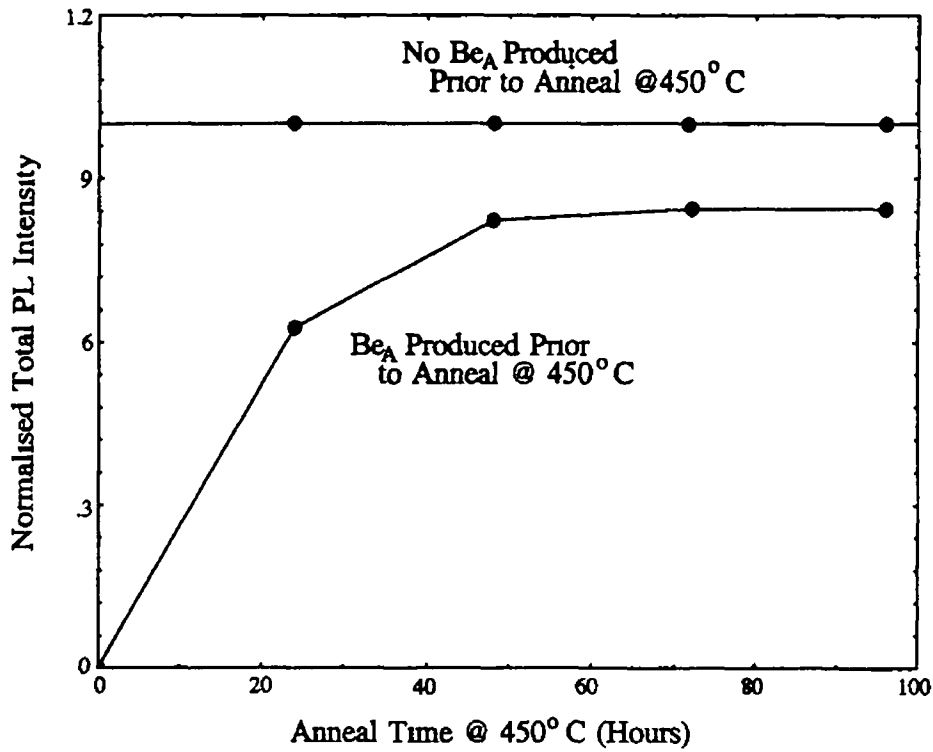
1.2

No Be_A Produced
Prior to Anneal @450°C

9

6

Be_A Produced Prior
to Anneal @ 450°C

.3

0

0    20    40    60    80    100

Normalised Total PL Intensity

Anneal Time @ 450° C (Hours)

*Figure 5 8   Normalised total PL intensity as a function of anneal time at 450°C*

## 5.6 Conductivity Type

Even in high purity, high resistivity, silicon residual impurities which determine its conductivity type are present   Both n-type and p-type samples were compared in order to eliminate these dopants as possible defect constituents   Boron (p-type) and phosphorous (n-type) were present in the starting materials with concentrations in the range $< 1 \times 10^{13}$ atoms/cm$^3$   Figure 5 9 contains spectra from both n-type and p-type material which were similarly treated in all other respects   The production of $Be_A$ was favoured in p-type material   Ratioing the intensities associated with the ZPL's of the $Be_A$ and Be-pair defects in both material types reveals a ratio of ~ 6 4 in p-type material and ~ 1 6 in n-type material   The Be-pair defect is an electron attractive isoelectronic defect[4]   If we consider the $Be_A$ defect to consist of an isoelectronic centre, which is either electron or hole attractive then the fact that the defect is favoured in p-type material points to it being primarily a hole attractive defect   In n-type material it is more difficult to maintain the bound hole necessary to capture the loosely bound
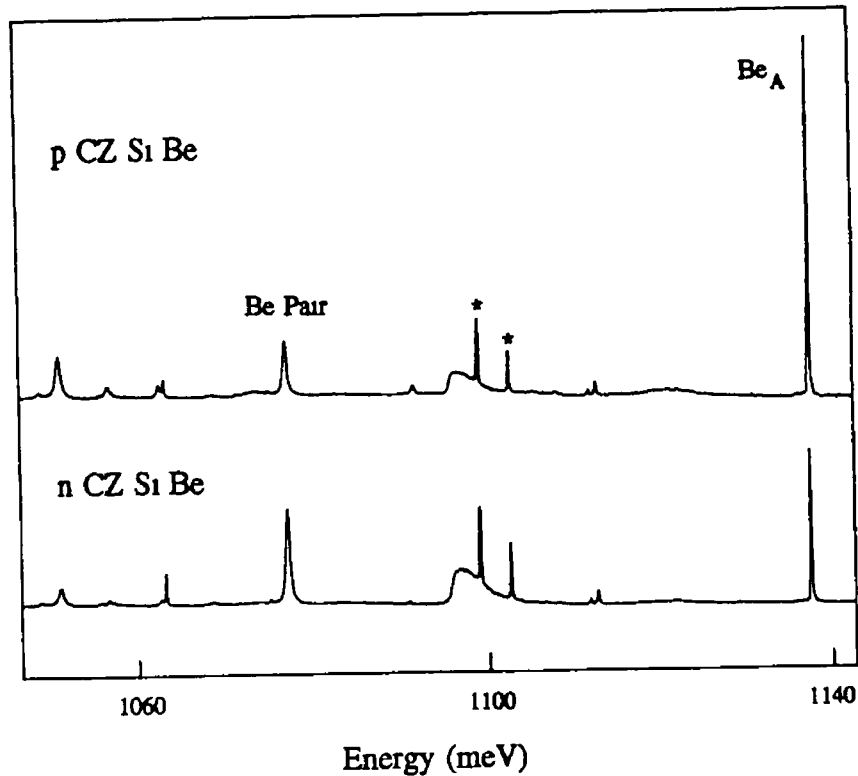
Figure 5 9   PL spectra of $Be_A$ defect comparing n and p type material

electron, thus completing the bound exciton process   We can conclude that although the $Be_A$ defect does not appear to incorporate either B or P, it is favoured in p-type material indicating that the defect is likely to be a hole-attractive isoelectronic centre

## 5.7 Damage Related Products

During the implantation process the silicon crystal is subjected to a considerable amount of radiation damage as the energetic ions penetrate a shallow region beneath the surface   The depth and distribution of the implanted ions will depend on the energy, dose and identity of the incident particle   On entering the crystal the implanted ion will have an energy E, on impact with a lattice atom a proportion of this energy will be transferred to the lattice atom which may leave it's site with a finite energy   This energy will be dissipated through collisions with other lattice atoms   The implanted ion will continue to impact with lattice atoms until all of its initial kinetic energy is dissipated, whereupon it comes to rest in the lattice structure   The average distance travelled by the ion before coming to rest is the range, an estimate of the range is

equivalent to the average penetration depth of the ions into the crystal  Interstitial atoms such as those created during the implantation process are generally referred to as damage products  Damage products such as silicon self interstitials and carbon interstitial atoms will be produced in the damage region  Silicon self interstitials are highly mobile at room temperature, while carbon interstitial atoms are highly mobile at $T > RT$ with a diffusion rate considerably exceeding that of a carbon substitutional atom [5]  These damage products are available for complexing with other impurities present and with the impurity introduced via implantation

A number of experiments were conducted to determine the extent to which damage products play a role in the formation kinetics of the Be defect  Samples 19, 20 and 21 all received a dose of 1e15 atoms/cm$^2$ but with various implantation energies The implantation energy will determine the depth to which the implanted ions penetrate and will also effect the extent of damage in the crystal because each ion will transfer a fraction of its energy during each collision to an atom of the crystal, a process which continues until all energy is transferred and the implanted ion comes to rest  Table 5 4 lists the average penetration depth at each implantation energy together with the stopping cross section which is an estimate of the energy lost by the ion per Å

| Implantation Energy | Penetration Depth (Approx) | Stopping Cross Section | Concentration |
|---|---|---|---|
| 50 keV | 1730 Å | 22 eV/Å | 5 7x10$^{19}$ cm$^3$ |
| 100 keV | 3440 Å | 25 eV/Å | 2 9x10$^{19}$ cm$^3$ |
| 200 keV | 6360 Å | 33 eV/Å | 1 6x10$^{19}$ cm$^{-3}$ |

*Table 5 3  Implantation characteristics for silicon implanted silicon  In all cases the implanted dose was 1 x 10$^{15}$ atoms/cm$^2$  (The calculated values were obtained using "TRIM" a PC based tool "the TRansport of Ions in Matter", the method employed in the program is described in reference [6])*

The PL spectra obtained from the samples implanted with energies as outlined above are illustrated in figure 5 10  The inset in this figure compares the increase in luminescence intensity of this defect with that of the Be pair luminescence, also observed in these samples, as a function of implantation energy  In the case of the Be$_A$ defect there is an
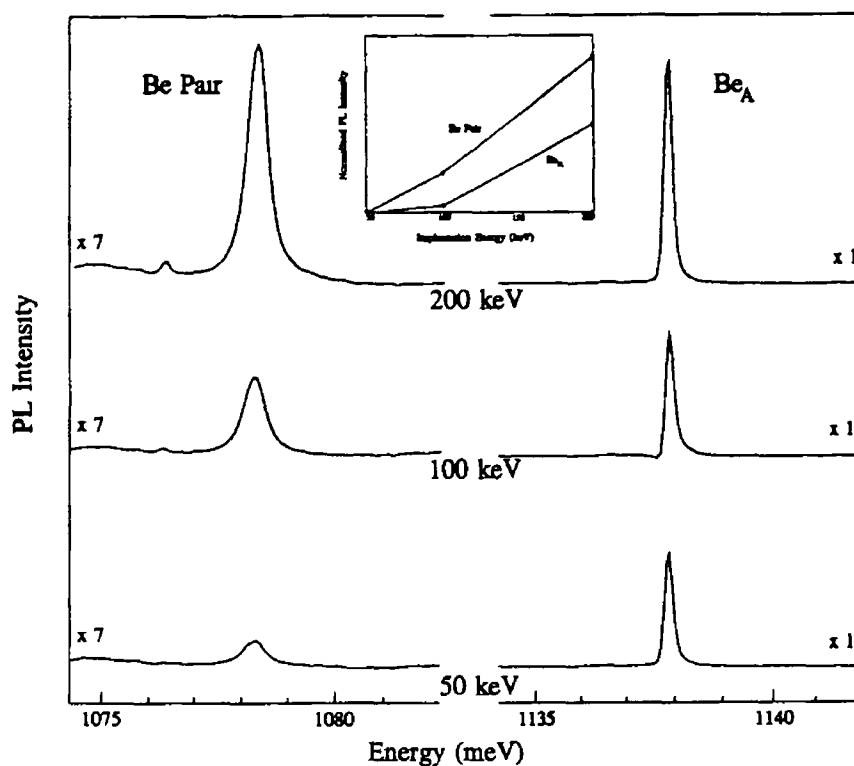
*Figure 5 10  PL spectra comparing the effect of implantation energy on defect production*

increase of a factor of ~ 2 over the implantation energy range investigated, whereas the Be-pair luminescence increases by a factor of ~ 10 over the same range  The dose
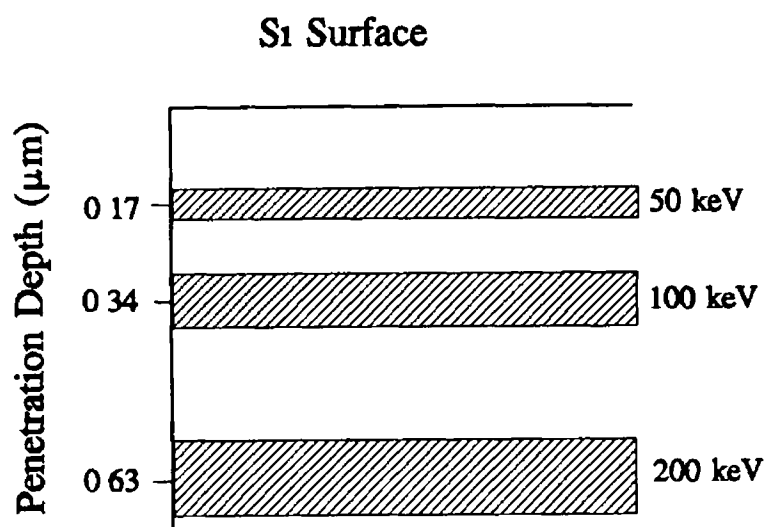


*Figure 5 11  Schematic representation of penetration depth of Be ions in Si with implantation energies of 50, 100 and 200 keV*

received by all samples was equivalent ($1 \times 10^{15}$ Be atoms/cm$^2$ )   On this basis the concentration of Be atoms in the implanted region, after implantation, can be estimated Column four of table 5 4 contains the estimated concentration values   The effects of annealing are twofold   Firstly, a uniform distribution of the implanted ion throughout a layer the sample material is expected due to the high diffusivity   Secondly, a proportion of the implanted ions will also out diffuse from the sample surface during the annealing procedure   In the case of the sample implanted with an energy of 50 keV the proportion of out-diffused ions is likely to be higher than in the case of the 200 keV sample as the implanted ions are concentrated in a narrow band close to the sample surface as illustrated in figure 5 11   The concentration of Be ions in the sample after annealing can therefore be expected to be higher in the case of the 200 keV sample The spectra of figure 5 10 correlate with this result as they show an increase in luminescence intensity for both the $Be_A$ and Be-pair defects as a function of implantation energy   The Be-pair defect incorporates two Be atoms, and, as outlined above, increases in intensity at a higher rate than the $Be_A$ defect as a function of increasing implantation energy (and so increasing concentration)   We can therefore conclude that the $Be_A$ defect must incorporate fewer Be atoms than the Be-pair defect due to its smaller intensity increase as a function of final Be concentration   The $Be_A$ defect is therefore assumed to incorporate one Be atom

A significant step towards understanding the role of damage and damage related products in the production of this defect is to distinguish between processes that are simply thermally induced by the annealing process and those that rely upon the breakup (or further complexing) of radiation damage defects that form at and above room temperatures but below the formation temperature of this defect   The most appropriate means of achieving this is to prepare samples by Be diffusion thus eliminating the introduction of damage products   However, Be is a highly toxic substance requiring extreme safety precautions when handled and for this reason only implanted samples were used   The following investigations were undertaken to partially address this problem

From table 5 4 the penetration depth of 200 keV $^9$Be ions, and so an estimate of the depth of the damage region, is calculated to be approximately 6300 Å   Damage and damage products resulting from the implantation process can be eliminated by etching the surface of the sample to a depth beyond the damage region   Figure 5 12 contains
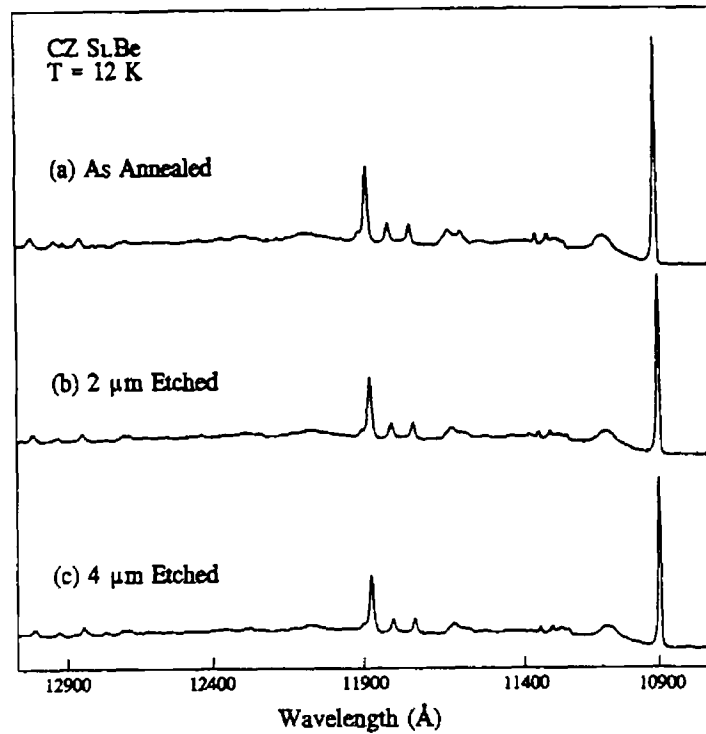
*Figure 5 12  (a) PL spectra of Si Be sample containing Be$_A$ (b) after removing 2 μm from surface and (c) after removing a further 2 μm*

three spectra, the first of which is from a sample with a strong PL signal associated with the Be$_A$ defect  This sample was subjected to an etching procedure (as described in section 4 6) which removed 2 μm from the surface  The spectrum obtained at this point is contained in figure 5 12(b)  The sample was then subjected to a second etch of a further 2 μm, the resulting spectrum is contained in figure 5 12(c)  The PL from this defect is clearly not confined to the surface layer where damage and damage products are abundant  The presence of the defect at ranges well beyond the damage region indicates that the presence of the Be ion is the crucial factor in the production of this defect rather than damage products

## 5.8 Local Vibrational Modes

The data presented above indicates that beryllium and oxygen are likely constituents of this defect and that damage related products are not necessary in order for this defect to form  In this section the characteristic local mode spectrum, also a

function of the chemical constituents of the defect, will be investigated

In all samples in which this defect was produced a characteristic local mode spectrum was observed A local mode which makes a contribution to the one phonon sideband will also appear in the multiphonon sidebands Hence, the two phonon replicas are also clearly observed In section 2 8 2 we saw that most local modes which arise in silicon are produced by a constituent atom of the defect vibrating about its equilibrium position Isotope shifts observed in the local modes indicate unambiguously the presence of a particular impurity in the defect Table 5 4 contains data on the local modes of a range of defects produced in silicon which display a shift in energy associated with the substitution of isotopes of particular impurities It is clear from this data that the phonon quantum ($\hbar\omega$) associated with the vibration of any single constituent of a defect can have any of a large range of values The N-C related defect referred to in table 5 4, for example, has a local mode at $\hbar\omega$ = 122 9 meV which is sensitive to both C and N isotope substitution The G line and P line both possess local modes which are attributed to the incorporation of C, however, the associated phonon quanta occur in the range 65 - 72 meV It is, therefore, not possible to predict the phonon quantum that will be associated with any given defect constituent, and conversely, in the absence of isotope studies the origin of the observed local modes of the $Be_A$ defect can not be determined

Circumstantial evidence presented in previous sections indicate that both Be and O are incorporated into this defect and so although the exact origin of each local mode can not be determined, it is reasonable to assume that they are associated with the vibration of the Be and O constituents of the defect. Using this information and the positions and strengths of the local modes, an estimate for the change in the silicon lattice parameter that is required to accommodate a Be-O complex can be determined For a local mode, the shift $Q_0$ in equilibrium position is given in terms of the reduced mass $\mu$ of the mode and its frequency $\omega$ by [7]

$$Q_0^2 = \frac{2\hbar\omega S}{\mu \omega^2}$$
5 4

where S is the Huang-Rhys factor for the mode The value of S may be obtained from the PL spectrum using the equation

| Line | ZPL Energy (meV) | Element | Phonon Quanta (meV) | Ref |
|---|---|---|---|---|
| | 745 6 | N | 122 9 | [8] |
| | | C | 122 9 | |
| C Line | 789 | O | 65 5 | [9] |
| | | O | 72 6 | |
| | | Si | 72 6 | |
| P Line | 767 | C | 72 0 | [10] |
| | | | 65 2 | |
| G Line | 969 | C | 71 9 | [11] |
| | | | 67 35 | |
| | 1080 | B | 109 4 | [12] |

*Table 5 4     Zero phonon lines energies and shifts from no-phonon lines for local modes attributed to various impurities*

$$S = \frac{I(localmode)}{I(zpl)} \qquad 5\,5$$

where I is the intensity ℏω for the local modes of the Be$_A$ defect are as listed in table 5 1 and an estimate of the Huang-Rhys factor for each local mode is

$$L_1 \approx 08 \qquad L_2 \approx 09 \qquad L_3 \approx 48 \qquad 5.6$$

If we consider the Be-O complex to contain one Be and one O atom then the reduced mass of this system is

$$\frac{1}{9} + \frac{1}{16} = \frac{1}{\mu} \qquad 5.7$$

giving $\mu$ = 5 76 a m u  Using equation 5 4, $Q_0$ for each of the three local modes is

$$Q_0(L_1) = 004\,nm \qquad Q_0(L_2) = 004\,nm \qquad Q_0(L_3) = 009\,nm \qquad 5.8$$

The average value of $Q_0$ is approximately 006 nm  This is equivalent to a change of 2 5 % of the Si lattice parameter in the presence of this defect  A deformation such as this extent sufficient to create a local strain field about the defect site which can be either electron or hole attractive  This value is large compared with the strains produced (< 2%) in a typical uniaxial stress experiment where shifts in the ZPL of 1-10 meV are typical [12]

## 5.9 Vibronic Sideband

Weakly bound excitons in silicon are characterised by vibronic sidebands which contain contributions mainly from the TA, LO and TO wavevector conserving phonons  Inspection of the sideband associated with the $Be_A$ defect, for example in figure 5 1, reveals that for this defect this is not the case  A strong phonon sideband is observed extending more than 200 meV from the ZPL, indicating that the defect undergoes considerable relaxation upon exciton recombination  The lattice relaxation therefore involves phonons from all parts of k-space, and not simply the wavevector conserving phonons

Recall from section 2 8 7, that annihilation of the exciton induces a relaxation of the defect within the lattice  The relaxation energy was defined as the difference between the zero phonon energy $E_{ZPL}$ and the energy $E_c$ of the centroid of the luminescence band

$$E_r = E_{ZPL} - E_c \qquad 5.9$$

A relaxation energy of approximately 100(5) meV is calculated by direct integration of the entire luminescence band (ignoring features unrelated to this defect e g FE luminescence) for this defect  In calculating this value, the luminescence band was corrected for system response  However it must be remembered that the resolution of the measurement can distort the observed luminescence intensity  The resolution used in this case was ~ 0 15 meV  $E_c$ values calculated from spectra with poorer resolution were found to be within 10 % of the value quoted here  Taking these limitations into

account, a broad range of phonons is clearly involved in the relaxation of the lattice in the vicinity of the defect after the exciton has recombined   The spectroscopic binding energy of this defect is just 31 52(5) meV   Clearly, the experimentally observed relaxation energy is a major contributor to the binding of the electron and hole to the defect centre

A characteristic feature of the vibronic sideband of this defect is the occurrence of the local modes, $L_1$, $L_2$ and $L_3$, observed in the sideband structure   Recall from section 2 9, that the local modes are also replicated in the two phonon region of the spectrum   Vibrational modes replicated in the two phonon sideband arise due to any combination of phonons from the one phonon sideband which combine to form the two phonon sideband   The two phonon region can therefore be constructed from the one phonon region according to equation

$$P_n(\omega) \sim \int P_{n-1}(\omega - x) P_1(x) dx \qquad\qquad 5.10$$
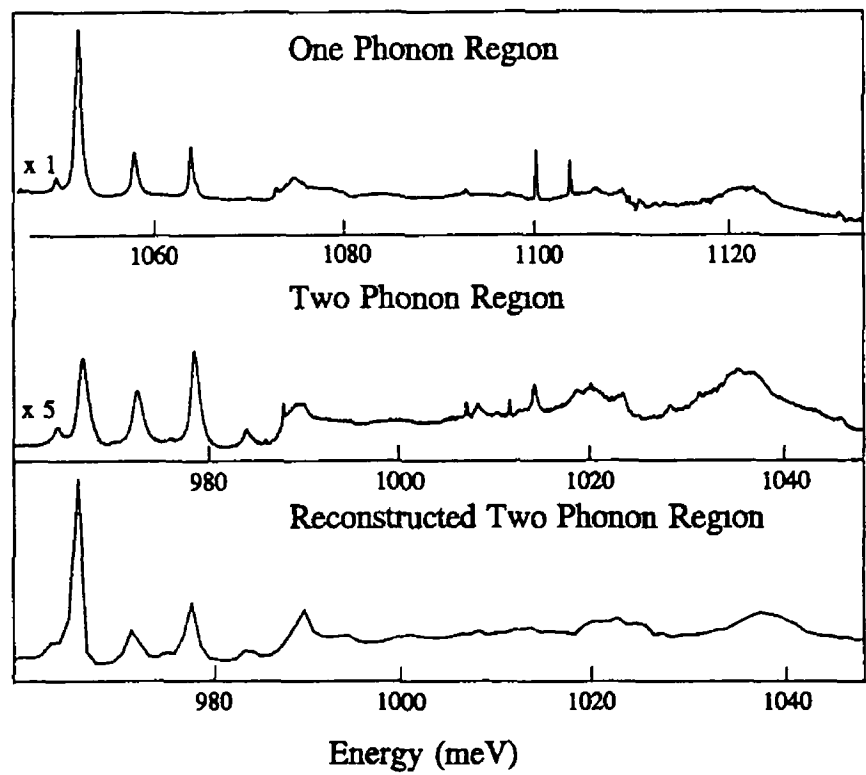


*Figure 5 13   The one and two phonon regions of the spectrum associated with the $Be_A$ defect are depicted together with the reconstructed two phonon region*

where the integral runs over all the mode frequencies, x   The top panel of figure 5 13

contains the one phonon region of the spectrum and the second panel contains the two phonon region of the spectrum    The two phonon region was reconstructed using equation 5 10 and is illustrated in the bottom panel of figure 5 13   The curve in the figure contains the contributions from the one, two and three phonon sidebands in this region    The reconstruction predicts that the relative intensities of the three local modes should approximate the intensities observed in the one phonon region of the spectrum    As yet, a reason for the observed behaviour has not been deduced

## 5.10 Conclusions

In this chapter the results of a comprehensive set of experiments were presented which provide circumstantial evidence for the chemical constituents of a defect produced in Be implanted silicon   Optimum defect production is achieved by annealing at 600°C    An estimation for the activation energy of defect formation is of the order of 2 75 eV   After annealing, a slow cool was necessary to optimise the defect concentration   This is reminiscent of the Be related acceptor level at 191 9 meV above the valence band which was discussed in section 1 5 - optimum formation conditions for this level were achieved by allowing the sample to cool slowly after annealing, Crouch et al [13] suggest that during cooling Be complexes dissociate to substitutional sites

Production of this defect is favoured in oxygen rich silicon which is indicative of the involvement of oxygen in the defect   Substitutional Be would be expected to form a double acceptor and interstitial Be a double donor, however a molecule involving Be and O will be electrically neutral and will have no excess carriers in the silicon lattice    The resulting defect would therefore be isoelectronic in nature, with the luminescence occurring as the result the recombination of an exciton bound to the defect.   The exciton would be bound to the defect by firstly trapping a charge carrier, electron or hole, by virtue of a defect induced strain field, the second carrier then being captured due to a Coulombic attraction   A change in the lattice constant of the order of 2 5 % was calculated for a Be-O complex, this induces a local strain field in the crystal which makes it attractive to a charge carrier

It is clear that the information presented above concerning the chemical constituents of the defect is circumstantial   The use of isotope studies would confirm

the actual defect constituents, however, as Be has only one stable isotope confirmation of the involvement Be cannot be concluded in the usual manner  In chapter seven a feasibility study on a new technique involving the use of radioactive isotopes as a means of confirming a defect constituent will be presented

The vibrational sideband associated with the defect was considered  The spectrum contained phonons from all regions of k space rather than simply the momentum conserving lattice modes  The centroid of the vibrational band was calculated to be of the order of 100 meV from the ZPL

In the next chapter the nature of the photoluminescence spectrum associated with this defect as a function of applied perturbations in the form of temperature, uniaxial stresses and magnetic fields will be studied in detail in an attempt to further characterise this defect  The isoelectronic nature of the defect will be confirmed and the symmetry associated with it will be established

**References**

[1]     N N Gerasimenko, B A Zaltsev, L N Safronov and L S Smirnov, Sov Phys Semicond 19(7) (1985) 762

[2]     K W Boer, in Survey of Semiconductor Physics - Electrons and Other Particles in Bulk Semiconductors (Van Nostrand Reinhold, 1990)

[3]     O O Awadelkarim, H Weman, B G Svensson and J L Lindstrom, J Appl Phys 60 (1986) 1974

[4]     M O Henry, E C Lightowlers, N Killoran, D J Dunstan, B C Cavenett J Phys C 14 (1981) L255

[5]     G Davies, E C Lightowlers, R C Newman, A S Oates A model for radiation damage effects in carbon doped crystalline silicon

[6]     J F Ziegler, J P Bersack and U Littmark The Stopping and Range of Ions in Matter (Pergamon Press, New York 1985)

[7]     G Davies, Physics reports 3&4 (1989) 83

[8]     A Dornen, G Pensl and R Sauer, Phys Rev B 35 (1987) 9318

[9]     G Davies, E C Lightowlers, R A Woolley, R C Newman and A S Oates, J Phys C 17 (1984) L499

[10]    W Kurner, R Sauer, A Dornen and K Thonke, Phys Rev B 39 (1989) 13327

[11]    G Davies, E C Lightowlers and M C do Carmo J Phys C 16 (1983) 5503

[12]    E Irion, K Thonke and R Sauer, J Phys C 18 (1985) 5069

[13]    R K Crouch and J B Robertson, Phys Rev B, 5 (1972) 3111

# Chapter 6

## Analysis of 1137.98 meV Be Related Defect

## 6.1 Introduction

In the previous chapter we identified a vibronic system in Be implanted silicon and the chemical nature of the defect was discussed In this chapter we further investigate this defect by examining the spectral response to temperature, uniaxial stress and magnetic fields

## 6.2 Temperature Controlled Experiments
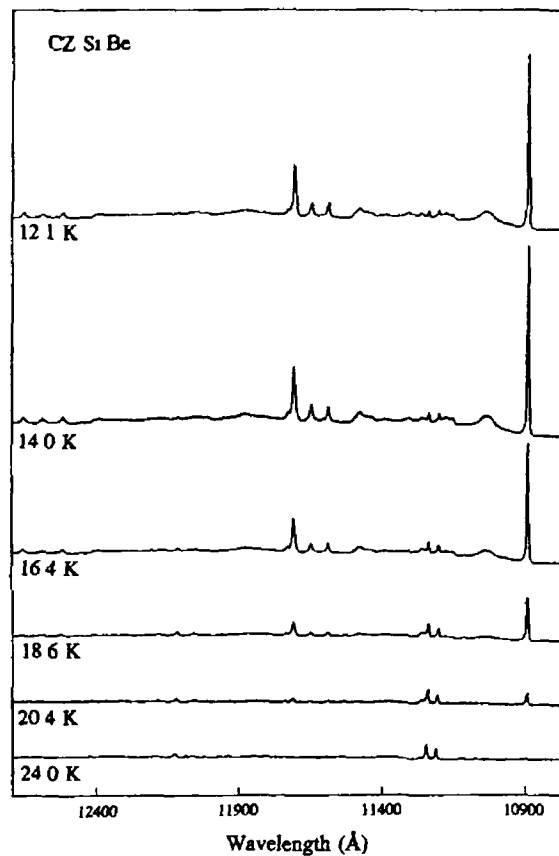


*Figure 6 1 Representative PL spectra over temperature range 8 - 25 K.*

The photoluminescence spectrum was monitored as a function of sample temperature and was found to be highly sensitive to temperature below 25 K, at which point the intensity was negligible Representative spectra over the range 8 - 25 K are illustrated in figure 6 1 The luminescence intensity as a function of temperature of the
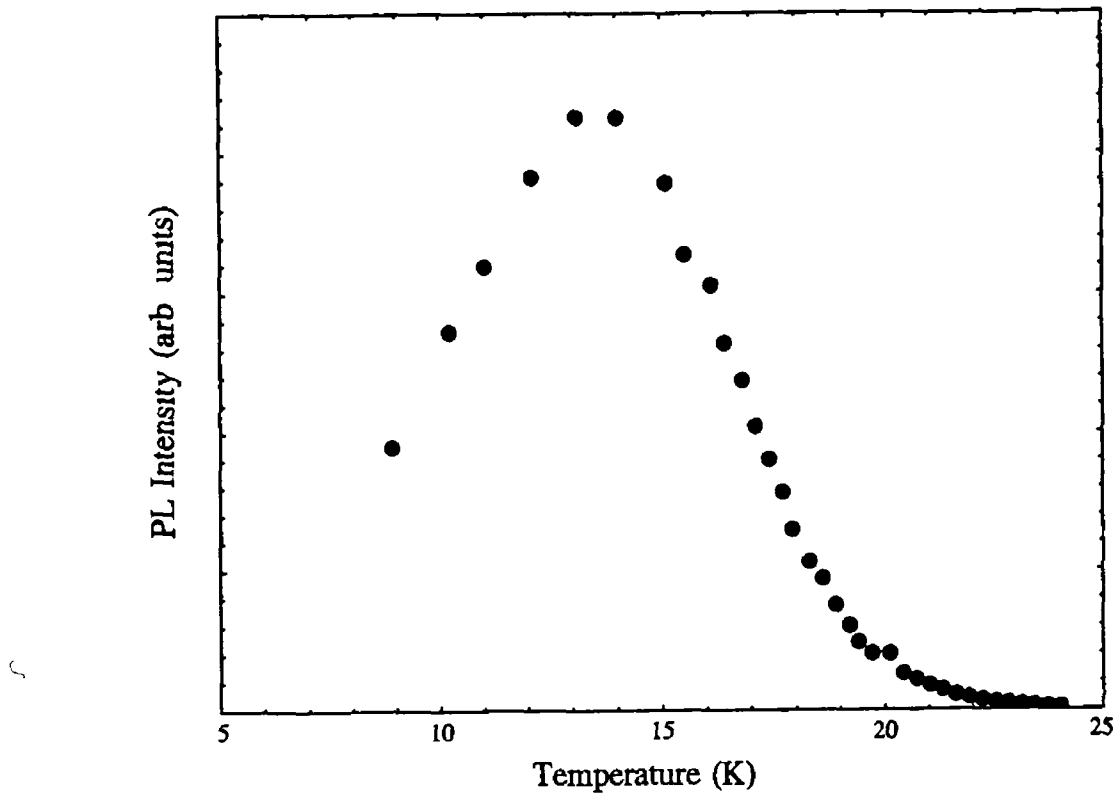


Figure 6 2 Photoluminescence intensity for the $Be_A$ defect as a function of temperature

zero phonon line of the system is illustrated in figure 6 2 At temperatures up to about 13 K the luminescence intensity increases, consistent with shallower exciton traps being depopulated Identification of these traps is difficult and the range of shallow traps present from sample to sample may differ As an example, the binding energy of an exciton at a boron acceptor is just 3 8 meV while that of a phosphorous donor is 4 7 meV These levels along with others with binding energies less than the binding energy of the defect of interest are all possible shallow traps which may contribute to the increase in intensity

At approximately 13 K the intensity reaches a maximum and thereafter gradually decreases to a negligible value at 25 K due to the thermal dissociation of the carriers

from the defect This is characteristic of an exciton bound to a defect where there is a rapid increase in the probability of thermal ionisation as a function of increasing temperature In section 3 2 the temperature dependence of the decay in luminescence intensity was given by

$$I(T) = \frac{I(0)}{1 + GT^{\frac{3}{2}} \exp\left(-\frac{E_t}{kT}\right)} \qquad 6.1$$

where the $GT^{3/2}$ term describes the temperature dependence of the density of band states relative to the band states G and $E_t$ is the dissociation energy of the bound complex Rearranging equation 6 1 and neglecting the $T^{3/2}$ term we obtain

$$\frac{I(0)}{I(T)} = 1 + G\exp\left(-\frac{E_t}{kT}\right) \qquad 6.2$$

and

$$\ln\left(\frac{I(0)}{I(T)} - 1\right) = \ln G - \frac{E_t}{kT} \qquad 6.3$$

(The $T^{3/2}$ term is assumed constant in comparison to the other terms over the narrow temperature range of interest, 13 - 24 K) Plotting ln (I(0)/I(T) - 1) against 1/T yields a slope of $-E_t/k$ The intensity data for $Be_A$ have been plotted in this manner in figure 10 3 Neglecting the $T^{3/2}$ term, an ionisation energy of 25 4(3) meV is obtained for $E_t$ To account for the $T^{3/2}$ term in equation 6 3 the quantity 3/2 ln T should be added to the right hand side of equation 6 3 This procedure was followed for the low and high temperature limits of figure 6 3 in order to correct for the $T^{3/2}$ term The dashed line in figure 6 3 represents the corrected fit The corrected ionisation energy, calculated from the slope of the dashed line in figure 10 3, is 27 2(3) meV If we assume the defect to be isoelectronic in nature, then the total binding energy of the electron-hole complex to the defect can be calculated from the energy gap of silicon (1169 5 meV, at low temperatures) and the position of the ZPL (~ 1138 meV), i e ~ 31 5 meV The calculated value of $E_t$ of 27 2(3) meV accounts for most of this energy, which in the pseudo-donor model implies that the binding energy of the primary particle to the defect is only of the order of 4 2(3) meV The observed behaviour can be explained by
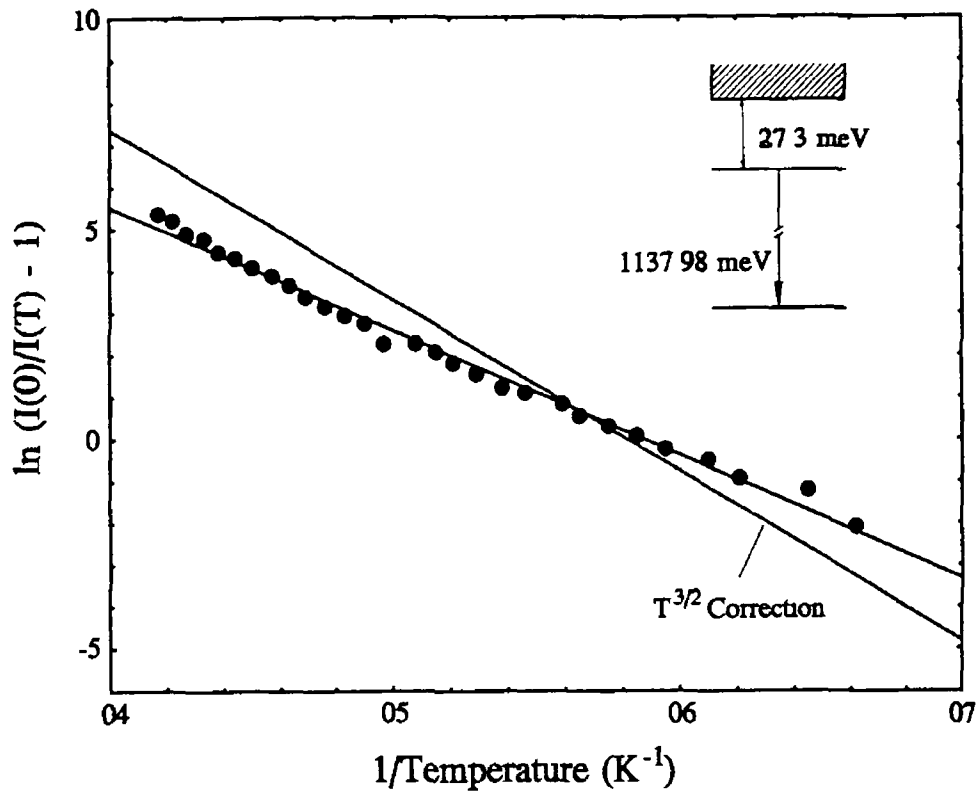
*Figure 6 3   Ln (I(0)/I(t)-1) vs 1/T, the dashed line indicates the corrected fit associated with $T^{3/2}$ assumed constant over the temperature range*

considering the ionisation process to involve the simultaneous loss of the electron-hole pair from the defect in the form of an exciton rather than the sequential release of the loosely bound particle followed by the tightly bound particle   Ionisation from other shallow isoelectronic pseudo-donor and pseudo-acceptor defects behave in this way, for example, the "ABC" centre in silicon which is electron attractive [1] and the $Zn_A$ defect in silicon which is hole attractive

In the case of $Be_A$ the measured ionisation energy of the exciton accounts for ~ 87 % of the measured spectroscopic energy   The extensive relaxation by the defect that is evident on recombination, as discussed in the previous chapter, could contribute to the ionisation process   Also, as the temperature is increased, the phonon population increases and may also contribute to the ionisation of excitons from the $Be_A$ defect

In conclusion, the temperature dependence of the luminescence associated with $Be_A$ is characteristic of pseudo-donor and pseudo-acceptor defects in silicon   The dissociation energy of the bound complex was found to be 27 3(3) meV   The ionisation process is believed to consist of the simultaneous dissociation of the electron and hole

pair as an exciton

## 6.3 Uniaxial Stress Data

Oriented samples were prepared as outlined in section 4 6, in such a manner as to ensure a strong luminescence signal associated with the 1137 98 meV line and it's associated side band structure. Samples were aligned within the stress rig such that stress could be applied in turn along the <001>, <111> and <110> directions

Uniaxial stress measurements are particularly susceptible to errors in the form of spurious lines and stress components which become broadened with increasing applied stress. These can be attributed to two sources, firstly, the misalignment of the sample within the stress rig and secondly, the misorientation of samples when cut from the silicon ingot. Care was taken with sample alignment in order to minimise the former as a source of error. No control was possible, however, over the as-received sample orientation. The experiments were repeated to check repeatability. The measurements involved using both the dispersive system and the Fourier transform spectrometer as outlined in section 4 3. Two sets of data are presented in figure 6 4 in the form of fan-diagrams, obtained by determining the positions of each stress split component as a function of applied stress when a uniaxial stress was applied in turn along <001>, <111> and <110> axes of the samples. Figure 6 4(a) is based on data obtained from the dispersive instrument and figure 6 4(b) contains data obtained from the Fourier transform instrument where a resolution of approximately 0 12 meV was possible compared to approximately 0 25 meV on the dispersive instrument. Significant differences are evident, most notably the detection of extra components in the higher resolution data obtained using the FT instrument. These discrepancies between the two sets of data (a) and (b) were analysed in detail. The following are the principal factors which emerged in the analysis. Firstly, the reproducibility of the data recorded for increasing and decreasing stress was superior in case (a), this casts doubt on the accuracy of the data in case (b). Secondly, the extra components apparent under <111> stress in case (b) should have been detected in case (a) with the resolution available. The extra detail observed under <111> stress in case (b) is considered to be spurious and arises from a small misalignment of the sample. For the case of <100> stresses, the
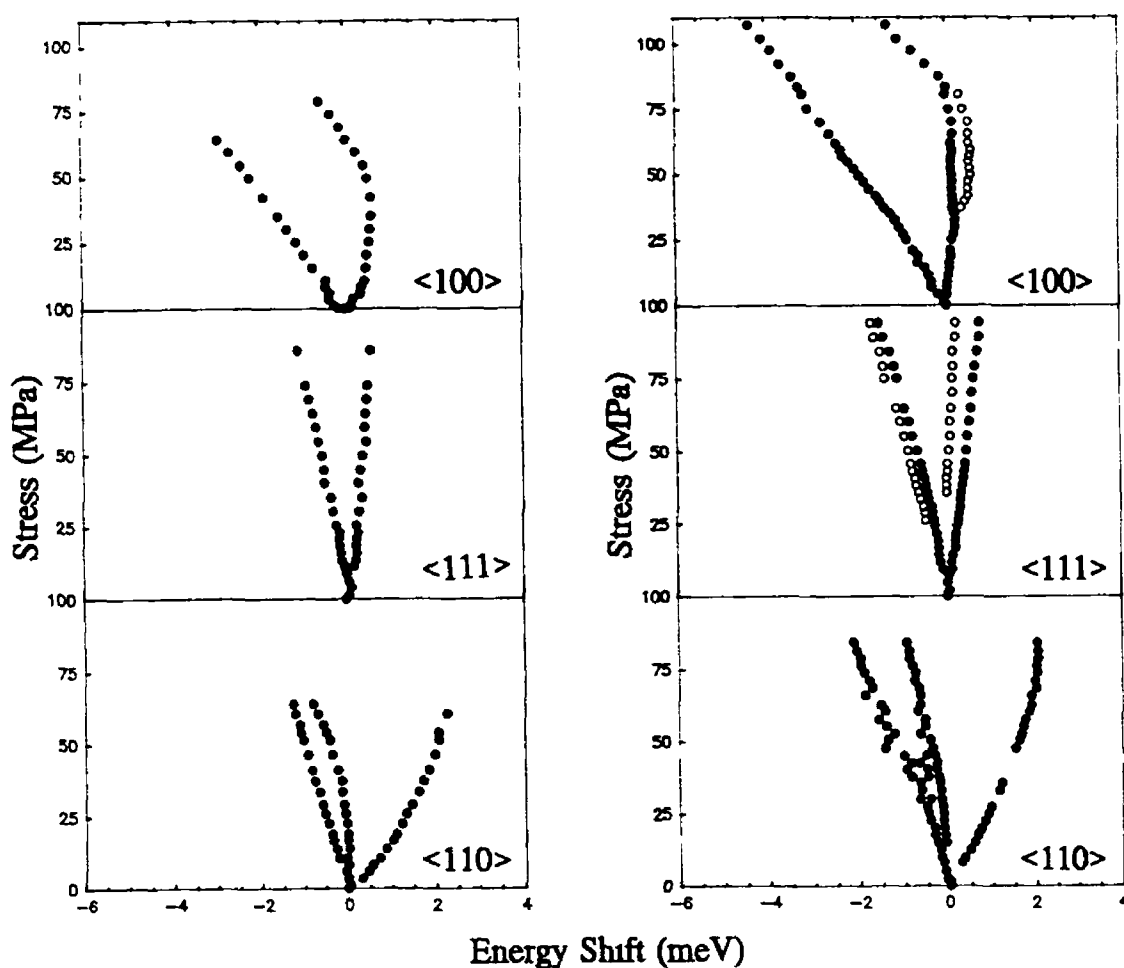
*Figure 6 4   Fan diagrams for uniaxial stress of the $Be_A$ defect as obtained using (a) dispersive instrument and (b) higher resolution Fourier transform instrument*

situation is not as simple   Here, the extra component observed in case (b) becomes evident as the stress split component begins to experience interaction effects and the extra component observed may be real   The differences between the data sets (a) and (b) for <110> stresses are not as striking as for the other two stress directions   A factor that must be considered here is that the sample used to produce the <110> data required polishing in order to produce a pair of parallel faces  - a process the other samples did not require as they were accurately cut in their as received state   Fortunately the <110> stress data are not essential for obtaining values for the stress parameters as will become evident below   Taken as a whole, and at low stresses, the two sets of data show very satisfactory reproducibility   This is maintained reasonably well also at high stresses except for the additional components observed under <111> stress   Accordingly, the set of data in figure 6 4(b) is analysed for the low stress regime where the extra resolution

provided somewhat better detail   For a global fit of theory to experiment aver the full range of stresses we use the set of data in figure 6 4(a)

Figures 6 5, 6 6 and 6 7 contain representative spectra obtained (using the dispersive instrument) for each of the three oriented samples as a function of applied stress
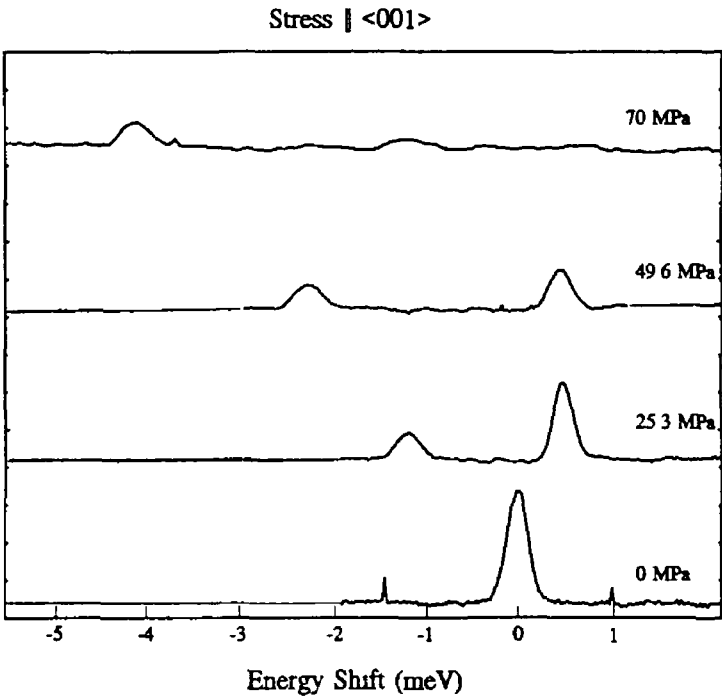
Stress ‖ <001>



Energy Shift (meV)

*Figure 6 5   Response of ZPL of Be_A defect to <001> stress*

Two components are clearly observed under <001> and <111> stresses and three under <110> stress   Table 3 1 lists the numbers of stress split components expected for the splittings of no-phonon lines under uniaxial stress for various transitions belonging to the eight possible symmetry systems of a cubic crystal   Comparing the present data with table 3 1, it can be seen that the observed splittings are consistent with the removal of orientational degeneracy at a defect of rhombic I symmetry imbedded in a cubic lattice   The point group of such a defect is $C_{2v}$, consisting of a twofold axis along a <001> or equivalent axis and two reflection planes whose normals are perpendicular to that axis and lie along the <110> and <1$\bar{1}$0> or equivalent axes, as illustrated in figure 3 7   The analysis that follows confirms this assignment through the determination of the stress parameters associated with a rhombic I centre and demonstrates the self-consistency of these results
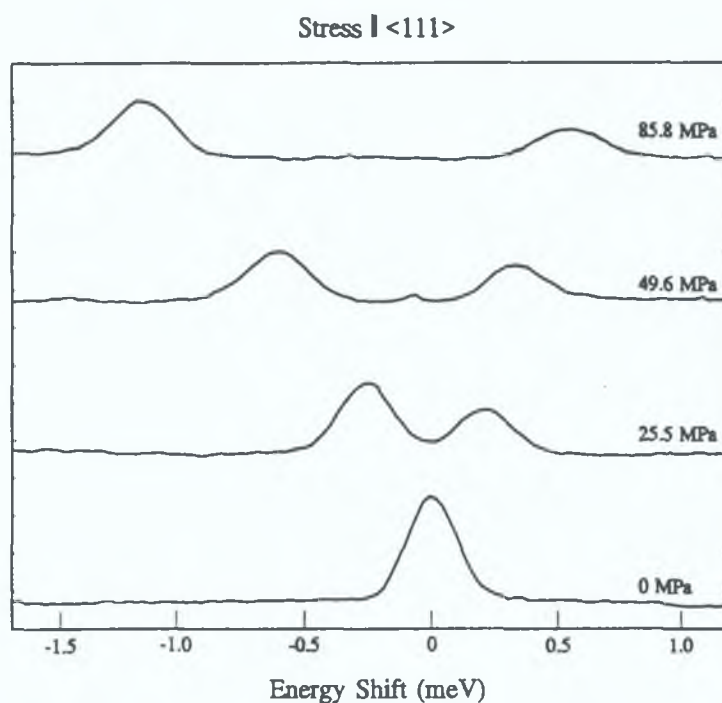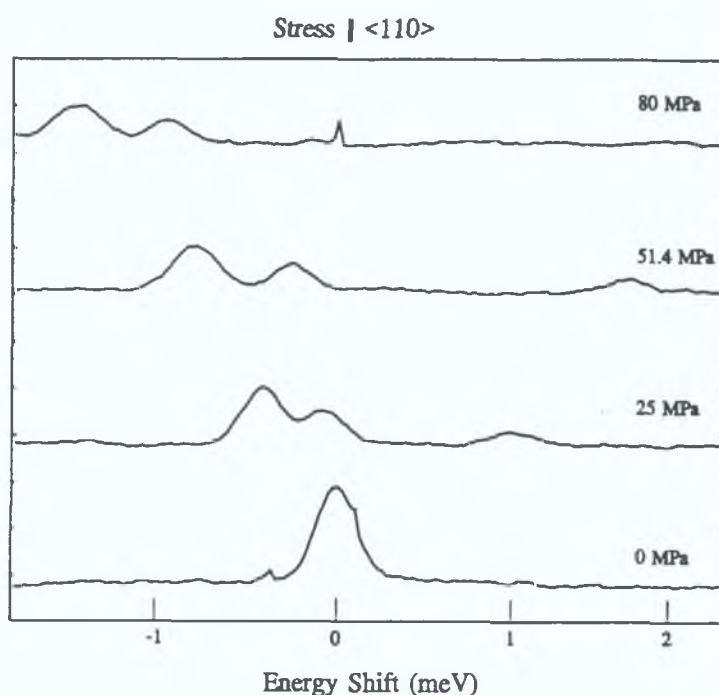
Figure 6.6  Response of ZPL of $Be_A$ defect to <111> stress.



Figure 6.7  Response of ZPL of $Be_A$ defect to <110> stress.

The most striking feature of this data is the strong interaction observed in the high energy component of the <001> data at stresses above ~ 60 MPa, which manifests

itself as a nonlinear shift rate. Interaction is also observed in the highest energy component of the <110> data while under <111> stresses no interaction is observed. This is indicative of the existence of an excited state of the system with transitions to the ground state not observed at the experimental temperature of 12 K due to the low thermal population of the upper state; in the absence of a perturbation such as uniaxial stress this level is not observed. Two stress regimes are identified. At low stresses, the response of the components is essentially linear whereas in the high stress regime the non-linear nature of the data dominates. In the first instance the data will be analysed in the low stress regime; the analysis will then be extended to account for the non-linear effects at higher stresses.

### 6.3.1 Low stress regime

In section 3.3, the shift rates for each of the stress split components, together with the expected intensities of each component for a rhombic I defect were derived, and they are summarised in table 6.1. Orientational degeneracies alone are responsible for the splitting at rhombic I defects as a function of stress. The transition therefore occurs between two A (or B) states or between an A and a B state.

| Stress Axis | Shift Rate Equations | Relative Intensities |
|---|---|---|
| [001] | $A_1$ | 2 |
| [100] | $A_2$ | 4 |
| [111] | $(A_1+2A_2+2A_3)/3$ | 3 |
| [$\bar{1}11$] | $(A_1+2A_2-2A_3)/3$ | 3 |
| [110] | $A_2+A_3$ | 1 |
| [$1\bar{1}0$] | $(A_1+A_2)/2$ | 4 |
| [011] | $A_2-A_3$ | 1 |

*Table 6.1    Summary of results for a transition at a Rhombic I centre in a cubic crystal. The notation used is consistent with that of Kaplyanski [2,3].*

Considering the low stress regime, it is trivial to determine the three stress parameters $A_1$, $A_2$ and $A_3$, by simply obtaining a linear least squares fit for each component of the
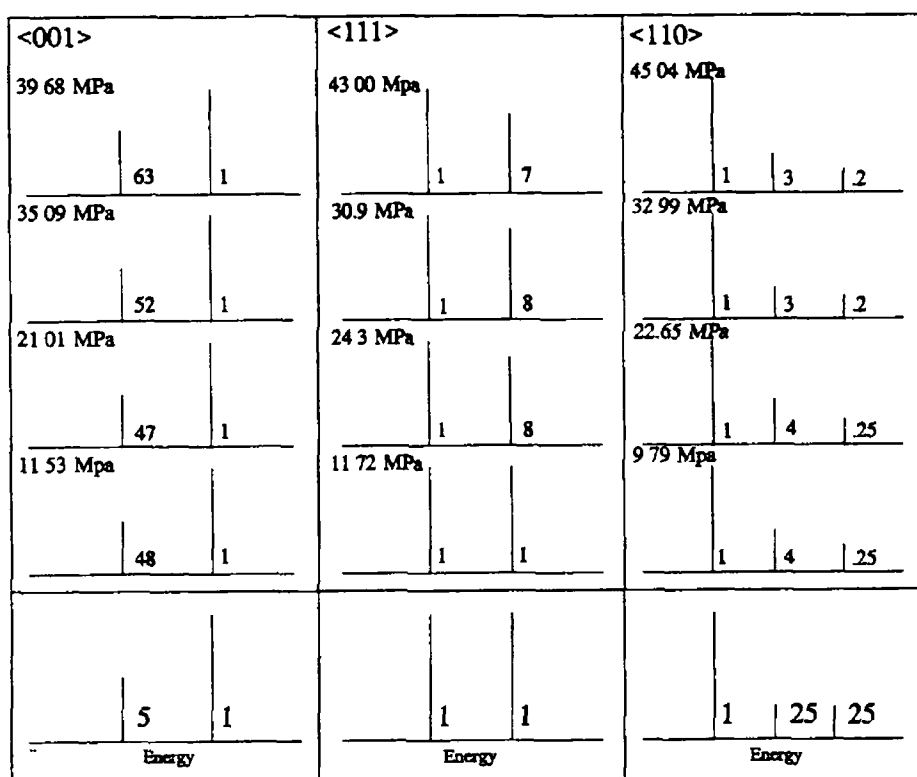
<001>

39 68 MPa

| 63 | 1 |

35 09 MPa

| 52 | 1 |

21 01 MPa

| 47 | 1 |

11 53 Mpa

| 48 | 1 |

| 5 | 1 |

Energy

<111>

43 00 Mpa

| 1 | 7 |

30.9 MPa

| 1 | 8 |

24 3 MPa

| 1 | 8 |

11 72 MPa

| 1 | 1 |

| 1 | 1 |

Energy

<110>

45 04 MPa

| 1 | 3 | .2 |

32 99 MPa

| 1 | 3 | .2 |

22.65 MPa

| 1 | 4 | .25 |

9 79 Mpa

| 1 | 4 | .25 |

| 1 | 25 | 25 |

Energy

*Figure 6 8   Schematic representation of the observed intensities of the stress split components as a function of stress*

stress vs energy data, and by considering the relative intensities of each component. Each of the six defect orientations will be associated with a stress split component of the data, hence expected relative intensities can be determined (cf section 3 3) These values should be reflected in the relative intensities of the PL sub-components Figure 6 8 shows schematically the observed intensities for stress applied along each of the principal axes for a range of stress values in the low stress regime For comparison, the bottom panel of this figure shows the expected intensities The intensity ratios of the subcomponents of a line will be stress independent when only orientational degeneracy is removed, as in the case of rhombic I symmetry Examination of the intensities of the stress split components shows very good agreement with the expected intensities Significant deviations are observed only for <100> stresses of ~ 40 MPa (where interaction effects are present) and for similar stresses along <110> In all other cases

agreement is excellent

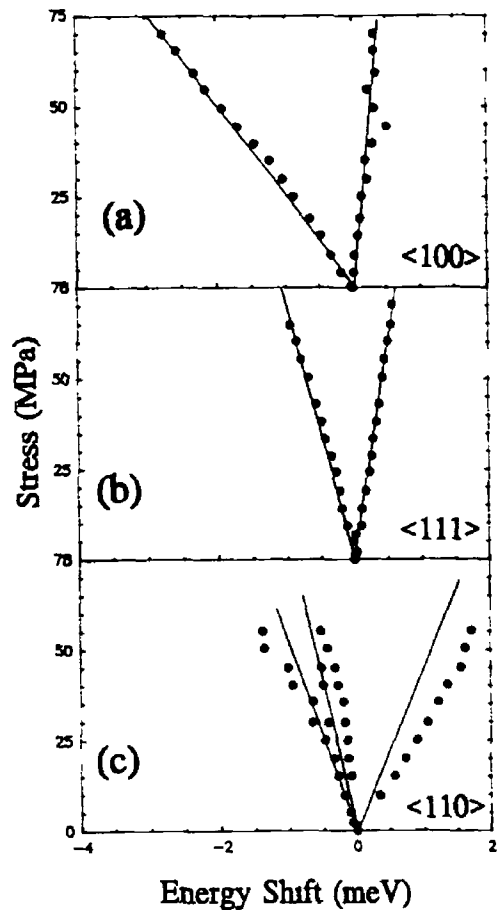## 6.3.1.1 Stress along <001>



Figure 6 9   Fan diagrams for $Be_A$ defect in low stress regime

A linear least squares fit to the <001> data, in the low stress regime, is represented by the solid lines in figure 6 9(a)   Shift rates of -40 0(4) and 7 4(7) meV/GPa are obtained for the low and high energy components respectively   From table 6 1, it is clear that the stress parameters $A_1$ and $A_2$ correspond directly with the slopes obtained   It remains only to assign the appropriate slope to each parameter Considering figure 6 5, an intensity ratio of 2 1 is expected between the two components, the parameter $A_2$ corresponding to the most intense component, which in this case is the high energy component   We therefore assign $A_1$ and $A_2$ as follows,

$$A_1 = -40\,0(4) \qquad A_2 = 7\,4(7) \qquad (meV/GPa) \qquad\qquad 6.4$$

### 6.3.1.2 Stress along <111>

Under <111> stress, the measured shift rates of the components are -16 2(3) meV/GPa for the lower energy component and 8 1(3) meV/GPa for the higher energy component, as illustrated in figure 6 9(b) Knowing the values of $A_1$ and $A_2$ (section 6 3 1 1), it is trivial to calculate $A_3$ using the linear combination of the shift rate equations associated with the stress split components under <111> stress $A_3$ may be obtained from the expression

$$\delta_3 - \delta_4 = \frac{1}{3}(A_1 + 2A_2 + 2A_3) - \frac{1}{3}(A_1 + 2A_2 - 2A_3)$$

$$\delta_3 - \delta_4 = \frac{4}{3}A_3 \qquad\qquad 6.5$$

The stress parameter therefore has the value

$$A_3 = 18\,3(6)\,(meV/GPa) \qquad\qquad 6.6$$

### 6.3.1 3 Stress parallel to <110>

It only remains now to substitute these values into the shift rate equations for stress along the <110> direction and to compare the calculated values to the actual least squares fit values This provides a self-consistent check on the parameter assignments which helps to confirm the results The solid lines of figure 6 9(c) are those obtained using the $A_i$ values as outlined above It is clear that the fit, although not perfect, is very good at low stress values

### 6.3 2 High stress regime

By considering the low stress regime, it was possible to assign the defect symmetry rhombic I It is clear, however, that the values obtained for the stress parameters yield a set of linear shift rates, from which the data deviates in the high

stress regime, particularly under <001> stress   In this section we shall consider the existence of an excited state of the system which, due to the operating temperature, is not populated under zero stress

Transitions from an excited state to a ground state at a defect with a rhombic I ($C_{2v}$) symmetry group occur between levels which are electronically non-degenerate   In $C_{2v}$ symmetry transitions can occur between states which are both A or both B, in this case the polarised intensity ratios illustrated in figure 6 10(a) would be expected for the stress split components [4]   Transitions can also occur occur between A and B states, in this case the polarised intensity ratios illustrated in figure 6 10(b) would be expected [4]   Figure 6 11 contains the polarised photoluminescence spectra at a representative



| Stress ‖ | <001> | <111> | <110> |
|---|---|---|---|
| A <> A |  1 \| 0 |  1 \| 1 |  0  2 \| 0   π |
| B <> B |  0  1 \| |  1  1 \| |  0  2 \| 0   σ* |
| A <> B |  0  2 \|   1 \| 1 |  4 \| 0   1 \| 3 |  1 1 \| 0   π    0 1 \| 1   σ* |

* parllel <1̄10> direction

*Figure 6 10   Expected polarised intensities of stress split components for defects with rhombic I symmetry   (a) A ↔ A, B ↔ B, and (b) A ↔ B transitions*

low stress value in each stress direction   Multiple internal scatter tends to depolarise the luminescence light, making it difficult to obtain accurate polarisation information   Bearing this limitation in mind, examination of the polarised luminescence spectra as in figure 6 11 favours a transition between A and B states   It is concluded, therefore, that the ZPL consists of a transition from an A to a B state or vice versa   Referring to the $C_{2v}$ character table (table 3 2) four transitions are possible, $A_1 \leftrightarrow B_1$, $A_1 \leftrightarrow B_2$, $A_2 \leftrightarrow B_1$ or $A_2 \leftrightarrow B_2$, uniaxial stress cannot distinguish between these cases [5]   We
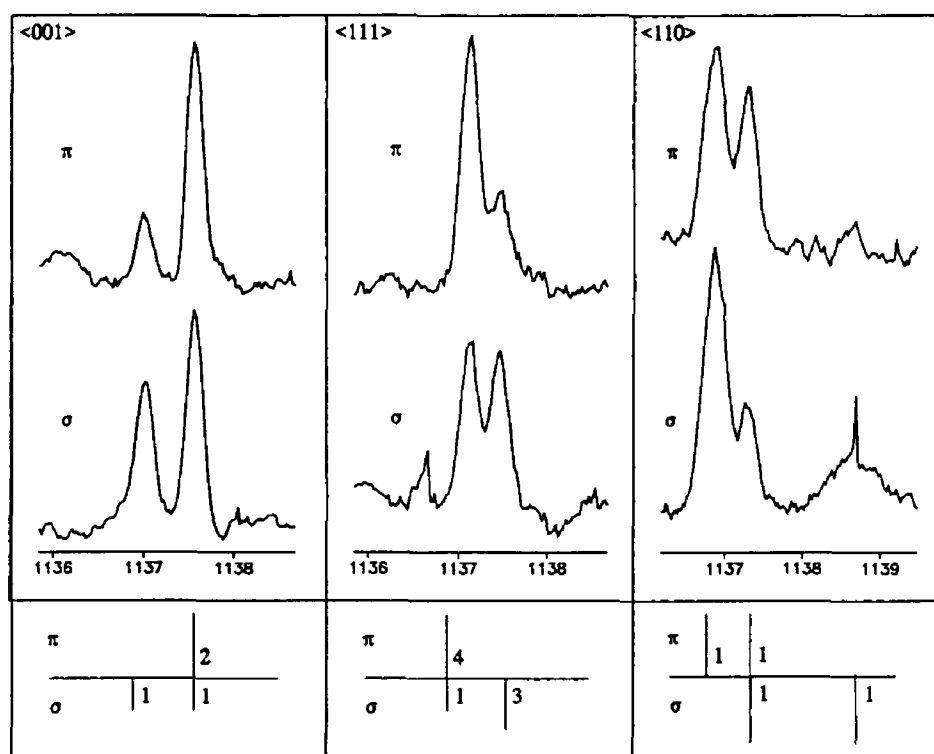
*Figure 6 11   Polarisation intensities of the stress split components for the $Be_A$ defect π and σ denote a polarisation axis parallel to and perpendicular to the applied stress, respectively*

will assume that the observed transition is $A_1 \leftrightarrow B_1$

In the high stress regime strong curvature is observed under <001> stress   In order to account for the observed nonlinearity we assume that an additional excited state of the system exists at a higher energy than the observed state   This assumption is based on the direction of the observed repulsion   The unseen state is also assumed to have a rhombic I symmetry   Based on the assumption that the observed transition is $A_1$ ↔ $B_1$ it is possible to determine the irreducible representation  of the interacting excited state   Let us further assume, for the present, that the ground state of the transition is $A_1$ and the upper state $B_1$   Figure 6 12 illustrates the four possible cases consistent with these assumptions

At zero stress, transitions from the upper excited state are negligible compared to the observed transition, but as the stress is increased the transition becomes
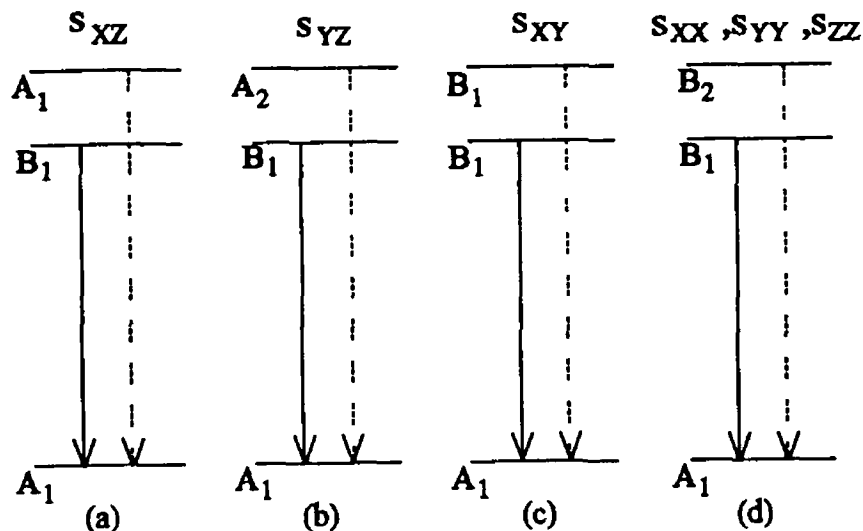
*Figure 6 12   Possible excited state structures for a $B_1 \leftrightarrow A_1$ transition at a rhombic I defect*

observable through the mixing of the $B_1$ and the unobserved level for a subset of the defects   The observed interactions provide the key to determining the irreducible representation of the unseen upper excited state   Interaction - in the form of a deviation from the linear shift rates - is observed under <001> and <110> stresses but not under <111> stress   Consider case (a) of figure 6 12   Examination of the $C_{2v}$ character table reveals that the only terms in the Hamiltonian which can mix $A_1$ and $B_1$ states are those which transform as $B_1$, i e only the $s_{XY}$ terms   Proceeding in this manner, it is possible to identify the $s_{ij}$ terms which are significant for each of the four cases listed above, the results of this analysis are presented in figure 6 12   In section 3 3, all of the $s_{ij}$ values for the six possible defect orientations in rhombic I symmetry were calculated according to equation 3 8 (table 3 4   contains the calculated values)   Inspection of table 3 4 reveals that the $s_{XY}$ tensor component is the only component which is non-zero for stress applied in the <001> and <110> directions and zero for <111> stresses   The $s_{XY}$ terms are reproduced in table 6 2 for each of the six defect centres

| Centre | X | Y | Z | Values of $s_{XY}$ for stress along | | |
|---|---|---|---|---|---|---|
| | | | | <001> | <111> | <110> |
| 1 | 110 | $\bar{1}$10 | 001 | 0 | 0 | 0 |
| 2 | $\bar{1}$10 | 110 | 00$\bar{1}$ | 0 | 0 | 0 |
| 3 | 011 | 0$\bar{1}$1 | 100 | ½ | 0 | -¼ |
| 4 | 01$\bar{1}$ | 0$\bar{1}$1 | $\bar{1}$00 | ½ | 0 | -¼ |
| 5 | 101 | 10$\bar{1}$ | 010 | -½ | 0 | ¼ |
| 6 | $\bar{1}$01 | $\bar{1}$0$\bar{1}$ | 0$\bar{1}$0 | -½ | 0 | ¼ |

*Table 6 2 Stress tensor components for each of the six rhombic I defect orientations*

We conclude that the upper excited is $B_2$ as the mixing of a $B_1$ and $B_2$ state is zero under <111> stress and non-zero under <001> and <110> stresses - as observed experimentally A secular matrix representing the interaction of a $B_1$ and a $B_2$ state is

$$\begin{bmatrix} <\Psi_{B_1}|\hat{V}|\Psi_{B_1}> & <\Psi_{B_1}|\hat{V}|\Psi_{B_2}> \\ <\Psi_{B_2}|\hat{V}|\Psi_{B_1}> & <\Psi_{B_2}|\hat{V}|\Psi_{B_2}>+\Delta \end{bmatrix} \qquad 6.7$$

where $\Delta$ is the energy difference between the two states in the unperturbed stress situation The perturbation $\hat{V}$ associated with a rhombic I defect was deduced in section 3 3, and was found to be

$$\hat{V} = A_1 s_{zz} + A_2 (s_{xx} + s_{yy}) + 2A_3 s_{xy} \qquad 6\ 8$$

The [1,1] and [2,2] elements of the secular matrix will therefore take this form The interaction term of the matrix has the stress tensor $s_{XY}$, as deduced above, however this is written in terms of the local defect co-ordinates To remain consistent with equation 6 8, the stress tensor must be transformed to crystal co-ordinates which is achieved using equation 3 18 The local stress tensor $s_{XY}$ transforms to

$$s_{XY} = \frac{1}{2}(s_{yy} - s_{xx}) \qquad 6.9$$

The stress operator for the interacting terms of the secular matrix in crystal co-ordinates therefore becomes

$$\hat{V} = W(s_{yy} - s_{xx})$$  6 10

The four elements of the interaction matrix are therefore

$$Element[1,1] \qquad A_1 + A_2(s_{xx} + s_{yy})A_3 + s_{xy}$$  6.11

$$Element[2,2] \qquad A_1' + A_2'(s_{xx} + s_{yy}) + A_3's_{xy} + \Delta$$  6 12

$$Elements[1,2],[2,1] \qquad W(s_{yy} + s_{xx})$$  6.13

Examination of the above matrix elements reveals eight adjustable parameters which may be varied in order to obtain an appropriate fit to the data As a first approximation the parameters associated with the observed state, $A_1$, $A_2$ and $A_3$, will be those calculated in the low stress regime From the data available, it is not possible to estimate values for the parameters associated with the unobserved state, A'$_1$, A'$_2$ and A'$_3$ and the interaction parameter, W The parameters contained in the interaction matrix were optimised by using the minimisation technique referred to in section 3 3

The parameters obtained using this method are listed in table 6 3 The solid lines on the fan diagrams of figure 6 13 correspond to the optimised fit values The fit obtained is in good agreement with the observed splitting of the ZPL of Be$_A$ The unseen excited state was assumed to have the same first order behaviour as for the observed state As no experimental data are, at present, available on the unseen state the stress parameters associated with it cannot be parameterised accurately However, the zero stress splitting of ~ 4 7 meV is consistent with a negligible intensity in the unseen state

| Be$_A$ (meV/GPa) | | Unseen Excited State (meV/GPa) | | Interaction Terms (meV/GPa) | |
|---|---|---|---|---|---|
| A$_1$ | -40 1 | A'$_1$ | -56 0 | W | 99 2 |
| A$_2$ | 11 0 | A'$_2$ | 1304 | | |
| A$_3$ | -19 5 | A'$_3$ | 1338 | | |
| Energy Separation of Excited States, $\Delta$ = 4 7 meV | | | | | |

*Table 6 3  Uniaxial stress parameters for the Be$_A$ zero phonon line   Column 2 contains parameters assigned to the interacting excited state which is calculated to be a distance of 4 7 meV away   Column 3 contains the interaction parameters   The shift rates calculated here are represented as solid lines in figure 6 13*
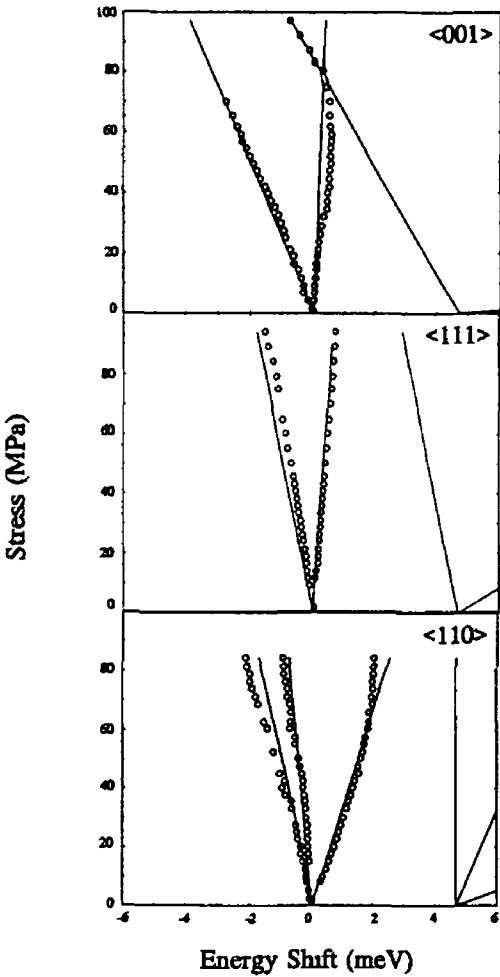


*Figure 6 13   Fan diagrams for Be$_A$ defect, solid lines represent fit to data using parameters of table 6 2*

## 6.4 Zeeman Measurements

Zeeman studies were carried out on the $Be_A$ line at the University of Aveiro, Portugal The experimental arrangements used are described in chapter 4 The Faraday configuration was used throughout the experiment which took place at 4 2 K

In the presence of a magnetic field up to 5 Tesla the zero phonon line did not split or show any appreciable broadening or shift with the field applied to either the <111> or <110> crystallographic directions; the $Be_A$ luminescence was not evident in the <001> sample For illustrative purposes only the 4 2 K spectrum for a magnetic field along the <110> axis of the sample is shown in figure 6 14 Similar spectra were obtained for the <111> sample

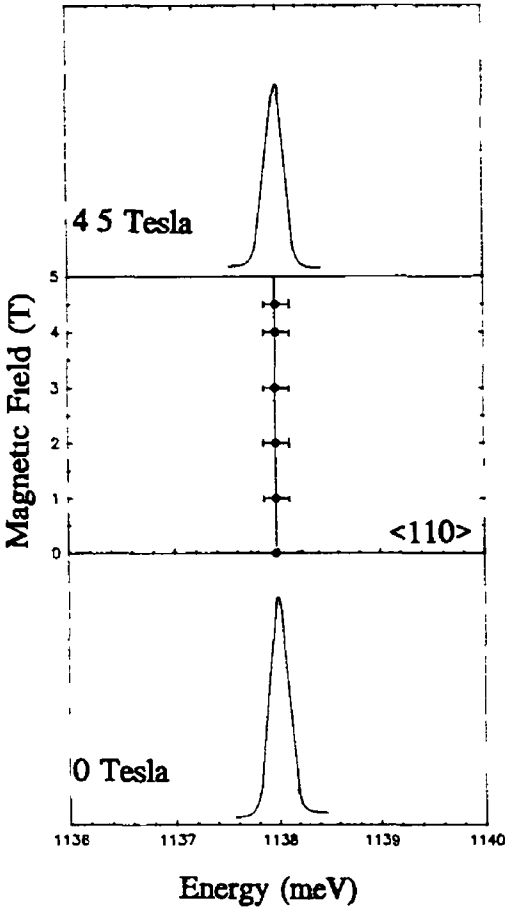In silicon, the valence band maximum is fourfold degenerate and holes are well



*Figure 6 14 Zeeman data obtained for <110> sample, both the <100> and <111> samples displayed the same behaviour, i e no splitting in a magnetic field up to 5 T*

described as $j = 3/2$ particles  When the hole becomes tightly bound at an axial defect the orbital angular momentum may become quenched and the hole then becomes a pure spin 1/2 particle, as described in section 2 6  In many cases, the spin 1/2 electron and hole couple to produce a singlet-triplet pair of levels with total spin $S = 0,1$ separated by the exchange energy, for example $S_A$ and $S_B$ defects in Si S [6]  This results in a very characteristic Zeeman splitting pattern  There are other cases, however, where no such coupling between the electron and hole is observed, the C centre, for example, behaves in this manner [7] as does the $Zn_A$ defect in silicon [8]  In the latter situation, negligible overlap of the electron and hole wavefunctions is believed to result in the absence of the exchange interaction  The Zeeman data must now be interpreted in a different fashion  A satisfactory model is that the observed optical transition (the $Be_A$ ZPL in this case) occurs between two spin 1/2 states, i e a spin 1/2 electron makes a transition into a spin 1/2 hole state  This is fully consistent with a pseudo-donor model for the $Be_A$ defect  As a final comment we note that a pseudo-acceptor model would involve a loosely bound $j = 3/2$ hole which would be expected to produce a readily observable line splitting in the experimental conditions used here  Accordingly, the Zeeman data very firmly favour a pseudo-donor model

This is not an unusual result when we consider the proposed isoelectronic nature of the defect  For isoelectronic defects the tightly bound particle is much more susceptible to the local crystal field around the defect  From the uniaxial stress data we concluded that the defect binds initially a hole which produces a Coulombic attraction for electrons

## 6.5 Discussion

The spectral position of $Be_A$, only ~ 31 meV below the silicon energy gap, is a clear indication that the states involved in this spectrum are most likely to be band-like or excitonic in nature  Zeeman data shows clearly that the origin of the $Be_A$ line can only be the recombination of a loosely bound electron with a tightly bound hole  We will assume that the tightly bound hole orbital is an $A_1$ state - a common assumption for highly localised states  We now consider how the $B_1$ and $B_2$ excited states which are indicated by the uniaxial stress data could arise  We begin by noting that the model of a tightly bound hole and loosely bound electron is that of a pseudo-donor

The 1s manifold of a pseudodonor will have, in Td symmetry, three states $A_1$, E and $T_1$   The ordering of these states is assumed to be inverted compared to substitutional donors, this assumption is based on the fact that the defect core is electron repulsive   For simplicity the E and $T_1$ states are assumed degenerate   In the axial $C_{2v}$ symmetry field of the defect these levels are further split as indicated in figure 6 15 Here, we have neglected any separation between states derived from the E and $T_1$ "parent" states   Clearly, this model can readily account for the occurrence of adjacent
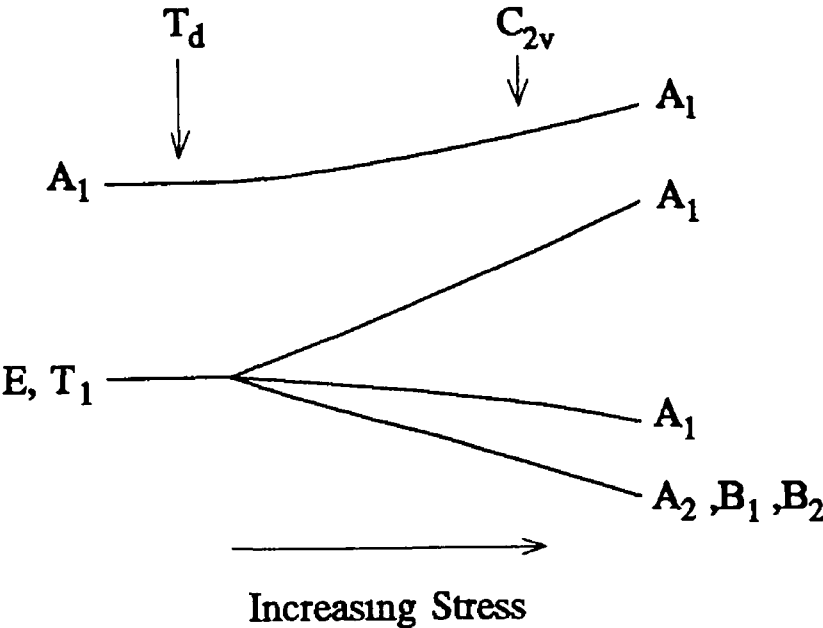


Increasing Stress

*Figure 6 15   Splitting of the 1s states of pseudodonor in $C_{2v}$ defect field*

$B_1$ and $B_2$ electron states   Until such time as stress data become available on the interacting excited state, a more precise identification cannot be made   Photoluminescence excitation measurements should prove to be particularly well suited to this task

The stress parameters $A_1$, $A_2$ and $A_3$ relate to the energy of the transitions i e , they give the changes in the perturbations of the final and initial states of the transition and are determined by the symmetry class of the defect   In silicon all defects are imbedded in a lattice of cubic symmetry $(T_d)$   In the case of isoelectronic defects, where

the loosely bound particle may orbit the defect with a radius equivalent to a number of lattice constants, the loosely bound particle may, not be subject to the local symmetry of the defect, and the wavefunctions are expected to be very similar to those of the appropriate band edge It is therefore of use to compare the values obtained for the stress parameters with those of the band states in order to determine the extent to which the lattice symmetry influences the transitions associated with the defect

The response of the silicon cubic crystal to uniaxial stress is described by Laude et al [9] If we compare the observed effects of stress on the $Be_A$ zero-phonon line with the perturbations experienced by the conduction band we find that the combination $A_1 + A_2$ is approximately 51 6 meV/GPa for the $Be_A$ defect, as compared to 92 5 meV/GPa for the conduction band splitting Therefore the response of the conduction band to stress accounts for approximately 52 % of the measured shift rates for this defect Under <001> stress the conduction band shift to lower energy is approximately twice that of the shift to higher energy which is similar to the result observed in this case The observed splitting of $Be_A$ under <001> stress resembles closely the behaviour of the conduction band, consistent with the conclusion that the electron is the loosely bound particle

The $A_3$ parameter is the only term in the Hamiltonian for defects with rhombic I symmetry that measures the response to shear stresses The conduction band is not affected by shear stresses, therefore we can conclude that the $A_3$ parameter derives from the hole state, which is the tightly bound particle, and which experiences the local strain field induced by the defect. If we compare the $A_3$ value with other isoelectronic defects exhibiting rhombic I symmetry, table 6 4, we find very similar values for the $A_3$ term in all cases All three defects included in this table behave in a similar fashion when subjected to a magnetic field, as will be discussed section 6 4 The response to stress of the $Be_A$ defect is remarkably similar to that of the $Zn_A$ defect, which incorporates the group II element Zn and O

| Defect | ZPL Energy (meV) | $A_1$ | $A_2$ | $A_3$ |
|---|---|---|---|---|
| $Be_A$ | 1137 98 | -40 1 | 11 0 | -19 5 |
| $Zn_A$ [10] | 1129 5 | -52 0 | 15 0 | -17 2 |
| In"PQR" [11] | 1129 4 | 7 0 | -11 3 | -17 8 |

*Table 6 4  Comparison of stress parameters for defects of $C_{2v}$ symmetry*

In conclusion, by comparing the stress parameters with those obtained for the band edges in silicon, we find that the observed behaviour of the stress data partly derives from the conduction band states  This is typical of an isoelectronic defect, as the loosely bound particle may orbit the defect with a radius of a few atomic spacings and so is likely to experience the symmetry of the lattice as well as the defect with which it is associated  It was concluded that the hole is the tightly bound particle and the electron the loosely bound particle

## 6.6 Tentative Model for the Defect

A model for the defect that satisfies all of the observed behaviour remains to be confirmed  However, on the basis of the data presented above and that of the previous chapter, the following model is proposed

The symmetry operations associated with a defect displaying rhombic I ($C_{2v}$) symmetry are a 2 fold rotation axis about a <001> type axis and two mutually perpendicular reflection planes parallel to <110> type axes, as illustrated in figure 3 7  The axial defect must conform to these symmetry operations

It was proposed in the previous chapter that the defect consists of a Be-O complex  Oxygen is known to favour the bond centered interstitial site  In this defect the Be atom is believed to occupy a substitutional site since the slow cooling necessary for its production results in a high substitutional fraction of Be [12]  Therefore if we assume that the defect consist of one Be substitutional atom and one O interstitial
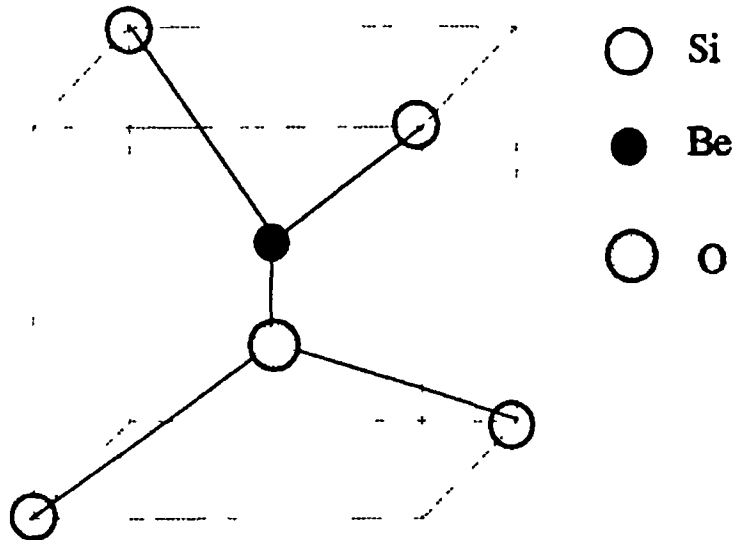
*Figure 6 16   Model of Be_A defect incorporating a one Be and one O atom.*

atom a possible model could be that of the Be and O atom forming an axial defect parallel to a <100> type axis, with the Be atom displaced off the substitutional site   The bonding between the Be, O and neighbouring Si atoms must be such as to produce an electrically neutral ground state   Bonding of a Be atom to two of the Si atoms is possible since each Be atom has two outer electrons in the 2s shell   This would result in a $Be^{2+}$ core   Similarly, if an O atom bonds with the remaining two Si atoms at the defect an $O^{2}$ configuration will result   The net effect is to create a neutral defect with a strong ionic bond between the $Be^{2+}$ and the $O^{2-}$ constituents   A schematic representation of the model proposed here is illustrated in figure 6 16   A strong ionic may also account for the presence of the strong local mode phonons observed in the PL spectrum   A theoretical investigation of the vibrational properties of such a Be-O complex would be informative

## 6.7 Conclusions

In the previous chapter it was proposed that the $Be_A$ defect was isoelectronic in nature  In this chapter it was concluded that the observed luminescence band was caused by the recombination of electron-hole pairs bound to a neutral core  The energy of dissociation of the bound complex was found to be 27 2(3) meV with respect to the conduction band

The splitting patterns of the zero phonon line were found to be consistent with an axial defect in a low symmetry field  The symmetry was found to be that of a rhombic I ($C_{2v}$) centre  Companson of the splitting pattern with that of the conduction band edge suggested that the loosely bound particle was an electron,  leading to the conclusion that the electrically neutral defect introduces a short range potential that is hole attractive  This was confirmed using Zeeman spectroscopy, from which it was concluded that the spin state of the defect was isotropic in a magnetic field  This is consistent with the quenching of the orbital angular momentum, i e  the lifting of the degeneracy associated with the valence band in the vicinity of the defect  The hole therefore displays only spin angular momentum with s = 1/2, exactly as for the loosely bound electron

**References:**

[1]     G  Davies  Private Communication

*[2]     A A  Kaplyanskii,  Opt  Spectrosc  16  (1964) 329*

*[3]     A A.  Kaplyanskii  Opt  Spectrosc  16  (1964) 557*

[4]     K  Mohammed, G  Davies and A T  Collins  J  Phys  C 15 (1982) 2779

[5]     G  Davies, M H  Nazare and M F  Hamer  Proc  R  Soc  Lond  A 351  (1976) 245

[6]     M  Singh, E C  Lightowlers, G  Davies, C  Jeynes and K.J  Reeson  Mat  Sci  and Engineer  B4  (1989) 303

[7]     K  Thonke, A  Hangleiter, J  Wagner and R  Sauer, J  Phys  C  18  (1985) L795

[8]     J  Campion, Private Communication

[9]     L D  Laude, F  H  Pollak and M  Cardona, Phys  Rev  B 3  (1971) 2623

[10]     M O  Henry, J D  Campion, K G  McGuigan, E C  Lightowlers, M C  do Carmo and M H  Nazare Semicond  Sci  Technol  9  (1994) 1375

[11]     S P  Watkins and M L W  Thewalt, Phys  Rev  B 34  (1986) 2598

[12]     R K  Crouch and J B  Robertson, Phys  Rev  B 5  (1972) 3111

# Chapter 7

# Radioactive Isotope Effects on Photoluminescence Spectra

## 7.1 Introduction

In chapter two we saw that optically active defects within a semiconductor have electronic states which are influenced by both the constituents of the defect and the surrounding lattice. By altering the isotopic mass of the impurity the frequency and amplitude of vibration of the defect may be altered resulting in a shift in energy of the zero phonon line and the associated local modes of the defect.

This method of substitution of isotopes of suspected defect constituents is a well established technique used to unambiguously identify a particular atom as a defect constituent. Isotopes of the same element have the same number and arrangement of extra-nuclear electrons and so have the same structure for their spectra. They are distinguished from each other by their nuclear mass. Isotope effects on spectral lines are therefore a manifestation of the influence of the mass of the nucleus. With increasing atomic number the fractional change in mass of the nucleus is smaller, and so one would expect the isotope effect to become smaller. However, even for elements with a high atomic number a noticeable isotope effect may be present.

A good example of the effect of isotope substitution detected with PL spectroscopy is illustrated in figure 7.1 for the so called $Zn_A$ and $Zn_B$ defects for samples containing selected zinc isotopes [1]. An unambiguous lineshift is observed between samples containing $^{64}Zn$ and $^{68}Zn$, with shifts of 0.10 meV and 0.09 meV respectively for the $Zn_A$ and $Zn_B$ zero phonon lines. It was therefore concluded that zinc was a constituent of the defects.

Many defects exhibit local vibrational modes within their PL sideband structure. With the introduction of isotopes of the chemical constituent of the defect, the principal atom(s) contributing to each local mode can be determined. Again referring to the zinc related defects mentioned above, shifts in a local mode at approximately 12 meV led to the conclusion that the vibrational motion is predominantly that of a zinc atom oscillating with respect to a static lattice.
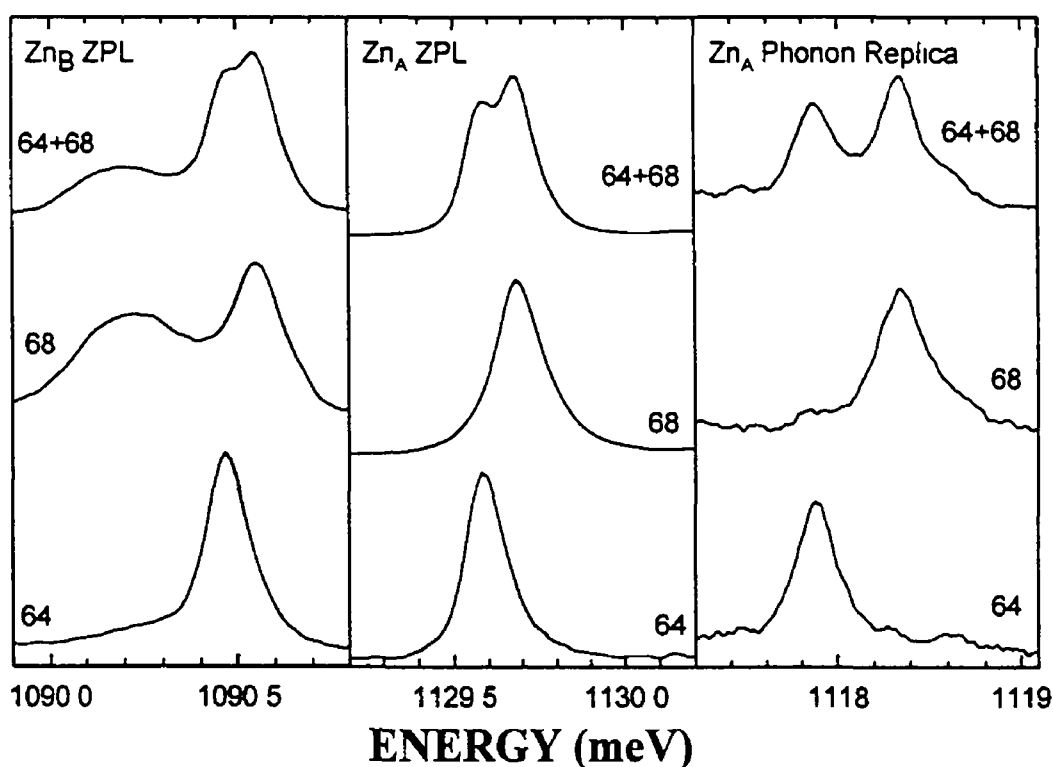
*Figure 7 1  High-resolution PL spectra of the $Zn_A$ and $Zn_B$ defects, showing the effect of isotope substitution on both the ZPL lines and on a phonon replica of the $Zn_A$ line, from [1]*

## 7.2 Radioactive Isotopes

Table 7 1 includes all available isotopes of Be   As is clear from this, the existence of only one stable Be isotope precludes the use of isotope substitution experiments, therefore making constituent identification difficult

In the following, we consider the feasibility of using radioactive isotopes as a means of identifying the chemical constituents of a defect   Data was obtained for the well known In related "PQR" centre in silicon [7] and demonstrates the scope of this technique   Firstly, some areas of semiconductor research in which radioactive isotopes have been employed will be considered followed by an evaluation of the use of radioactive isotopes as a means of identifying defect constituents

| Isotope | Abundance or Radioactive Half-life |
|---|---|
| 7 | 53 3 days |
| 9 | 100% |
| 10 | 1 6 x $10^6$ years |
| 11 | 13 8 seconds |
| 12 | 11 4 mseconds |

*Table 7 1    Isotopes of Beryllium   $^9Be$ with 100% abundance is the only available stable isotope*

Radioactive isotopes have had a relatively narrow range of applications in semiconductor research to date  The principal application has been in diffusion studies where the penetration of the atoms into a solid can be accurately measured [2] Mossbauer spectroscopy has been a consistent feature of semiconductor research also, albeit with a limited number of suitable isotopes [3]   Perturbed angular correlation [PAC] is a relative newcomer to semiconductor spectroscopy and involves the detection of γ-ray emission to provide information on defect characteristics [4]   This, too, suffers from the limited availability of suitable γ emitters  Lastly, the channelling and blocking of radioactive decay products can be used to reveal information regarding the location of impurities in crystals [5]

A unifying feature of all of the techniques mentioned so far is that the decay products (radiation or particles) are monitored directly  The effect of a radioactive decay process on other signatures of the isotope or its daughter products can also be exploited  In the case of semiconductors this was first demonstrated by Peterson and Nielson [6] in a DLTS study of gold and platinum related defects in Si  The appearance or disappearance of a spectrum at a rate consistent with a specific radioactive half-life can thus provide excellent information on the chemical identity of defect impurities  It will be shown here that PL spectroscopy can be used to monitor the appearance and/or disappearance of a PL signal associated with a defect centre involving the implanted ion

Photoluminescence is particularly well suited, due to its high sensitivity, to situations involving low concentrations or small volumes  However, a disadvantage is

the difficulty of producing quantitative intensity data, an important consideration for the experiment described here This is particularly true when excitation is achieved by using radiation with energy greater than the band gap energy The intensity of a defect PL spectrum then depends critically on the capture cross section of the defect for excitons or free electrons and holes and on the radiative efficiency of the defect following the capture process Competition between centres for the free carriers and/or excitons may result in one defect only dominating the spectrum, the appearance of a new spectrum for different conditions may result simply from the elimination of totally unrelated but much more effective carrier traps The concentration of a defect is also a key factor For low concentrations, it is possible to saturate a PL line intensity, i e increasing the excitation density cannot produce greater PL intensity since all available defects are excited However, if the defect concentration is high, it may not be possible to achieve saturation Aside from all of these fundamental considerations, the requirement of reproducible optical and temperature conditions must be met for quantitative measurements

## 7.3 Radioactive Indium in Silicon

To evaluate the use of radioactive isotopes in photoluminescence spectroscopy $^{111}$In was employed There are several reasons for choosing this isotope Firstly, the half-life of 2 8 days is suitable for the practicalities of PL spectroscopy Secondly, In in silicon is known to produce one of the most intense PL emissions recorded in silicon (when suitably treated [7]) so that a low dose implantation, and hence low activity, is sufficient

The starting material used was high purity FZ silicon with resistivity of approximately 20,000 Ωcm Radioactive $^{111}$In ions were implanted at an energy of 80 keV to a total dose of $10^{11}$ atoms into an area of 2 x 2 mm$^2$ The measured activity of the sample following implantation was 10 μCi The sample was RCA cleaned and a rapid thermal annealing was performed in air in the manner described by Thewalt et al [6] to enhance the Si In PL An air cooled argon ion laser operating at 100 mW was used to excite the luminescence

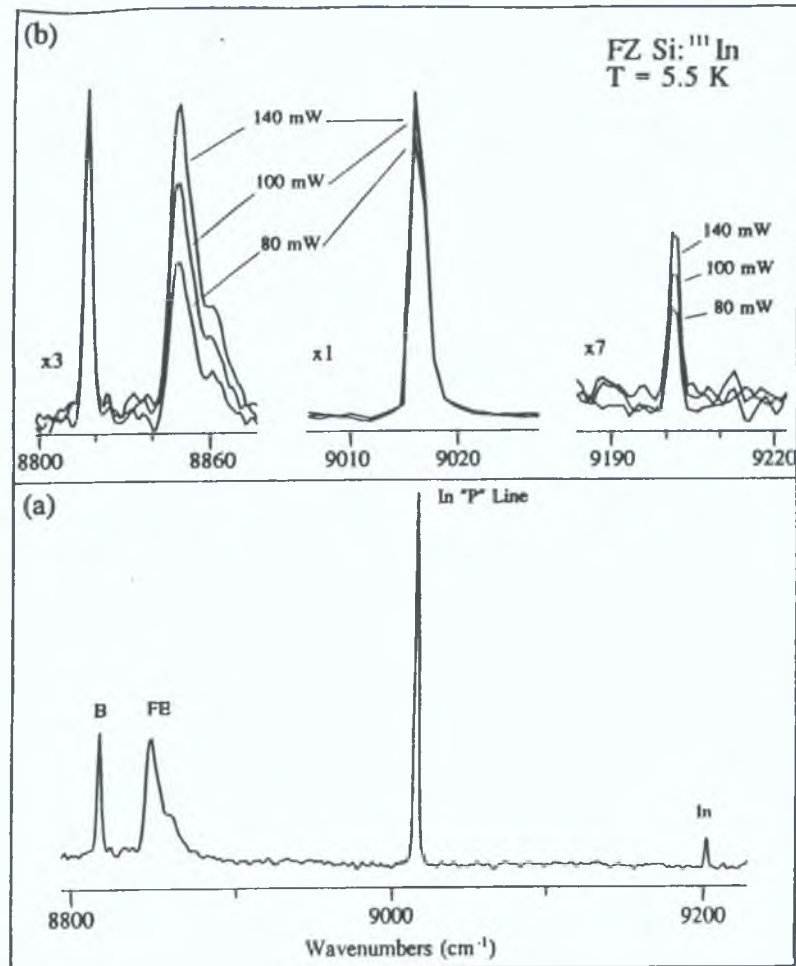Figure 7 2 illustrates some of the difficulties regarding saturation of the defects

*Figure 7.2  (a) The PL spectrum of Si:In at 5.5 K for a laser power of 140 mW, and (b) spectra recorded at 5.5 K for laser powers of 80, 100 and 140 mW.*

upon illumination.  A PL spectrum of Si:In recorded at 5.5 K is shown in figure 7.2(a). The line at ~ 9200 $cm^{-1}$ is due to neutral In acceptor bound exciton (BE) recombination. The line at 9013 $cm^{-1}$ is the P line of the In related "PQR" spectrum [8].  Features due to free exciton recombination with the emission of LO or TO phonons and BE recombination at neutral boron acceptors, again with the emission of TO phonons are also evident.  The effects of different excitation conditions are shown in figure 7.2(b). When the laser power is increased from 80 mW neither the boron related line nor the P line changes appreciably in intensity.  However, the intensities of both the In acceptor BE line and the FE line increase with laser power.  Hence, the PQR and boron PL intensities are saturated, whereas the neutral In acceptor PL is not.  The boron concentration is known to be low, < $10^{13}$ $cm^{-3}$.  The total In concentration following

implantation is estimated to be ~ $6 \times 10^{17}$ cm$^{-3}$. We can conclude that only a small fraction of the implanted In is involved in the PQR centres in agreement with Thewalt et al [6]. The choice of laser power is clearly very important for comparing PL intensities. In the data that follows, the intensity of the P line and the indium acceptor BE line as a function of time will be examined. A laser power of 100 mW was chosen as standard for the experiment since this was sufficient to achieve saturation of the P line when the PQR centre concentration was at its greatest value; with the concentration expected to decrease with time this condition could be maintained. For the indium acceptor BE this saturation condition could not be achieved. In this case there was a danger that the PL might become saturated as the indium concentration decreased with time. However, care was taken to ensure that this possibility was not overlooked in the experiment by recording spectra over a range of laser powers.

The Si:$^{111}$In sample was first annealed three days after implantation. Intense PQR luminescence was observed with a P line signal to noise ratio of ~ 800. Within one day the signal was no longer detectable, an extraordinary result when a 2.8 day half-life was expected. The sample was re-annealed, on this occasion six days after implantation. The PQR luminescence signal was recovered to approximately the same signal level. The rapid loss of intensity was confirmed and the data which reveal this are shown in figure 7.3. The full spectrum in figure 7.3(a) was recorded approximately two hours after quenching. The main line P and its associated sidebands dominate the spectrum, extending to the O$^{\Gamma}$ cut-off at ~ 8940 cm$^{-1}$. Both the free exciton (FE) and the boron bound exciton (B) lines can also be observed. The neutral indium acceptor BE line, however, is barely detectable. Increasing the laser power from 100 mW to 140 mW caused an increase of only 4% in the P line intensity but without producing any In acceptor BE PL.

The lowest spectrum in figure 7.3(b) is for eight hours after quenching. Here the P line intensity is lower by a factor of ~ 2 and the In acceptor BE line is now evident. The evolution of the spectrum is shown in the remaining spectra of figure 7.3(b). Both the PQR spectrum and the neutral In acceptor BE line decreases in intensity, the former very rapidly, while the FE and B lines maintain their intensities very well.

These results are summarised in figure 7.4 which shows the intensity decrease of both the P line and the In acceptor BE line with time. The squares and circles are data points for the neutral In acceptor bound exciton and the PQR centre respectively.
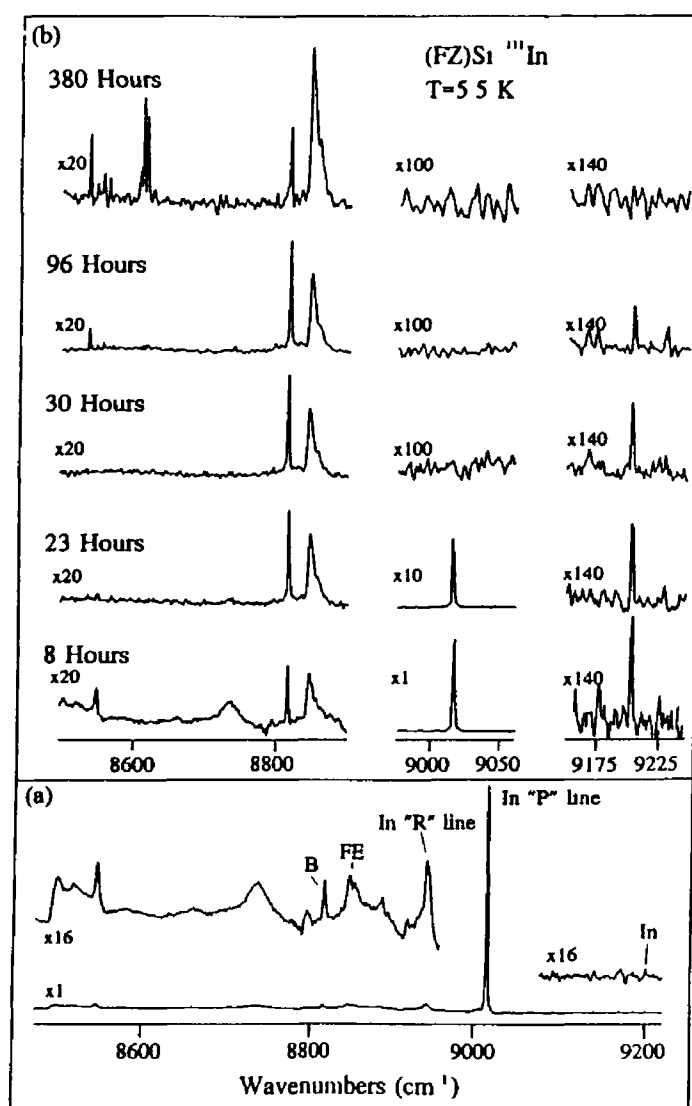
*Figure 7 3 (a) "PQR" In related spectrum, and (b) the "PQR" spectrum as it evolved over 16 day period*

The final data point for the PQR centre, depicted by an open circle, corresponds to the noise floor, the line was not detected at this time   For the neutral In BE line the spectrum taken after eight hours was used as the origin   The solid line shows the change expected for a 2 8 day half-life   The acceptor bound exciton intensity is seen to follow this closely, whereas the PQR intensity departs markedly   The most likely explanation for the latter is the passivation of the PQR centres   It is known that the PQR PL intensity slowly degrades with time following a quench for bulk In doped
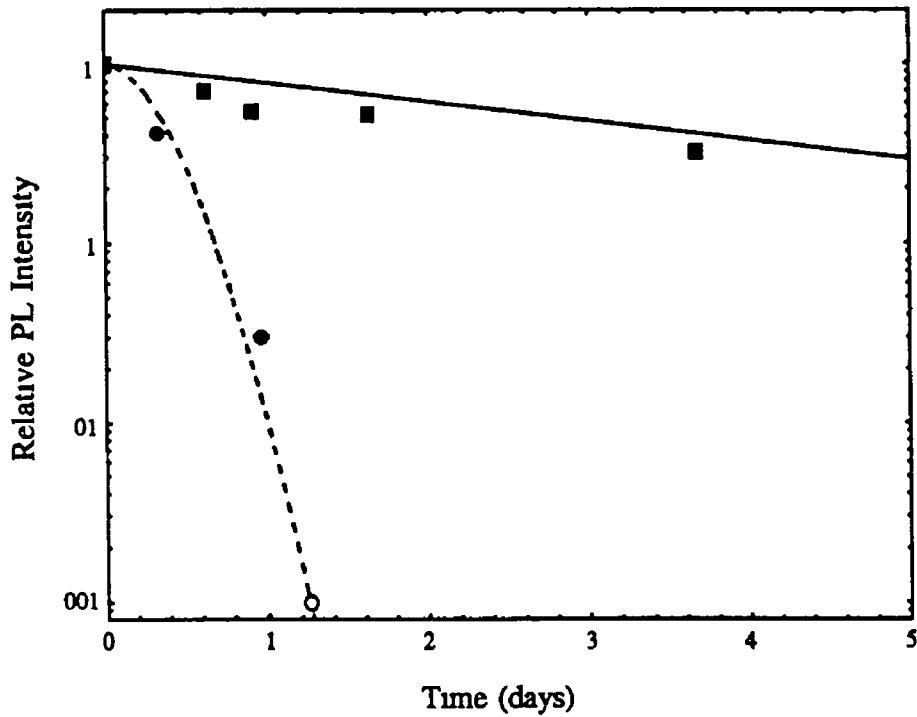
*Figure 7 4   PL Intensity changes for In related PL spectra as a function of time   Solid line indicates a half-life of 2 8 days   The broken curve is as described by equation 7 1*

samples [9]   However, an investigation of samples implanted with stable $^{115}$In and similarly annealed do not display the marked behaviour of $^{111}$In   Several possibilities should be considered as the passivating species   Since the concentration and total population of PQR centres are both very low, trace amounts of impurities which are mobile at room temperature could readily lead to total passivation   Transition metal contamination is one likely source of passivation   The presence of $^{111}$Cd daughter atoms in the implanted layer produced in the decay of $^{111}$In must also be considered   The diffusivity of Cd in Si at room temperature is not known   However, given the proximity of the implanted ions - the straggle is only 13 nm - even a small value could be sufficient to cause daughter $^{111}$Cd atoms to migrate to surviving In PQR centres   In this scenario, the decrease in the P line intensity can be modelled by the following expression,

where $\alpha = 0\ 247$ day$^{-1}$ is the radioactive decay probability, $\beta$ (an adjustable parameter) is a measure of the probability of capture by surviving $^{111}$In PQR centres of daughter $^{111}$Cd atoms for which the concentration as a function of time is proportional to the factor $\{1-\exp(-\alpha t)\}$ This simple formula neglects any source of passivation other than the decay of $^{111}$In atoms, but it does produce qualitatively the observed time dependence of the PQR intensity The broken line in figure 7 4 is obtained for $\beta = 20$ m$^3$day$^{-1}$

It is evident from figure 7 3(b) that a series of new lines appear after long delays - these will now be discussed It is noteworthy that the intensity of the luminescence for all new spectra is of the same order of magnitude as the boron acceptor bound exciton emission, and certainly much less than that observed for the PQR isoelectronic centre It is likely, therefore, that the centres producing the new spectra are donor or acceptor in nature rather than isoelectronic Substitutional Cd would be expected to produce double acceptor bound exciton recombination which has never been seen in silicon although examples exist for Ge [10,11] The complexity of the line structures observed may well be consistent with such recombination, but such a conclusion is tentative The PL intensities are too weak to reveal either two-hole or two-electron satellites which would confirm the nature of the recombination centres A variety of samples with greater initial doses of $^{111}$In would reveal such detail

The influence of the radioactive decay process must also be considered The capture of an inner shell electron by the parent $^{111}$In nucleus leads to a substantial energy release by the $^{111}$Cd daughter, culminating in the production of two $\gamma$-rays per disintegration Although much of this energy is deposited in the crystal there is no evidence from many experiments using $^{111}$In in PAC [12] that defect production adjacent to the In/Cd atoms is significant Furthermore, the total radiation dose received by the crystal from a typical implant dose of $10^{11}$ atoms is orders of magnitude less than the norm for PL defect production [13] Accordingly the effects of the decay process itself can be neglected

It is clear that the dramatic changes observed in the intensity of isoelectronic bound exciton recombination spectrum "PQR" are too fast to be attributed to radioactive decay alone However, the substitutional In acceptor bound exciton is found to decay at a rate appropriate for the $^{111}$In half-life These results establish the feasibility of using

radioactive isotopes in PL spectroscopy and they also provide a striking illustration of how such experiments may be exploited in the study of a wide range of defects in all classes of semiconductor

## 7.4 Radioactive Beryllium

The exploitation of radioactive isotopes in the area of defect constituent identification is obvious, with particular application to atoms whose range of available isotopes is restricted as in the case of beryllium. It is proposed to perform an experiment such as this using $^7$Be, which with a half-life of 53 3 days is suitable to the technique described here. Therefore, in the absence of suitable stable Be isotopes it will be possible to confirm the involvement of Be in the defect analysed in chapters five and six

## 7.5 Conclusions

A range of factors need to be considered before undertaking experiments such as these. Firstly, the production of suitable isotopes in sufficient quantities and with adequate mass separation must be achieved. Yields must be high in order to implant the necessary dose in a reasonable time. Half-life values also impose severe constraints, values of the order of hours require both high yields and on line PL facilities, while values of the order of several weeks or longer are not well suited to PL spectroscopy because of the difficulties associated with quantitative PL measurements. Nevertheless, there are many problems in the characterisation of semiconductors, particularly regarding the chemical identification of impurity centres, which would be amenable to PL analysis using this approach. Other high sensitivity techniques such as EPR and PTIS should also prove to be particularly suitable for use in conjunction with radioactive isotopes

# References

[1]     M O  Henry, J D  Campion, K G  McGuigan, E C  Lightowlers, M C  do Carmo and M H  Nazare  Semicond  Sci  Technol  9 (1994) 1375

[2]     G E  Murch and A S  Nowick, "Diffusion in Crystalline Solids", Academic Press, 1994

[3]     L  Nieson, "Mossbauer Spectroscopy Applied to Inorganic Chemistry", ed  G J  Long,  Plenum 1987

[4]     H E  Mahnke, Huperfine Interactions 49, (1989) 77

[5]     H  Hofsass and G  Linder, Physics Reports 201 (1991) 121

[6]     J W  Peterson and J  Nielson, Appl  Phys  Lett  56, (1990) 1122

[7]     M L W  Thewalt, U O  Ziemelis and R R  Parsons, Solid State Commun  39 (1981) 27

[8]     G S  Mitchard, S A  Lyon, K R  Elliott and T C  McGill, Solid State Commun  29 (1979) 425

[9]     J  Weber, R  Sauer and P  Wagner, J  Lumin  24/25 (1981) 155

[10]    H  Nakata, T  Yodo and E  Otsuka, Solid State Commun  45 (1983) 55

[11]    R  Sauer and J  Weber, J  Phys  C  Solid State Phys , 17 (1984) 1421

[12]    H  Skudlik, M  Deicher, R  Keller, R  Magerle, W  Pfeiffer, D  Steiner and E  Recknagel  Phys  Rev  B 46 (1992) 2159

[13]    G Davies Phys  Rep  176 (1989) 83

# Chapter 8

# Conclusions and Suggestions for Further Work

## 8.1 Conclusions

The focus of this thesis has been on the characterisation of a defect in Be implanted silicon. The defect was first identified by Gerasimenko et al as one of a number of defects produced in Be implanted silicon annealed at temperatures in the range 550 - 800° C. Little was known of this defect other than the position of the zero phonon line and that it was preferentially produced in oxygen rich silicon. In this study the involvement of oxygen was largely confirmed from a comparison of oxygen rich and oxygen lean material. It has not been possible to confirm or refute the involvement of C in the defect. It was concluded that the most likely defect constituents were Be and O.

High radiative efficiency and the sideband structure suggested the defect to be isoelectronic in nature. The response to temperature revealed a dissociation energy for an electron-hole pair bound to the defect of ~ 27 3 meV compared to a spectroscopic binding energy of ~ 31 meV. The binding mechanism is complex as there is a large relaxation energy associated with the luminescence process. Perturbation techniques were successfully employed to probe the microscopic structure and symmetry of the defect. Uniaxial stress spectroscopy revealed a rhombic I ($C_{2v}$) symmetry and a non linear response to stress suggested the existence of a nearby excited state. Using Zeeman spectroscopy the isoelectronic nature of the defect was confirmed and it was concluded that the defect consists of hole attractive core. The defect is consistent with a pseudo-donor model.

The difficulties associated with the application of isotope studies to this defect were considered and a new technique involving radioactive isotopes was presented which should overcome these difficulties. This is the first time that radioactive isotopes have been employed for the identification of defect constituents.

## 8.2 Suggestions for Further Work

The most immediate investigation that is required concerning this defect is the application of photoluminescence excitation in order to characterise the excited state structure. The position of the excited state spectrum lends itself to the use of a Ti-sapphire laser to facilitate this measurement. Uniaxial stress and Zeeman measurements on the excited states of the defect could be carried out with this system, thus establishing the symmetry of the excited states.

The characteristic local mode structure associated with this defect shows some anomalies in the multiphonon sideband. A theoretical investigation of the vibrational properties of a Be-O axial defect would be very interesting in this respect. Using isotope substitution experiments the origin of the local modes may be determined. The binding mechanisms associated with this defect are complex, particularly with regard to the relaxation energy observed in the luminescence process.

Radioactive isotope experiments using $^7$Be should confirm the involvement of Be in the defect. Material diffused with isotopes of oxygen would further confirm the involvement of O in the defect. As this defect was observed in ion implanted material which has an abundance of carbon interstitial atoms that are highly reactive, the study of samples with selected isotopes of carbon would determine whether C is also a constituent of the defect.

# Acknowledgements

# Appendix A

## RCA Cleaning Procedure for Silicon

1 Boil in methanol

2 Rinse in cold methanol

3 Boil in trichloroethylene

4 Rinse in cold methanol

5 Rinse in de-ionised water

6 Boil in $NH_4OH$   $H_2O_2$   $H_2O$, 5 1 1

7 Rinse in de-ionised water

8 Boil in HCl   $H_2O_2$   $H_2O$, 5 1 1

9 Rinse in de-ionised water

10 Blow dry